Optimisation of a latent heat storage system containing a salt hydrate

Master of Science Thesis

Wessel Sanderse

Delft University of Technology

TU Delft

Optimisation of a latent heat storage system containing a salt hydrate

by

W. G. (Wessel) Sanderse

to obtain the degree of Master of Science in Mechanical Engineering.
at Delft University of Technology,
to be defended publicly on Monday October 16, 2023 at 9:30 AM.

Student number:	4466438
Project duration:	September, 2022 - October, 2023
Specialisation:	Energy, flow and process technology

Thesis committee:	Prof. Dr. K. Hooman	TU Delft, Supervisor, Chair
	Dr. R. Delfos	TU Delft
	Dr. Ir. W.P. Breugem	TU Delft

TU Delft

Abstract

The purpose of this study is to develop a methodology that is capable of scaling the commercially available latent thermal energy storage system with salt-hydrate HS48 as phase change material. The scaling model should provide information on the optimal design parameters of the heat battery for different sizes and energy demands. Phase-change materials are widely used for thermal storage applications, such as water, salt hydrates, paraffin, selected hydrocarbons, polymers, and metal alloys. In this paper, the literature related to PCM properties, theory, and practical applications in various energy storage systems is reviewed, providing a solid foundation for the research and analysis. The literature includes configurations in which PCM is integrated into hot water storage tanks, including designs with copper pipes, cylindrical modules, and spherical capsules. Finally, we discuss how these systems can use PCM to effectively store and release thermal energy.

A research method is developed providing the specifications that are needed to scale a thermal energy storing system. The methodology is based on the heat transfer principles of the phase-change storage unit and the specifications of the commercially available heat battery. The methodology provides a scaleable model capable of simulating the outputs of the commercial heat battery. The model is validated by the designed experimental set-up, and thus able to provide a simulation of the system for different sizes.The methodology proposes the assumptions, which enables us to use the model for the commercially available heat battery. The model simulates a hot and a cold circuit running through a PCM with one-dimensional heat transfer. The emphasis of the model is to design a model for two different scales and to produce realistic outputs. The results of the temperature distribution show that the charging time is increasing nonlinearly with an increase in the mass of the PCM. The smaller laboratory-scale version is used as the basis for the design of the experimental setup. The validated model is compared with the measured data from the experimental setup. The results of the model and the real-life data are analysed to provide the basis for the experimental validation. The performance of the model is closely aligned with the experimental data, revealing results that resemble the experimental data with minor differences in temperature values. However, the average effectiveness of charging and discharging shows significantly improved results compared to the test sequence.

To provide favourable outcomes, the validated system is optimised by enhancing the thermal conductivity of the phase change material and creating a more compact design. The model is then scaled to the power output delivered by the commercially available heat battery. The model is expressed in three variations of the scaled model. The configurations are based on highlighting each of the three independent variables that describe the system : (1) the number of parallel tubes, (2) the number of passes per tube, and (3) the length of a single pass. The configurations are evaluated on the five main outputs; From the results of these outputs, the optimal design is determined.

The results indicate that the applied optimisation has significant positive effects on the output of the system. With all the configurations discussed, the optimal design is chosen to be configuration 3, where the highlighted variable is the number of parallel tubes (1). Implementing this design in a commercially available heat battery will reduce the mass of the PCM, the size of the system, and the charging time. This study demonstrates promising results and identifies areas for improvement, particularly related to the idealised assumption of phase-changing behaviour and specific application requirements, such as domestic hot water supply.

Preface

This thesis, "Optimisation of a latent heat storage system containing a salt hydrate", is the result of my graduation project to obtain a Master's degree in Mechanical Engineering with the specialisation of Energy, flow and process technology at the University of Technology Delft.

First of all, I would like to thank Kamel Hooman for the pleasant guidance throughout the project. I enjoyed our discussions and have been motivated throughout the project by your positive and supportive mindset.

Another word of gratitude must be given to Bart Hoek for his supervision during my experiments.

Furthermore, I would like to thank Rene Delfos and Wim-Paul Breugem for being part of my graduation committee.

Lastly, I would like to thank my family, friends, and roommates for their support, listening ears, and all non-academic distractions.

Wessel Sanderse
Delft, October 2023

Contents

1 Introduction

1.1. Background and motivation

Since the world's current energy demand is currently increasing, there is a constant search looking for new energy supply alternatives. The use of renewable energy sources is an environmentally friendly approach to a sustainable future. [1]. While renewable energy offers a great solution to reducing greenhouse gas emissions, it also poses challenges in terms of storage.

By capturing surplus energy during off-peak demand hours and delivering it during peak demand, energy storage systems enhance the efficiency of energy systems and reduce overall energy wastage. This leads to more efficient utilisation of renewable resources and a decrease in energy costs.[2] Energy storage systems can also ensure grid stability and reliable energy supply by storing excess energy during periods of high production and releasing it when needed. This helps balance supply and demand, while also reducing the dependence on fossil fuels for backup power generation [3].

Energy storage can be classified into three main types, namely mechanical storage. batteries and thermal energy storage. Thermal energy storage (TES) focusses on capturing and storing heat through a specific medium. TES systems operate on the following fundamental principles : heat is delivered to the TES (by charging), stored there (by storing), and then taken from the TES for usage (discharging) [4].

TES is particularly significant when used for domestic applications, such as heating and providing hot water. A TES system must have the capacity to store absorbed energy for at least a few days to deliver hot water when needed. By storing renewable energy with thermal energy storage, we could remove residences from conventional gas-powered boilers, which would be a huge leap into a sustainable future. The challenge lies in storing the collected heat in the most efficient way and being able to extract this stored heat when it is most necessary[2].

Latent heat storage

Thermal energy storage can be divided into two categories: active and passive storage concepts. In active thermal storage systems, the storage medium itself circulates. These active systems are characterised by forced convection in the material. For passive systems, a heat transport medium passes through the store to carry energy to and from a storage medium [5]. A phase change material (PCM), a solid, a liquid, or chemical reactants can be used as storage media, according to Pinel [6]. Thermal energy can be stored using any of the following storage mechanisms: sensible heat, latent heat, or a mixture of the two [7].

In contrast to sensible heat storage, latent heat storage using PCM can offer a much greater storage capacity at the same temperature range. An essential quality is isothermal storage [8]. It is possible to have a smaller and less expensive thermal storage system since the storage capacity of such a system is mostly determined by the latent phase change heat, which is often many ten times larger than the sensible heat [7]. When their phase structures are reformulated during the melting/solidification process, PCM's have the capacity to store/release a significant amount of heat [9].

The evolution of enthalpy of a PCM as a function of temperature is shown in Fig. 1.1. Heat is stored in sensible form in the regions of the curve where the temperature is lower than or higher than the fusion

temperature. The amount of heat stored is the product of specific heat and increased temperature. The compound goes through a phase change at the fusion temperature and can absorb or release energy at a temperature that is nearly constant as long as the phase change is incomplete. That is, as long as the energy injected into or extracted from the PCM is not equal to its enthalpy of fusion. Therefore, the latent heat storage potential of a PCM is equal to its fusion enthalpy [6]. A thermal storage system has the best energy storage efficiency if the medium can be removed from it at the same temperature at which it was initially stored [7].

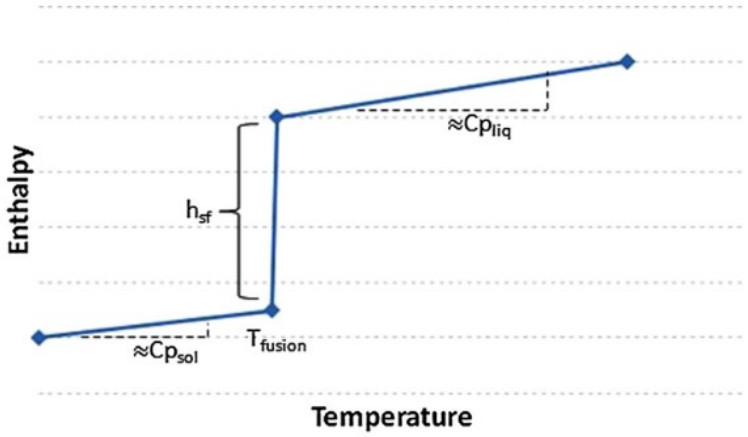

Figure 1.1: Enthalpy evolution of a compound under going a change of phase [6].

The main advantage of latent heat storage over sensible heat storage is that latent heat systems accumulate more energy per unit mass and can store or transfer heat with small changes in temperature [8]. Unlike sensible heat storage in which materials have a large temperature difference when storing thermal energy, latent heat storage can work in a nearly isothermal way. This makes latent heat storage favourable for applications that require strict working temperatures [9]. Latent heat storage systems typically possess relatively compact dimensions and lower masses in comparison to other energy storage systems. Furthermore, they offer the distinct advantage of high storage capacities, making them attractive choices for a variety of energy storage applications [4].

The biggest drawback of latent heat storage is its poor thermal conductivity [9]. Encasing PCM to increase the heat exchange area and running the heat transfer fluid over a bed of these capsules is a typical solution to the thermal conductivity issue. Compared to a tank filled with only the heat transfer fluid, this yields a higher storage density and a more consistent storage temperature. Encapsulation also has the benefit of making volume adjustments easier to handle. PCM particles can also be included in the structure of other substances to achieve better heat transfer characteristics [6].

PCM can be categorised into organic and inorganic PCM [10]. Paraffin wax is one of the most significant classes of organic PCMs. It is regarded as chemically inert, stable, less expensive, and suffers minimal volume fluctuations during the melting process, and has a low vapour pressure in the melt state. As a result of these factors, paraffin systems typically have very long freeze-melt cycles. Some undesirable characteristics of paraffin wax include its low thermal conductivity, incompatibility with plastic containers, and flammability. Inorganic PCMs include salt hydrates, salts, metals, and alloys. The main advantages of inorganic PCMs are their high thermal conductivity and large volumetric latent heat storage capacity, which is frequently twice that of organic compounds. Supercooling, phase separation, and lack of thermal stability are the main problems with salt hydrates [4].

Latent thermal energy storage systems are suitable for use in certain sectors and applications. For example, the usability of PCM materials is an ideal thermal storage solution in buildings, power generation, the food industry, and automotive applications and it was concluded that significant improvements can be obtained in overall energy performance for the system in these sectors [11]. For this research, the storage system will be applied to power generation for residential homes. In this case, the system is described as a heat battery [12].

1.2. Research goal

For the full utilisation of a latent heat storage system in the form of a heat battery, the optimal design parameters should be quantified through a numerical model. The design of the heat battery is based on an existing heat battery. The commercially available heat battery consists of a rectangular enclosure filed with the salt-hydrate HS48 as seen in Figure 1.2. Within the rectangular enclosure, a heat exchanger is placed, where hot and cold water streams exchange heat through a countercurrent stream as seen in Figure 1.2b. The system is powered by a 3 kW heat pump and can provide 8 kW of power that can replace a 200 L boiler commonly used in households.

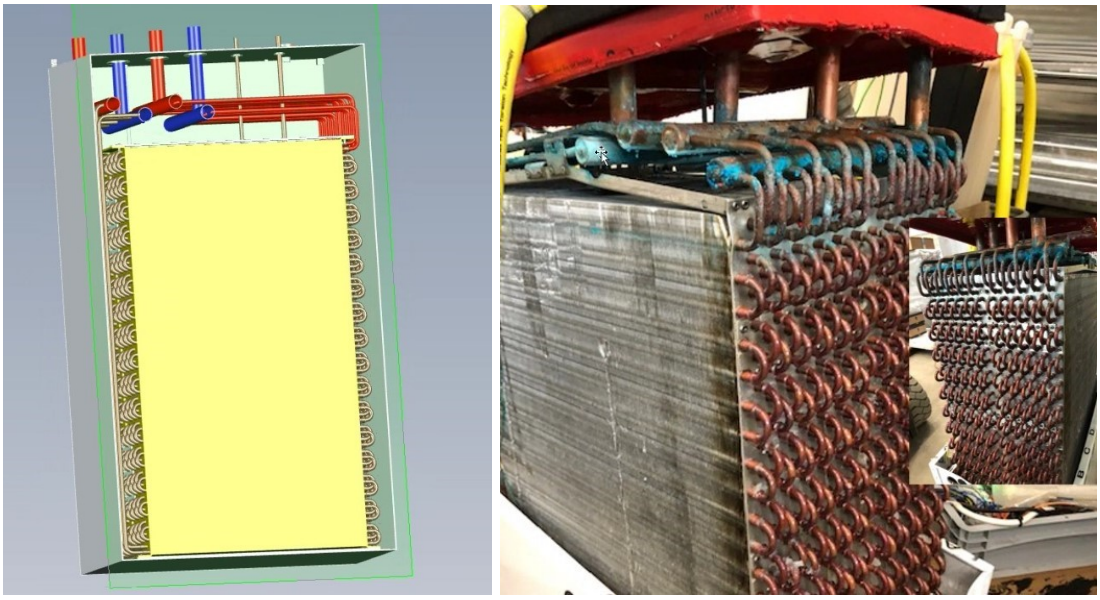

(a) 3D-model of the heat battery. **(b)** Tubing configuration of the heat battery.

Figure 1.2: Overview of the commercially available heat battery.

The commercially available heat battery is available in one size. The size is expressed in the power output the heat battery can supply, as well as the mass of PCM that is used. The heat battery is capable of providing 8 kW and consists of 110 kg of material. For certain applications, a latent heat storage system is required for higher or lower power outputs. This leaves the question of how to scale this type of heat battery and which considerations should be taken into account when scaling such a system. To the best of the authors' knowledge, this storage design in combination with the commercial salt hydrate has not been previously reported in the literature.

The aim of this study is to develop a model capable of scaling the commercially available latent thermal energy storage system with salt-hydrate HS48 as PCM. The scaling model should provide information on the optimal design parameters of the heat battery for different sizes and energy demands. Subsequently, the model is experimentally validated with a laboratory-scale storage design. When the model is validated with real-life data, it should be able to provide the optimal design parameters for a heat battery containing the phase-change material. The system will be evaluated in terms of power output, storage capacity, and average effectiveness during the charging and discharging processes. The goal of this thesis is formulated as follows:

The goal of this research is to develop a methodology that is capable of (1) developing a scaleable model based on an existing latent heat storage system, (2) evaluating the accuracy of the model with an experimental setup, (3) and providing the optimal design of the system based on a specific power demand .

1.3. Research questions

The main research question derived from the research goal is :

What will be the results of the optimisation of a latent heat storage system containing a salt hydrate as a phase-change material?

To adequately answer this research question, the methodology that will be developed must comply with certain accuracy and practical standards. These design requirements are translated into three sub-questions. Initially, the following subquestions must be answered, resulting in a proposed methodology capable of meeting the design requirements.

(1) How will the specifications and output of the latent heat storage system be affected when altering the scale of the system?

The precision of the method is partly determined by the dependence on the experimental data. Therefore, the second sub-question must be answered to validate this effectiveness and quantify the accuracy under different power demands.

(2) How accurate are the outputs of the latent heat storage system compared to the experimental data?

The method is capable of delivering an accurate output for the corresponding specifications, which will determine the scale of the system. To determine the optimal configuration, while providing a predetermined output in the form of power demand, the third sub-question has to be taken into account.

(3) What is the optimal design configuration of the latent heat storage system for a specific power demand?

By consecutively finding a solution for the subresearch question, a research method is developed providing the specifications that are needed to scale a thermal energy storage system containing phase-change material. The system will be evaluated for three different modes of operation: charging the system, discharging the system, and simultaneous charging and discharging of the system.

1.4. Outline

In Chapter 2, the theory and literature relevant for this research are discussed. Next, the proposed methodology is explained in Chapter 3. This methodology is carried out using a numerical analysis in Chapter 4. Thereafter, the experimental validation of the numerical model is performed and explained in Chapter 5. The results of the proposed methodology are presented in Chapter 6. A review of the results and several recommendations for future research are proposed in Chapter 7. Lastly, the conclusion of this investigation is formulated in Chapter 8.

2

Literature review

In this chapter, the relevant literature to this thesis topic is discussed. First, an overview of all the phase-change material relevant in the literature is presented in Section 2.1. A review of available TES systems containing phase-change material and other applications is given in Section 2.2. Lastly, in Section 2.3, a brief summary of this literature review is presented.

2.1. Phase-change material

Unlike conventional sensible thermal storage methods, PCMs provide much higher energy storage densities, and heat is stored and released at an almost constant temperature [4]. Considerable research has been done on the application of PCMs for heating and cooling a heat transfer fluid. PCMs are usually chosen on certain selection criteria [13]. These criteria can be divided into thermodynamic properties and kinetic properties. The theory on modelling PCM is given later, where the Stefan problem is described, as well as the heat rate of the phase-change material.

2.1.1. Selection criteria

A variety of solid-liquid phase-change materials are used for thermal storage applications, such as water, salt hydrates, paraffin, selected hydrocarbons, polymers, and metal alloys. Organic PCMs are composed of a wide range of materials, including paraffin, fatty acids, their eutectic mixtures, esters, and other organic compounds. Inorganic substances include salts, salt hydrates, hydroxides, and alloys [10]. Salt hydrates are inorganic salts that contain water of crystallisation. During phase transformation, the salt dehydrates, forming a salt hydrate with fewer water molecules. Depending on the melting behaviour, three types of melted salt behaviour can be identified: congruent, incongruent, and semi-congruent melting [4].

Thermodynamic properties

Phase-change materials are typically classified by their melting temperatures. The melting point, or sometimes the liquefaction point, is the temperature at which a substance transitions from a solid to a liquid state [14]. When selecting a PCM for a particular application, it is important to ensure that the melting temperature is within the practical range of the application [4]. Low-temperature PCMs have melting points below 15 °C, mid-temperature PCMs range between 15 and 90 °C, and high-temperature PCMs have melting points above 90 °C [15].

The enthalpy of fusion of a substance, also referred to as its latent heat of fusion, is the amount of energy, usually in the form of heat, required to transform a specific quantity of the substance from a solid to a liquid state, while keeping the pressure constant [16]. Paraffins have melting temperatures ranging from -12 °C to 71 °C, and their heat of fusion ranges from 190 to 260 J/g. Non-paraffins or fatty acids have melting points between 7.8 °C and 187 °C, and their heat of fusion ranges from 130 to 250 J/g. Salt hydrates have melting points between 11 °C and 120 °C, and their fusion heat ranges from 100 to 200 J/g. Eutectics have melting points between 4 °C and 93 °C, and their fusion heat ranges from 100 to 230 J/g [17]. The amount of phase-change material required to meet the heat needs of households is determined by the thermal energy storage capacity [18]. This capacity is determined by

the latent heat of fusion and the specific heat of liquid and solid PCMs, which are used to store latent and sensible heat, respectively. To reduce the size of the system and improve its thermal efficiency, a large thermal storage capacity is essential.

Conventional phase-change materials, both organic and inorganic, have a very low thermal conductivity, ranging from 0.1 to 0.6 W/mK. This is not suitable for applications in low-heat-transfer energy storage systems due to slow charging and discharging rates [5]. To increase thermal conductivity, various techniques can be used, such as adding materials with high conductivity, using finned tubes with different configurations, inserting PCM into a metal matrix, micro encapsulating, and impregnating porous materials with PCM [10].Materials that experience a phase transition are characterised by a change in density. This change, which can reach 10%, can lead to a decrease in volume due to solidification, resulting in the formation of gaps and a gap between the PCM and its container, which would have a major effect on performance [19].

Kinetic properties

The phenomenon of supercooling leads to an imbalance between the processes of solidification and melting, preventing the phase change from occurring at the expected temperature [20]. This implies that no true phase shift occurs when a liquid PCM is cooled to its solidification temperature, and that the liquid state persists until the liquid is cooled further to a different temperature, resulting in a low heat storage capacity. Although temperature changes are often minor in PCM applications, supercooling is still a factor to consider when it comes to energy recovery.

Crystallisation is triggered when the temperature decreases to a certain value, which can be affected by impurities or actual working conditions, and then the temperature increases rapidly toward the phase transition temperature [21]. Generally, the degree of supercooling required for the crystallisation of hydrated salts is high and inconsistent; studies show that it can even exceed 50 °C. This leads to a sudden, large release of latent heat at the start of solidification, as well as a decrease in the heat released during the subsequent discharge process. Consequently, supercooling has a major impact on the heat release curve of the heat storage unit. For this reason, it is essential to take into account the supercooling state, the growth of crystallisation, and the change in temperature during the solidification process in PCMs [22].

In order to ensure that chemical degradation does not occur after a certain number of temperature cycles, the storage medium must be stable. The durability of characteristics with prolonged cycling, as well as changes in density and supercooling of phase-change materials, present practical difficulties in the application of the latent heat method [23]. One of the main issues of cycling stability is phase separation. When a PCM is composed of multiple components, phases with different compositions can form when cycling. Phase separation is the effect that phases with different compositions are separated from each other on a macroscopic level. Phases with a composition that is different from the initial composition optimised for heat storage then demonstrate a significantly lower capacity to store heat. The economic viability of using a phase-change material depends on its service life, during which there should be no major changes in the melting temperature or latent heat of fusion caused by the operational thermal cycling of the storage material. Two factors are responsible for the inadequate long-term stability of storage materials: poor stability of the materials themselves and/or corrosion between the PCM and the container [10].

To ensure that thermal energy can be released or absorbed at the necessary rate, a good heat transfer rate must be maintained between the heat storage material and the heat transfer fluid. The phase change temperature has a direct effect on the rate of latent heat release and storage, with a lower melting temperature allowing the storage process to begin earlier at a lower water temperature. However, this lower melting temperature will also delay the start time of solidification for heat release. The heat transfer rate is increased by a greater temperature difference, but the power that can be drawn from the energy storage system is limited by the poor thermal conductivity of the PCM. Research has shown that the intermittent availability of the water mass flow rate, as well as natural and induced convection during charging and discharging, causes discharge to occur more quickly than charging [24].

2.1.2. Theory

Simulating the behaviour of charging and discharging the PCM is usually described by the Stefan problem. The theory behind the Stefan condition is derived from the book of Mills [25].

The Stefan problem is a type of boundary value problem for a system of partial differential equations in which the boundary between two phases of a material can move over time. This problem is used to describe the evolution of the boundary between two phases of a material that undergoes a phase change. In the context of PCM, the temperature profile responds to changes in boundary conditions much faster than the position of the melting front (x^*). This means that even though the melting front can move, the temperature profile quickly assumes the form it would have if the melting front were fixed at its current position, known as the quasi-static temperature profile. Once the quasi-static profile is established, the time evolution of T is slow, and the diffusion equation becomes $\partial^2 T/\partial x^2 \approx 0$, which can be solved for the quasi-static temperature profile in the material. This profile is linear, $T = mx + b$, with a slope m and an offset b determined by the boundary conditions. In a system made up of slabs of different materials, the temperature profile will be linear with a different slope for each material.

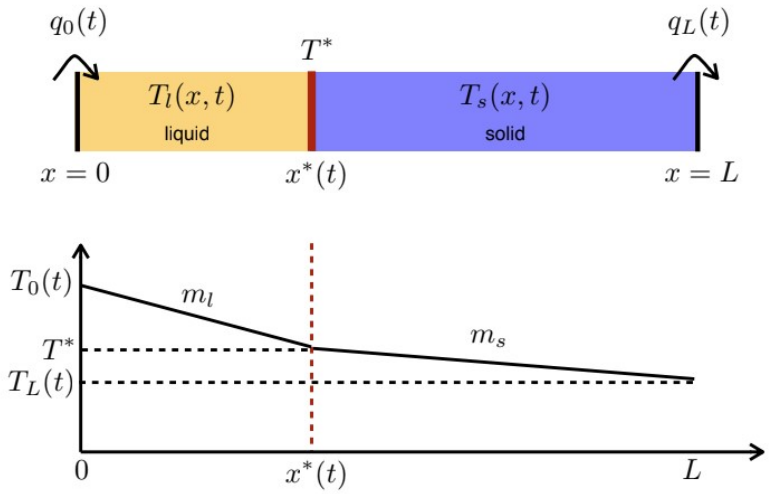

Figure 2.1: (top) A quasi-1D PCM. (bottom) A quasi-static temperature profile.

The material has boundaries at $x = 0$ and $x = L$. The interface between the liquid and solid phases occurs at x^*, where the temperature is T^*, which is the melting temperature. The boundary conditions must be applied at $x = 0$, $x = L$, and the melting front $x = x^*$. This poses a unique challenge in heat transfer within PCMs, since the position of the melting front is not known in advance. The slope of the temperature profile between x_1 and x_2 is given in Equation 2.1. Heat is flowing through both the liquid and solid portions of the PCM, with the heat flux through the liquid being higher than that through the solid, as some of the heat is used to convert the solid to liquid. The power per unit of surface area delivered to the melting front is given in Equation 2.2, where the subscripts s and l refer to the solid and liquid, respectively. The latent heat of melting of the PCM is $h_s l$. The energy balance requires that the melting front advances by a distance dx^* in time dt, which is represented in Equation 2.3. Introducing $v^* = dx^*/dt$ for the velocity of the melting front, the above can be rewritten as Equation 2.4.

$$\frac{\partial T}{\partial x} = m = \frac{T(x_2) - T(x_1)}{x_2 - x_1} \tag{2.1}$$

$$P = q_l - q_s = -k_l m_l + k_s m_s \tag{2.2}$$

$$\rho h_{sl}\, \mathrm{d}x^* = P\, \mathrm{d}t \tag{2.3}$$

$$\rho h_{sl} v^* = -k_l \left(\frac{T^* - T_0}{x^*} \right) + k_s \left(\frac{T_L - T^*}{L - x^*} \right) \tag{2.4}$$

The Stefan condition, which is specialised in quasi-static temperature profiles, is described in Equation 2.4. The condition states that the velocity of the moving front is determined by the difference in the slope of the temperature profile on either side of x.

2.2. Latent heat storage systems

In this section, the different configurations of latent heat storage systems, used for domestic water heating systems, are reviewed. Three main options, as described in the literature, are a hot water storage tank filled with PCM modules, a storage tank made of a PCM slab with copper pipes integrated in the tank, and a version of the latent heat storage system where the PCM is arranged concentric to the flow line.

Copper pipes integrated in the PCM storage tank

Hassan and Beliveau [26] discussed the creation of a newly designed collection system. As seen in Figure 2.2a, the heating energy is kept in the PCM, which is housed in a properly insulated cylindrical tank. The parallel copper pipes in the storage tank are attached to the heat source and are used to transmit hot fluid from the source to the PCM to transfer heat. Compared to typical system design, the developed system offers significant cost savings, suggesting that the adoption of this system is promising. The proposed system could supply a minimum of 88 % of the hot water requirements throughout the year, thus reducing the need for non-renewable energy [2].

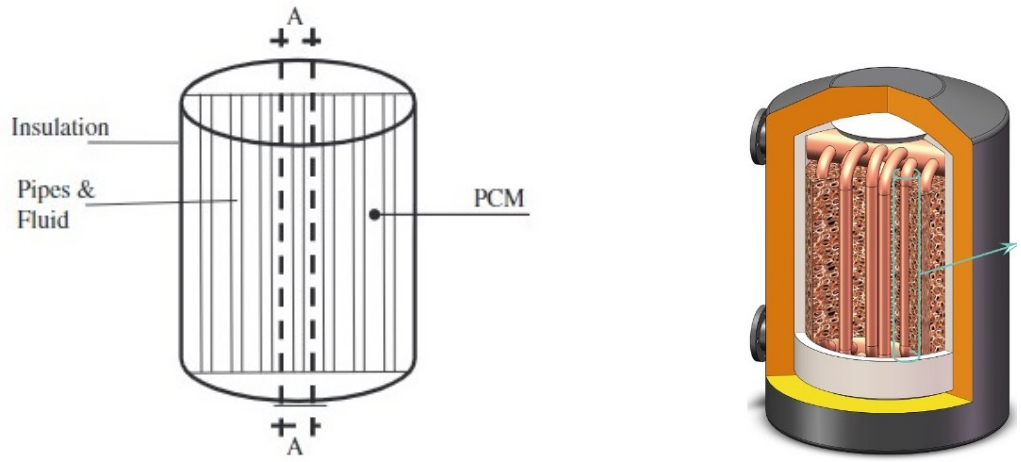

(a) PCM storage tank [26]. **(b)** Thermal energy storage tank [27].

Figure 2.2: Separate thermal energy storage units as described in the literature.

According to Liu et al. [27], a unique energy storage tank is proposed filled with phase-change materials and graded metal foams. The thermal energy storage tank is shown in Fig. 2.2b with the volume of the shell completely filled with metal foams and PCM. The top injection inlet is used for the passage of heat transfer fluid. HTF with a lower temperature exits the tank outlet after energy charging. The results show that the melting and solidification processes are not impacted by the pore density gradient design. Comparing a design with graded porosity to one without reduces the total melting time by 21.1 %. Furthermore, the ideal porosity gradient shortens the total duration of the melting and solidification cycle by 10.9 %.

PCM packed in hot water storage tank

Morrison et al. [28] describes a phase-change energy storage used in heating systems. The storage container consists of a tank that is vertically filled with cylindrical tubes, as seen in Fig. 2.3a. The heat transfer fluid flows parallel to the PCM as it is housed inside the tubes. The PCM storage unit of each tube is thought to operate independently of the others [29, 30, 28]. The water-based technology enables simultaneous charging and discharging of the storage unit. When the storage unit is in the charging phase, a heat transfer fluid captures the radiation heat and transfers it to the storage. The cylindrical latent heat storage device described is a component of a domestic hot water system. Using these types of storage has the fundamental benefit of collecting heat at a steady temperature. The additional benefit of the comparative latent heat storage method is discovered to be limited in the range of 25 % of the storage volume. However, the seasonal variations in the latent heat storage system's efficiency will force over-optimisation of size, negating the benefit of compactness. [28, 29].

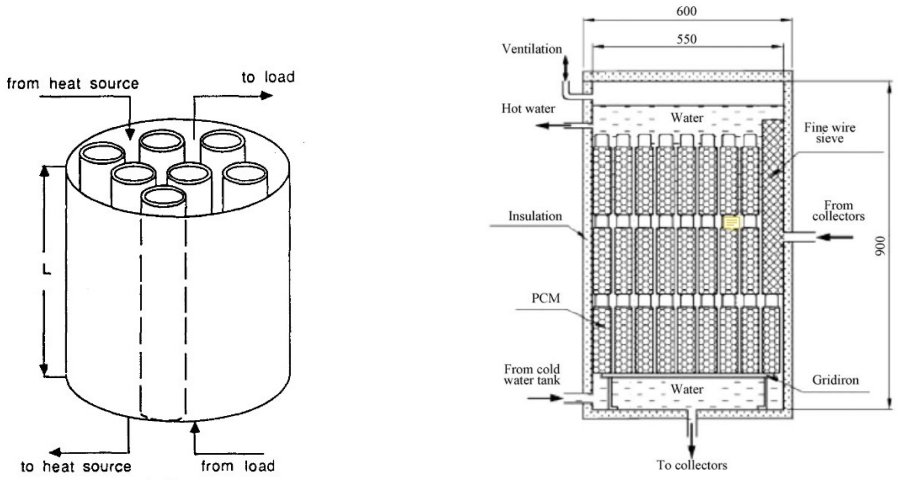

(a) The cylinder-packed vessel [30].

(b) Cross-section of the storage unit [31].

Figure 2.3: Storage systems with the PCM packed in hot water storage tank.

Canbazoglu et al. [31] provide a well-insulated cylindrical galvanised steel heat storage tank equipped with PCM. Glass wool is used as insulation. The three rows of polyethylene bottles, each of which contained PCM, were placed in the tank as depicted in Fig. 2.3b. Multiplying the amount of barrels increases the heat transfer surface for PCM. The water temperature at the midpoint of the storage tank was observed to decrease steadily during the day until it reached the phase change temperature of the PCM. After the heat source strength decreased, it stabilised at 46 °C for around 10 hours at night. In the water heating system, a mass flow of hot water is produced with an overall heat accumulation of 2.5 to 3.5 times that of conventional water heating systems.

Mazman et al. [32] present a latent heat storage system that could operate with an electrical heater. To implant the PCM module, the two water tanks had been modified [2]. Multiple cylinders were used at the top of the water tank as part of the PCM module geometry. As seen in Fig. 2.4a, there are modules of regular aluminium bottles filled with similar volumes of PCM. The system is able to provide hot water for extended periods of time without an external energy source. This is achieved by including a PCM module in water tanks for household hot water supply, or by using smaller tanks with the same function. The stored water temperature remained at least 30 °C higher than the outside temperature during the course of the 24-hour test period. According to Al-Hinti [33], the use of brief forced circulation intervals had the least impact on the functioning of the system.

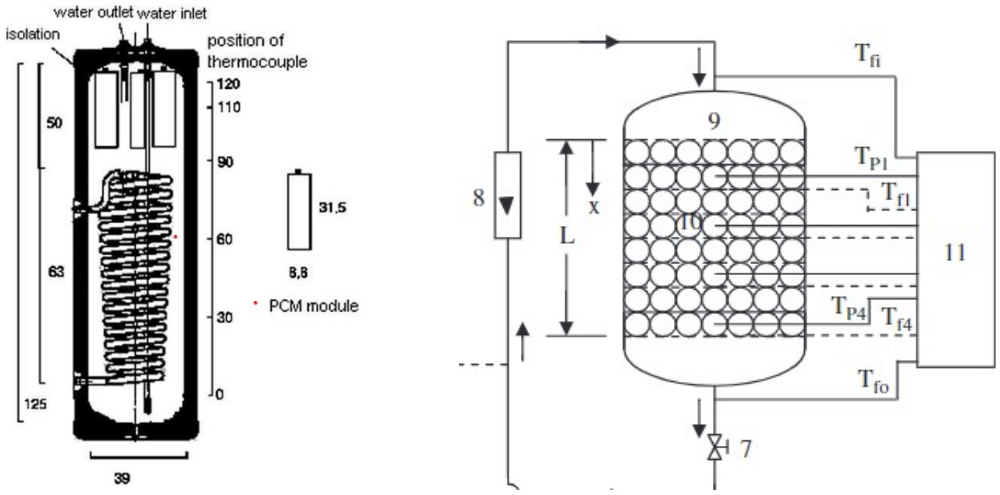

(a) Domestic hot water tank with the PCM module [32].

(b) TES tank [34]

Figure 2.4: PCM systems with integrated in a domestic hot water tank.

Nallusamy et al. [34] created an integrated thermal energy storage unit with a packed bed that can store sensible and latent heat. As shown in Fig. 2.4b, the thermal energy storage unit uses paraffin as phase-change material filled in spherical capsules that are packed in an insulated cylindrical storage tank. Water is employed as the heat transfer fluid. According to the results of the discharge studies, the combined storage system that uses hot water discharge from the TES tank is best suitable for applications with sporadic demand.

Concentric to the flow line

A third way to implement PCM in a domestic flat plate solar water heating system is by placing PCM concentric to the flow line of the heat transfer fluid. This configuration is described by Malvi et al. [35]. There are various flow configurations, namely serpentine flow, wall-to-wall parallel flow, and spiral flow.

In the latent heat storage system, paraffin wax is utilised as the phase-change material in a sheet-and-tube-type collector where the tubes are attached to the absorber plate by a suitable adhesive. In a serpentine flow, a single integrated length of tubing is used to create a fluid that flows in a zigzag or serpentine pattern. In a parallel wall-to-wall flow, water flows through channels with a rectangular cross section. These channels offer a smooth passage for the flow of water because they do not have steep curves. The spiral flow runs through a polymer tube filled with PCM, and then water tubes were inserted to study the spiral flow in a tube-in-tube heat exchanger. The heat removal factor of the configuration is proportional to the melting temperature of the PCM. The factor depends on the melting and solidification phases of the PCM rather than the mass flow. The results show that for a mass flow rate of 1 kg/hr of water, the heat removal values for serpentine and parallel wall-to-wall flow are, respectively, 0.44 and 0.88. In the context of PCM, it was noted that the factor has a value ranging from 0 to 0.28. Furthermore, it has been found that the value in a traditional water heater with serpentine flow or parallel wall-to-wall flow does not increase appreciably above a mass flow rate of 4 kg/hr.

Other Applications

Latent heat storage systems are often combined with solar collectors to establish a solar water heater. Solar water heaters can be incorporated with PCM in three ways: under the collector absorber plate, a separate thermal energy storage unit or concentric to the flow line[36]. The requirements that the results should meet are phase-change material such as latent heat storage, water-based flat plate solar collectors (preferably sheet and tube), and they should be used to power residential appliances like domestic hot water or space heating.

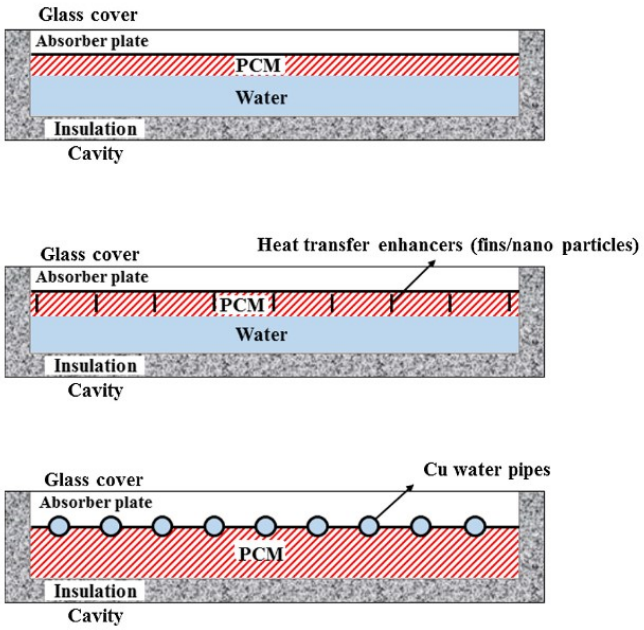

Figure 2.5: Solar collector designs with PCM placed under the collector absorber plate [36].

The first method to improve the thermal performance of a flat-plate solar collector was to integrate PCM. As illustrated in Figure 2.5, three general categories can be used to classify the majority of PCM integrated designs. The first is a design in which the PCM is placed beneath the collector and is in direct contact with water. Second, with PCM that has been increased for heat transfer in direct contact with water, and third, with copper pipes that have PCM surrounding them and water flowing through them [36].

Another common application for PCM is as thermal management in buildings. The use of PCMs in buildings can have two different objectives. First, take advantage of natural heat and cold sources, such as solar energy for heating or night cold for cooling, and second, use man-made heat or cold sources. In either case, it is necessary to store heat or cold to match availability and demand with respect to time and power. Generally, there are three different ways to use PCMs for the heating and cooling of buildings: PCMs in building walls; PCMs in other building components than the walls; and PCMs in separate heat or cold stores. The first two are passive systems, where stored heat or cold is automatically released when indoor or outdoor temperatures exceed the melting point. The third is an active system, where stored heat or cold is thermally separated from the building by insulation and is only used on demand and not automatically [13].

Research can be divided into innovation of new configurations that combine heat sources with phase-change material storage, and research done on the material characteristics of phase-change material. The specific configuration of (copper) water pipes in separate PCM storage tank seems the most promising for further research. Possible research could be in finding the optimal tubing configuration through this PCM tank. The optimisation will be determined by the melting distribution near the tubing and the optimal melting in the corners of the tank, thereby optimising the mass needed for thermal energy storage. Another field of research would be the optimisation of the PCM simultaneously charging and discharging.

2.3. Chapter Summary

This chapter provides a comprehensive review of the literature related to the thesis topic. It begins with an overview of phase-change materials (PCMs) and their properties, discussing selection criteria based on thermodynamic and kinetic properties. The chapter then delves into the theory of PCM behaviour, particularly the Stefan problem, which describes the movement of the melting front within PCM materials. Next, the chapter explores various latent heat storage systems using PCM. It discusses configurations where PCM is integrated into hot water storage tanks, including designs with copper pipes, cylindrical modules, and spherical capsules. In addition, it presents systems where PCM is placed under solar collector absorber plates and systems where PCM is used for thermal management in buildings. This review also highlights the advantages and challenges associated with each PCM storage system. Throughout the chapter, the focus is on practical applications, such as domestic water heating systems and solar water heaters, with a consideration of how these systems can effectively utilise PCM to store and release thermal energy.

In summary, this chapter comprehensively examines the literature related to PCM properties, theory, and practical applications in various energy storage systems, providing a solid foundation for the research and analysis.

3

Methodology

In this paper, a methodology is proposed to find the optimal design of a latent heat storage system. This methodology is based on the heat transfer principles of a phase-change storage unit and the specifications of the heat battery developed by the commercially available. First, the general idea of the methodology is discussed in Section 3.1. Thereafter, the detailed structure of the methodology and several considerations of the system are described in Section 3.2. Lastly, a hypothesis of the methodology is given in Section 3.3.

3.1. General idea

In this methodology, the latent heat storage system is based on the commercially available heat battery. The battery can provide 8 kW of power and is usually charged by a 3 kW heat pump. The established design consists of a rectangular enclosure, where a heat exchanger is placed within the enclosure. The heat exchanger is composed of two separate flows, a hot water flow to charge the system and a cold water flow to discharge the system. These flows are regulated through an open divider. This open divider divides each flow into 10 parallel copper tubes, where each individual tube follows a specific pathway that compromises a total of 32 passes, as seen in Figure 3.1. To enhance the poor thermal conductivity of the PCM, a total of 58 aluminium plates are inserted into the PCM for every 10 cm in the x-direction. The PCM that is being used is HS48, an inorganic salt hydrate PCM developed by the company PLUSS.

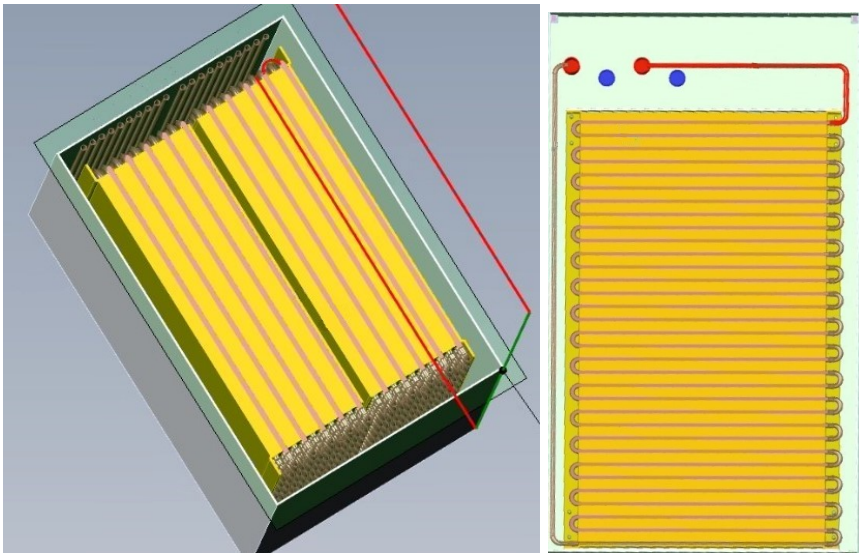

(a) Number of parallel tubes. **(b)** Number of passes per tube.

Figure 3.1: Cross-sectional view of the commercially available heat battery

To provide a model capable of simulating the outputs of the commercially available heat battery, this methodology uses the characteristics of heat transfer for phase-change materials. Morrison [28] developed a model applicable to phase-change materials in rectangular units. The model uses the method of formulation of enthalpy. This, unlike the Stefan problem, does not require tracking of the phase interface. The main reason for using this model to simulate the latent heat storage system is the lack of accurate tracking of the liquid interface when performing the experiments. Heat transfer fluid passes through the storage unit in the x-direction at a rate $\dot{m}$ and with an input temperature $T_{f,i}$ as shown in Figure 3.2. Here, the length in the flow direction is L.

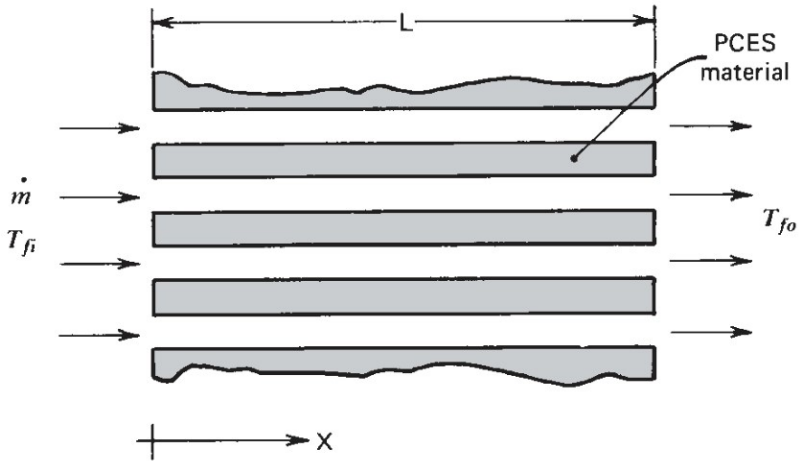

Figure 3.2: Schematic of a phase change storage unit [28].

The model developed by Morrison is based on certain assumptions. Assumptions directed at the properties of phase-change materials are defined in the form of three criteria. Phase-change material can serve as energy storage, provided that these criteria are met. Firstly, the phase transition must be accompanied by a high latent heat effect. Secondly, the phase-change process should be reversible over a large number of cycles without experiencing serious degradation. Third, it is desirable that the phase transition occurs with minimal supercooling or superheating.

The assumptions regarding the heat transfer of the flow are that during flow, the axial conduction in the fluid is negligible. Other assumptions are that the Biot number is low enough that temperature gradients normal to the flow can be neglected; the fluid capacitance is low; and heat losses to the surroundings are zero.

Regarding the heat transfer in the PCM, the model only takes into account the ideal reversible phase change. This, in other words, means that no supercooling or superheating occurs. Finally there is only conductive heat transfer within the PCM unit, meaning that convectional heat transfer is negligible during phase change.

If a phase-change material is heated from the reference temperature (T_{ref}) to the maximum operating temperature of the material (T_{max}), it undergoes a phase transition at the melting temperature (T^*). The storage capacity of the phase change is then determined by : the sum of the sensible heat change of the solid phase from T_{ref} to T^*, the latent heat at T^*, and the sensible heat of the liquid from T^* to T_{max}. This is shown in Equation 3.1. Note that the storage capacity equals the total charged energy. The total discharged energy is the reverse procedure. Latent heat, which is added at the melting temperature, can be regarded as a high specific heat over a very small temperature range.

$$Q_s = m\left[C_s\left(T^* - T_{ref}\right) + \lambda + C_l\left(T_{max} - T^*\right)\right] \tag{3.1}$$

The thermal resistance to heat transfer within the material is variable depending on the degree of solidification and whether the material is heating or cooling [37]. When heat is removed from a material that undergoes a phase change, the process in which the material crystallises starts at the outer edges and gradually progresses toward the core of the material. Once this crystallisation process is complete, heat needs to move through the solid layers to reach the container walls. On the other hand, when heat

is added to the solid material, it starts to melt initially at the containers' walls and then spreads inward toward the centre of the container. If the containers are designed in a way that shortens the distance for heat to travel internally, the melting and solidification will be less time-consuming. Therefore, the paths for internal heat transfer should be as short as possible [22].

Taking the assumption that axial conduction during flow is negligible and fluid capacitance is low, the energy balance on the phase-change material is given in Equation 3.2. Where u, T, K, and ρ are the specific internal energy, temperature, thermal conductivity, and density of the phase-change material respectively. The average temperature of the heat transfer fluid is T_f, the cross-sectional contact area of the phase-change material is A_{PCM}, the wetted perimeter is P, and U is the overall heat transfer coefficient between the fluid and the phase-change material. The equation describes the change in internal energy over time per kilogram of phase-change material. Note that the fluid temperature is taken over time but averaged over the length of the channel.

$$\frac{\partial u}{\partial t} = \frac{UP}{\rho A_{PCM}} \left(T_f - T\right) \tag{3.2}$$

The specific internal energy u is a function of the temperature of the phase-change material T, which is taken as a uniform value, the liquid fraction χ, and the specific heats of the liquid and solid phases C_l and C_s. Determining the specific internal energy requires a different approach for when the PCM temperature is below, equal to, or above the melting temperature T^*, as shown in Equation 3.3. Here T_{ref} is the reference temperature at which the internal energy is taken as zero, in most cases the room temperature of 293 K.

$$u = \begin{cases} C_s \left(T - T_{\text{ref}}\right) & \text{if } T < T^* \\ C_s \left(T^* - T_{\text{ref}}\right) + \chi\lambda & \text{if } T = T^* \\ C_s \left(T^* - T_{\text{ref}}\right) + \lambda + C_l \left(T - T^*\right) & \text{if } T > T^* \end{cases} \tag{3.3}$$

As the heat is added to the phase-change material, the heat is extracted from the heat transfer fluid. From the assumptions that axial conduction during flow is negligible and the fluid capacitance is small, the energy balance in the heat transfer fluid is described by Equation 3.4. Where ρ_f, A_f, and C_f are the density, flow area, and specific heat of the fluid. The energy balance is able to determine the temperature of the HTF over a certain length, thus returning values for the inlet and outlet temperatures of the storage system.

$$\frac{\partial T_f}{\partial x} = \frac{UP}{\left(\dot{m} C_p\right)_f} \left(T - T_f\right) \tag{3.4}$$

The charging or discharging power can now be determined with Equation 3.5. Here, the discharging power is one of the parameters that determines the scale of the system needed to supply a certain power demand. In the case of the commercially available heat battery, this is a value of 8 kW.

$$\dot{Q} = \dot{m} C_{p,water} (T_{f,0} - T_{f,i}) \tag{3.5}$$

With the equations provided for the discharging power, the melting distribution and the storage capacity can be determined for the phase-change storage unit developed by Morrisson. The challenge lies in projecting the theory onto the commercially available heat battery and still providing accurate results. To achieve this, a number of assumptions need to be made to relate the model to the heat battery.

One of the characteristics of the Morrison model is that the PCM is enclosed in rectangular units. To match the heat battery with the model, assumptions are made that the PCM that retrieves the heat is divided into rectangular sections. As shown in Figure 3.3, the parallel tubes deliver heat (when charging) to the rectangular units on both sides. This means that the phase-change material between the passes is not taken into account. The rectangular units have a width of dy, which is the distance between the parallel tubes. The length of the rectangular units should be long enough to fit the length of a single pass (L_{tube}). The surface area of the phase-change material is A_{PCM}, which in this case is L_{tube} multiplied by the height of the enclosed phase-change material (z_{PCM}).

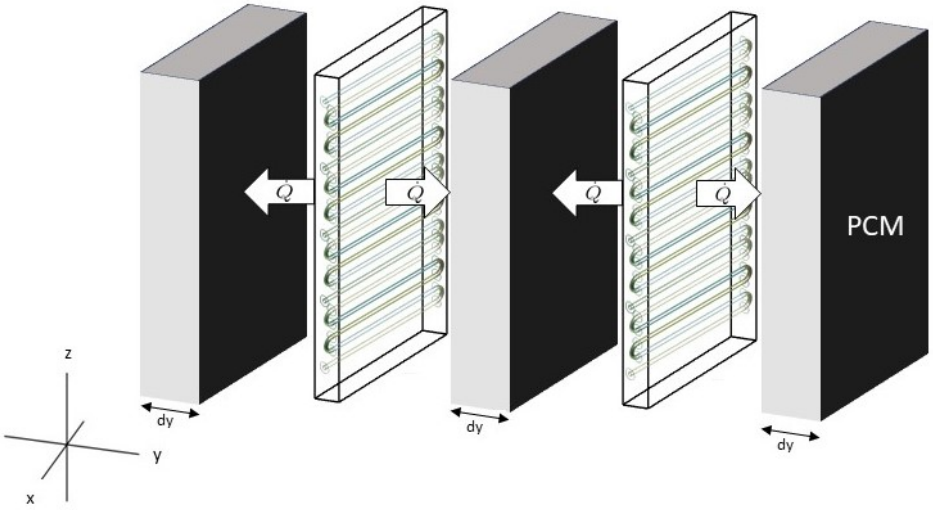

Figure 3.3: Schematic of heat transfer in heat battery model.

The assumption of not taking into account the material between the passes is based on the temperature difference. The temperature difference of the HTF from the start of one pass to the end of the next pass is very low. The temperature difference of the HTF between the hot and cold circuits is very large; therefore, the heat transfer between two passes is negligible. In other words, the heat transfer in the z-direction is zero. Similarly to the temperature difference of the HTF between two passes, the heat transfer over one pass is even smaller, meaning that heat transfer in the x-direction is also negligible. With both of these conditions set, it can be assumed that there is no heat transferred to the material in between the passes of individual tubes.

Due to the countercurrent design of the heat exchanger, and the fact that the heat capacitance is largest when heat is transferred from the hot circuit to the cold circuit, we can assume that heat transfer will dominate in the y-direction. To match the model with the heat battery, the assumption to be made is that the heat transfer in the phase-change material is one-dimensional. In other words, the heat flow is one-dimensional between the HTF and the PCM in the phase change profile that is moving in the y-direction [38].

The thermal resistance which is incorporated into the overall heat transfer coefficient, in Equation 3.2 and Equation 3.4. Note that the overall heat transfer coefficient U depends on the state of the PCM and the flow rate inside the tubes. The thermal resistance to heat transfer within the material is variable depending on the degree of melting and whether the material is heated or cooled [22]. To approach the thermal resistance, the assumption of one-dimensional heat transfer is key. In more detail, it is assumed that the phase change occurs in one-dimensional form from the internal surface of the tube to an external boundary in the PCM [38]. For one-dimensional conductive heat transfer between the HTF and the PCM, the heat transfer is determined through a thermal resistance network. The thermal resistance network is based on an insulated steam pipe described by Mills [25]. The relation between these parameters is described in Figure 3.6. A more in-depth description of the determination of the overall heat transfer coefficient is given in Section 3.2.

$$\frac{1}{UA_f} = R_{HTF} + R_{wall} + R_{PCM} \tag{3.6}$$

With the assumptions given, the methodology should be able to provide a model capable of simulating the heat transfer within the commercially available heat battery. The model is dependent on the dimensions and mass of the phase-change material in use. By altering these parameters, the model should be able to scale size and be able to supply a certain power demand. To validate the scaleable model, a design of a heat battery at a laboratory-scale size should be numerically modelled. In Chapter 4 the original size and the size on the laboratory scale are numerically analysed. A detailed description on how to scale the specifications of the system is given in Section 3.2.

From the findings of this chapter, the experimental validation will be conducted in Chapter 5. To

provide an accuracy of the methodology, the model is validated by the experimental set-up. With the corresponding inputs and outputs, the scale-able model is validated, and thus it can provide a simulation of the heat battery for different sizes.

To provide favourable outcomes for the validated model, the system is optimised by enhancing the thermal conductivity of the phase-change material and creating a more compact design. How to achieve this is described in 3.2. Therefore, the optimised model will be able to provide a power output of 8 kW, for a specific amount of PCM mass and a fixed mass flow rate. To further analyse the performance of the system, a model will simulate different design configurations of the system with a fixed mass of phase-change material. To approach this the design is computed in three ways, which are expressed on the independent variables in the model: the length of the tube for a single pass (L_{tube}), the number of tubes (N_{tubes}), and the number of passes (N_{passes}) [39]. These parameters are intrinsically related to, respectively, x_{cube}, y_{cube}, and z_{cube}. These three configurations will be evaluated on the optimal design. The testing parameters of performance will be: charging/discharging power of the system, temperature outlet of the system, time of charging / discharging, and average effectiveness's of the system. The optimisation process is described in Section 3.2.

3.2. System considerations

The methodology provides a solution to the proposed research of: What will be the optimal design of a latent heat storage system containing a salt hydrate as a phase-change material? To find the optimal design, a model must be developed that describes the heat transfer characteristics of the heat battery (1) , also the model must be able to scale the specifications based on a certain power demand (2), finally the optimal design is assessed through the outputs of three distinct configurations (3).

3.2.1. Determining the overall heat transfer coefficient

As described in the previous section the overall heat transfer coefficient U depends on the state of the PCM, and the flow rate of the heat transfer fluid. Thermal resistance to heat transfer within the material is variable depending on the degree of solidification and whether heating or cooling of the material is occurring. To determine the overall heat transfer coefficient, Equation 3.6 is used. An overview of the specific components of the thermal resistance network is shown in Figure 3.4.

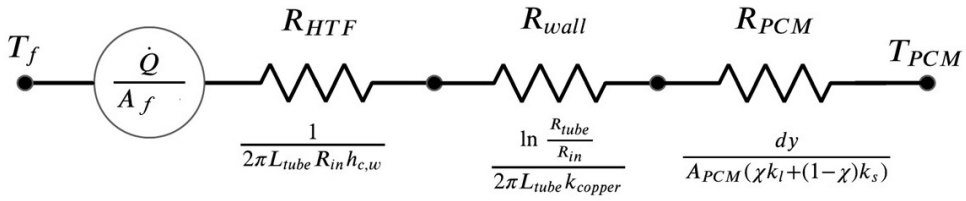

Figure 3.4: Thermal network of the resistances applied in the PCM system

Note that here the value of A_f is the total surface area of the tube. For the charging sequence, the initial liquid fraction is zero ($\chi = 0$) . The thermal resistance of the phase-change material (R_{PCM}) dominates due to the low thermal conductivity of the solid PCM (k_s). The relation of adding heat to solid PCM becomes $R_{PCM} > R_{HTF} > R_{wall}$. When melting occurs, the conductive resistance increases at the liquid interface and decreases at the solid interface. Note that in this model, we use a uniform PCM temperature, which means that no more heat is added to the heating of the solid PCM, but only the resistance is due to the PCM melting when $T = T^*$. When the PCM is fully melted ($\chi = 1$), the PCM temperature starts to rise again when all the heat is used to heat the liquid PCM. When the system is discharging, the thermal effects described in this case will be reserved. When charging and discharging simultaneously, the liquid fraction can be established as $\chi = 0$ or $\chi = 1$, depending on whether the system is simulated for a solid state or a molten state.

To determine the thermal resistance induced by the heat transfer fluid (R_{HTF}) the convective heat transfer coefficient of the flowing water should be determined by Equation 3.7. To determine the Nusselt number, the Reynolds number of the flow should be determined. The hydraulic Reynolds number is

found by Equation 3.8. The model takes into account the amount of power charged by a single tube. Therefore, the mass flow rate is used for a single tube. Mass conservation shows that, for dividing the flow into N tubes, the mass flow rate to determine the Reynolds number is defined by: $\dot{m}_{tube} = \frac{\dot{m}_{total}}{N_{tubes}}$. The mount of power needed to melt the entire mass of PCM is determined with the total mass flowrate, see Equation 3.5.

$$h_{c,w} = Nu\frac{k_{water}}{L} \tag{3.7}$$

$$Re_D = \frac{\dot{m}_{tube} D_{in}}{\mu A_{tube}} \tag{3.8}$$

$$\mathrm{Nu}_D = 0.023\,\mathrm{Re}_D^{4/5}\,\mathrm{Pr}^n \tag{3.9}$$

$$Pr = \frac{v}{\alpha} \tag{3.10}$$

The Nusselt number is assessed with the Dittus-Boelter equation [38], see Equation 3.9. Where $n = 0.3$ for cooling and $n = 0.4$ for cooling and heating, respectively. The equation is an explicit function to calculate the Nusselt number. It is easy to solve but less accurate when there is a large temperature difference across the fluid. Pr is the Prandtl number and is determined by Equation 3.10.

The thermal resistance of the wall (R_{wall}) is a function of the dimensions of the tube and the thermal conductivity of copper. Because of the small wall thickness of the tubes, the thermal resistance due to the wall is as good as negligible compared to the thermal resistance of the phase-change material.

To determine the thermal resistance of the phase-change material (R_{PCM}), the length of the melted material is needed. From 3.3 it is established that this length is the distance between parallel tubes and is described as dy. When charging, the length dy is the distance between two tubes that include the hot circuit. Note that heat will be transferred in both directions on the y-axis, so the distance $dy/2$ actually melts in both directions but is also emitted from the next tube of the hot circuit. Therefore, the distance dy, as shown in Figure 3.5a, is the value inserted into the equation for R_{PCM}. When discharged, this value is the same. However, now the heat is extracted from the material and transferred to the cold circuit, as shown in Figure 3.5b. When charging and discharging simultaneously, both the hot and cold circuits are running. Therefore, the distance dy is taken as the distance between the hot and cold circuits; see Figure 3.5c. The value of A_{PCM} in determining R_{PCM} is the contact surface of the rectangular slab with width dy.

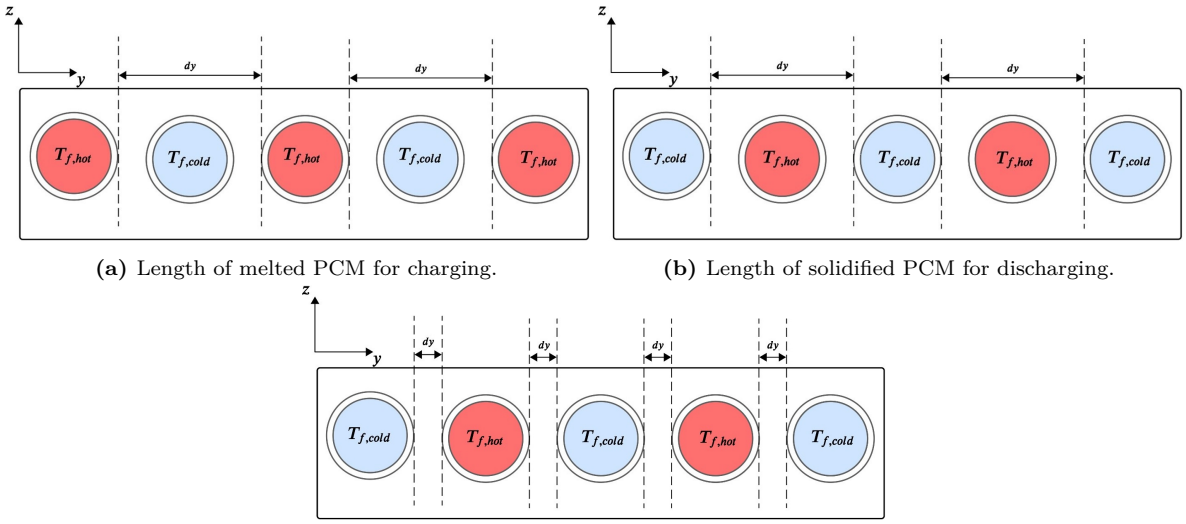

(a) Length of melted PCM for charging.

(b) Length of solidified PCM for discharging.

(c) Length of PCM for simultaneous charging and discharging.

Figure 3.5: Length of the heat transfer characteristic dy, for determining R_{PCM}.

3.2.2. Scaling through the independent variables

To provide an accurate scale-able the independent variables have to be determined. This is only possible by setting a couple of constant values in the design that are not affected by scaling. An overview of all the constants in the design is given in Table 3.1.

Table 3.1: Constants and relations for scaling the dimension of the storage system.

Dimension	Value	Dimension	Relation
R_{out}	3 mm	R_{in}	R_{out} - d_{wall}
d_{wall}	0.8 mm	x_{cube}	Sy_{cube}
x_{bends}	9 mm	x_{tube}	x_{cube} - $2x_{bends}$ - $2x_{tubes,walls}$
$x_{tubes,walls}$	4 mm	y_{tube}	$(2n_{tubes}$ - $1)y_{between,tubes}$ + $2n_{tubes}D_{out})$
$y_{between,tubes}$	6 mm	y_{cube}	y_{tube} + $2y_{tube,walls}$
$y_{tubes,walls}$	3.3 mm	z_{tube}	$n_{passes}D_{out}$ + $(n_{passes}$ - $1)z_{between,tubes}$
$z_{between,tubes}$	16 mm	z_{PCM}	z_{tubes} + $2z_{tubes,walls}$
$z_{tubes,walls}$	2 mm	z_{cube}	$\frac{\rho_s}{\rho_l} z_{PCM}$

The values that are decided to be independent variables are N_{passes}, N_{tubes}, and L_{tube}. In combination with the constant values, all the dimensional parameters can be determined because they have a clear relation to each other. The relations between the dimensions as a function of the constants and the independent variables are shown in Table 3.1. The relation between the length and width of the enclosure (x_{cube}, y_{cube}) is defined as the scaling factor S. The value of S is $\frac{5}{3}$ for the commercially available heat battery.

The scale of the system is expressed in the discharging power and the mass of PCM used to store the energy. The mass of the PCM is determined by the dimensions, which are defined through the independent variables. So by delivering an input in the form of one of the independent variables, the scale of the system can be expressed in the mass of the PCM. To provide the model with a single input, the independent variables can be expressed in each other through the relations from Equations 3.11 & 3.12. Finally, the mass of the PCM is expressed by $m = [x_{cube}y_{cube}z_{cube}]\rho_s$.

$$L_{tube} = x_{tube} \qquad (3.11) \qquad n_{tubes} = int[0.3n_{passes} + 0.491] \qquad (3.12)$$

The model will give the power output, the distributions, and the time of charging/discharging. For different scales and power demands.

3.2.3. Optimization configurations

The final step of the methodology is to find the optimal design of the heat battery. When the model is validated and able to supply the desired power demand, the model should be optimised to decrease the mass of the PCM. This is done by inserting the aluminium sheets in the material to enhance the thermal conductivity of the PCM. In the commercially available design, a total of 58 aluminium plates are inserted in the material, so this should also be implemented in the model. Another optimisation is to shorten the length of the heat transfer path within the PCM (dy). Doing this will decrease the melting time and make the design more compact, thus decreasing the mass of PCM utilised.

Now, the optimised design can be approached in three ways and expressed in three independent variables, namely the number of tubes, the number of passes, and the length of a single pass. These parameters are inherently linked with„ respectively x_{cube}, y_{cube} and $zcube$. Through this, three configurations are defined where one of the three independent variables is dominant. The configurations depend on the scaling factor S, which defines the relation between the dimensions of the enclosure. An overview of the three configurations is given in Figure 3.6.

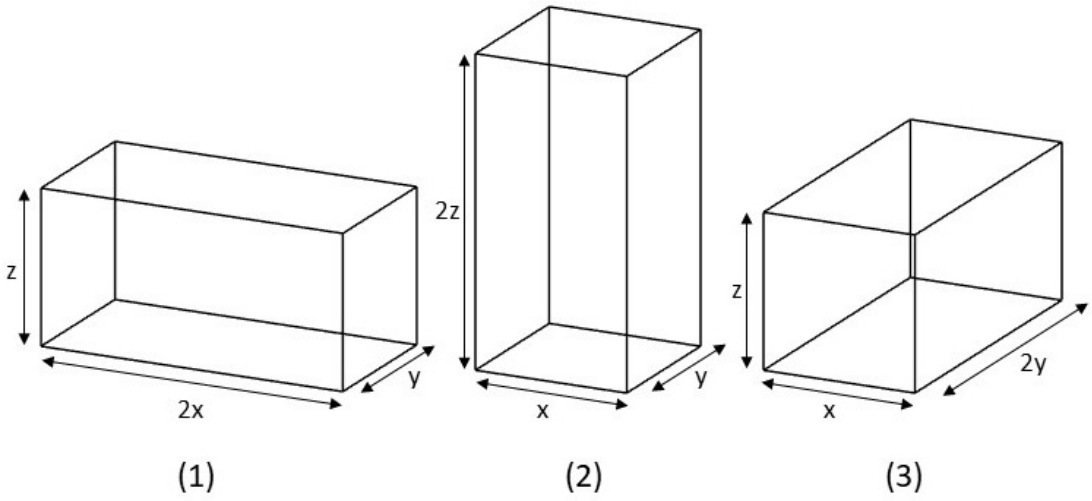

Figure 3.6: Overview of the configurations used for optimization.

1. $x_{cube} = 2y_{cube} = 2z_{cube}$

   Here, x_{cube} is twice as wide as the other dimensions. The variable which will be enhanced is the length per pass, meaning the total length of the tubes within the PCM is large and thus increases the surface area. Due to the large length of the tubes, $\frac{dT}{dx}$ is over a longer length, thus increasing the temperature difference over the HTF.

2. $z_{cube} = 2x_{cube} = 2y_{cube}$

   Here, z_{cube} is twice as long as the other dimensions, thus enhancing the number of passes that will fit the design. More passes will result in an increase in the total length of the tubes within the PCM. This will also increase the surface area and the temperature difference over the HTF. The design of configuration 2 has the most resemblance to the commercially available heat battery.

3. $y_{cube} = 2x_{cube} = 2z_{cube}$

   In the third design y_{cube} is twice as large as the other dimensions. This configuration shows an increase in the number of parallel tubes in the design. This leads to a shorter total length per tube, but will increase the amount of section in which the PCM is divided and decreases the distance between tubes, as described in Figure 3.3. This will increase the charging time but decreases the temperature difference over the HTF.

The three configurations will be compared on certain outputs. Namely, the effect on the outlet temperature; the charging or discharging power depending on the sequence; the melting/solidifying distribution of the PCM; and finally the average effectiveness of the system. The constraints of the optimisation are the mass of PCM used, the mass flow rates for heat transfer modes being equal, and the power output being at least 8 kW.

Heat exchange effectiveness describes the performance of a heat exchanger. It can be argued that a PCM thermal energy storage device is a heat exchanger with thermal performance defined by a fixed heat source/sink at the PCM temperature. During the phase change period, the actual energy stored and released is defined by this effectiveness, which directly affects the useful energy stored [40]. The effectiveness is described as a ratio of the actual heat discharged to the theoretical maximum heat that can be discharged, as seen in Equation 3.13. The maximum effectiveness of the system arises when the outlet temperature of the HTF is the same as the phase-change temperature. The process is a transient process and therefore the effectiveness of the heat exchanger is bounded between 0 and 100 % [38].

$$\varepsilon = (T_{\text{fi}} - T_{\text{fo}}) / (T_{\text{fi}} - T_{pcm}) \quad (3.13) \qquad \varepsilon = 1 - \exp(-U/(\dot{m}C_p)) \quad (3.14)$$

$$\bar{\varepsilon} = \left(\int_{\chi=0}^{\chi=1} \varepsilon d\chi \right) / (1-0) \quad (3.15) \qquad \bar{\varepsilon} = \int_0^1 (1 - \exp(-U/(\dot{m}C_p A_{PCM}))\, d\chi \quad (3.16)$$

For the heat battery, the effectiveness over the phase change is the most interesting parameter on which to test the configurations. Therefore, the average effectiveness over the sensible charging or discharging system is not taken into account. By assuming this, we can describe the effectiveness of the system by Equation 3.14. This equation represents instantaneous effectiveness at any point in time during the phase change period, while Equation 3.15 shows that average effectiveness during the phase change period. These two equations can be combined to the final equation 3.16.

3.3. Hypothesis

Based on the methodology described, a hypothesis is formulated consisting of the following three statements.

- The optimization configurations will perform better than the commercially available heat battery in terms of heat transfer, charging time and power output. The size of the system and the corresponding mass of PCM will be reduced as a result of the optimisation of the heat exchanger specifications.
- The discharge time will be shorter than the charging time for all configurations [24]; furthermore, the discharge power will outperform the charging power. In the case of simultaneously charging and discharging, in an initially molten state, these powers will converge after the PCM is completely solidified. When the final values for the charging and discharging power are reached, the system is in steady state, so it is independent of time.
- The first and second configurations will produce a higher temperature difference over the HTF as a result of the extended length of individual tubes. On the other hand, configuration 3 will have better heat transfer characteristics due to the PCM being divided into more rectangular sections, thus reducing the amount of PCM being melted by an individual tube. This will most likely result in more stored and retrieved heat in and out of the material and shorter charge and discharge time periods.

4

Numerical Analysis

In this chapter, an analysis is carried out to evaluate the proposed methodology. First, the goal of this numerical analysis is described in Section 4.1. Thereafter, in Section 4.2, the approach is described, which elaborates on the different scenarios and assumptions in the model. Furthermore, a method and the procedure of implementing the method are given in this section. The results of the analysis are given in Section 4.3, where the results are then discussed in Section 4.4. Finally, in Section 4.5 the conclusion of this analysis is formulated.

4.1. Goal

The numerical model for the latent heat storage unit is based on the findings of Morrison [28]. The methodology proposes the assumptions, which enables us to use the model for the commercially available heat battery. The model simulates a hot and a cold circuit running through a PCM with one-dimensional heat transfer. The HTF flows through copper pipes of a fixed diameter, where the flow is divided into a number of tubes and a number of passes. The PCM is divided into rectangular slabs with a width equal to the distance between the parallel tubes. This model is used to design a thermal battery based on the commercially available heat battery. The emphasis of the model is to design a model for different scales and power demands. Therefore, the numerical analysis is defined in two parts. Firstly a numerical model is produced which simulates the commercially available heat battery specifications and outputs, secondly a smaller laboratory-size scale of the system has to be simulated and is used as the bases for the design for the experimental set-up. The entire analysis is based on numerical simulations. The goal of this analysis is to find answers to the following questions:

- What is the distribution of the PCM temperature, when scaling the system?
- What is the temperature difference over the heat transfer fluid, when scaling the system?
- What is power stored in or retrieved from the heat battery, when scaling the system?
- What is the average effectiveness of the heat battery, when scaling the system?

4.2. Approach

To approach the goal of simulating the heat battery for different sizes. There are three modes of heat transfer within the system, which have to be simulated separately. Therefore, the three scenarios that are considered are : charging the system, discharging the system, and simultaneously charging and discharging the system. A brief explanation of the scenarios mentioned below is given below.

4.2.1. Scenarios

In this section, system considerations for each mode of heat transfer are discussed.

(1) Charging the system

For charging the system the initial temperature of the PCM is the reference temperature T_{ref}, the liquid fraction is zero ($\chi = 0$), and the flowrate is yet to be determined. The flow rate depends on the

number of parallel tubes, where, by mass conversion, the flow through each tube is equal to the total mass flow of the hot circuit divided by the number of parallel tubes.

One consideration while charging the system is that of the parallel tubes in the system, only half of them are used for charging the model; the other two tubes containing the cold flow are stationary while charging, thus having no effect on the system. This means that the length of heat transfer in the PCM is the distance between the hot circuits, which is depicted in Figure 3.5a. from the previous chapter.

A turbulent flow shows considerably better heat transfer; therefore, one of the conditions of the system is that the Reynolds number should be greater than 10,000 [41]. This is a constraint that determines the flowrate when the system is charged. The Reynolds number will determine the thermal resistance of the HTF within the thermal network. When the system is charged, the conductive resistance of the solid PCM will dominate the thermal resistance, because $R_{PCM} > R_{HTF} > R_{wall}$. When melting occurs, the conductive resistance grows linearly for the liquid interface and decreases linearly for the solid interface. Note that the average effectiveness of the system while charging is only determined over the period of phase change.

(2) Discharging the system
For discharging the system, the initial PCM temperature is the melting temperature (T^*), the liquid fraction ($\chi = 1$), and the flow rate is determined by the number of tubes containing the discharging fluid and a turbulent flow. Similarly to the charging mode, only half of the parallel tubes are used for discharging, while the other half of the tubes containing the "hot" flow are stationary. This means that the length of the PCM where solidification occurs and energy can be extracted is the distance between the tubes with the cold circuit. This is depicted in Figure 3.5b.(b) from the previous chapter.

As heat is extracted from the system, solidification begins at the walls, where the heat is transferred through the layers of solid to the tubes that contain the heat transfer fluid. Therefore, the conductive resistance of the solid PCM increases linearly while solidification occurs, while the conductive resistance for the liquid interface decreases. The average effectiveness of the system during discharging is also determined only during the phase change period.

(3) Simultaneous charging and discharging the system
For simultaneously charging and discharging the system the initial temperature of the PCM is either the reference temperature T_{ref}, with the liquid fraction is zero ($\chi = 0$) for analyzing the mode in solid state. The other option is to analyse the mode of molten state, where the PCM temperature is T^* and the liquid fraction is one ($\chi = 1$). The flow rate depends on the Reynolds number to ensure turbulent flow. The flow rates are equal to each other or unequal, which has an effect on the temperature difference in the heat transfer fluid. However, the flow rate has no effect on the distribution of the PCM temperature.

When the system is charging and discharging, all the parallel tubes are transferring heat, so there are no stationary tubes. The length of heat transfer in the PCM is the distance between the charging and the cold circuit, which is depicted in Figure 3.5c from the previous chapter.

The phase change will occur at a lower rate because both flows enhance each other's effect. This shows a lower melting rate when analysing the initial solid state of the system, and a lower solidification rate when analysing the initial molten state of the system. The discharging power will be higher and constant over a longer period of time due to the charging of the system at the same time.

4.2.2. Method

To provide a realistic simulation for the heat battery, certain assumptions are made, which are previously mentioned in Chapter 3. With these assumptions in mind, the method of the model can be approached. where the main parameters of this framework are the input, constants, and outputs. It is key to determine which inputs are given to the model to generate the desired outcomes. For structuring the model, the assumptions are presented in an overview in this section. When necessary, a brief explanation is given with the assumption.

- The model does not require tracking of the phase interface.
- The phase transition must be accompanied by a high latent effect:
  For the model the salt hydrate HS48 is used. which acquires a latent heat of fusion of 225 kJ/kg.
- The model does not take into account degradation after a large number of reversible cycles.

- During flow axial conduction is negligible :
  This gives in terms of the heat equation : $k\frac{d^2T_f}{dx^2} = 0$
- Temperature gradients normal to the flow can be neglected :
  Due to a low Biot number, it is assumed that $\frac{dT}{dy} = 0$ [22].
- Heat losses to the surrounding are zero.
- The model only takes into account the ideal reversible phase change :
  In other words, this means that no supercooling or phase separation occurs.
- There is only conductive heat transfer within the PCM :
  The convection heat transfer is negligible,thus ignoring the Rayleigh-Bénard convection [42].
- The range of the melting temperature of the PCM is between 49 °C and 51 °C :
  This is due to the enthaly hysteresis of the properties of the HS48 PCM.
- All heat is absorbed as latent heat while in phase change:
  No more sensible heat is added to the PCM, when the temperature is equal to T^*.
- Horizontally uniform melting distribution:
  The liquid fraction over time is a linear function.
- The temperature is uniform throughout the mass of the phase-change material.
- The material between the tube passes is ignored to determine the thermal resistance:
  Because heat transfer between two passes of the same tube is negligible.
- Axial conduction through the PCM is negligible :
  Thermal conductivity of PCM is small enough, so $\frac{du}{dx} = 0$
- Heat transfer between two passes of the same tube is negligible.
- One-dimensional heat transfer in the y-direction.
- The average effectiveness over the sensible charging or discharging of the system is negligible :
  $\bar{\epsilon}$ is only determined over the phase change period.

With the assumptions and equations of Section 3.1 and 3.2, the model can be generated. For the model, the input, constant parameters and output need to be determined first.

Input
The input for the laboratory scale system is the basis of the design of the experimental setup, which is described in Appendix A. An overview of the inputs for both systems which apply to all scenarios is given in Table 4.1. The numerical analysis will focus on equal flow rates for the third scenario.

Table 4.1: Input for the latent heat storage system.

Property	Value	Unit
m_{PCM}	110	kg
$(x, y, z)_{cube}$	(500, 300, 700)	mm
L_{tube}	483	mm
N_{tubes}	20	
N_{passes}	32	
N_{plates}	58	
A_{PCM}	0.346	m^2
A_f	0.223	m^2
$\dot{m}_{charge}$	25	$\frac{kg}{min}$
$\dot{m}_{discharge}$	14	$\frac{kg}{min}$
$\dot{m}_{sim,equal}$	10	$\frac{kg}{min}$

(a) Input for the commercially available heat battery

Property	Value	Unit
m_{PCM}	5.5	kg
$(x, y, z)_{cube}$	(180, 108, 252)	mm
L_{tube}	163	mm
N_{tubes}	4	
N_{passes}	12	
N_{plates}	20	
A_{PCM}	0.045	m^2
A_f	0.031	m^2
$\dot{m}_{charge}$	3	$\frac{kg}{min}$
$\dot{m}_{discharge}$	3	$\frac{kg}{min}$
$\dot{m}_{sim,equal}$	3	$\frac{kg}{min}$

(b) Input for the laboratory-size heat battery.

Constant parameters
The parameters that are constant for both sizes of the model are given in Table 4.2. Here, the wetted perimeter is calculated by $P = 2\pi R_{in}$, and the flow area for determining the Reynolds number by $A_{tube} = \pi R_{in}^2$.

Table 4.2: Constant parameters of the latent heat storage system.

Property	Value	Unit
T^*	50	°C
T_{max}	75	°C
T_{ref}	20	°C
$T_{fi,charge}$	70	°C
$T_{fi,discharge}$	12	°C
ρ_s	1400	kg/m^3
ρ_l	1380	kg/m^3
k_s	0.60	$W/(mK)$
k_l	0.46	$W/(mK)$
C_l	3470	$J/(kgK)$
C_s	3100	$J/(kgK)$
λ	225	kJ/kg
k_{copper}	398	$W/(mK)$
$k_{aluminium}$	237	$W/(mK)$
k_{water}	0.65	$W/(mK)$
μ_{water}	4.04 10^{-5}	Pa/s
ρ_{water}	1000	kg/m^3
$C_{p,water}$	4200	$J/(kgK)$
P	13.8	mm
L_{plate}	0.5	mm
A_{tube}	15.21	mm^2

Output
With the parameters and inputs inserted into the model and the theory from Chapter 3, the desired output of the system can be calculated. An overview of the results is given in Table 4.3. Note that the outputs are time-dependent, while some outputs are taken as the total or average value over the time range.

Table 4.3: Output of the latent heat storage system.

Output	Comment
T	Temperature of the phase-change material
χ	Liquid fraction of the phase change material
Q_s	Total stored energy
Q_r	Total retrieved energy
$T_{f,o}$	Outlet temperature over the HTF for both flows
ΔT_f	Temperature difference over the HTF for both flows
$\dot{Q}$	Charging or discharging power
$\bar{\epsilon}$	Average effectiveness of the system over the phase-change

4.2.3. Procedure

The model is a numerical model capable of determining the time of charge, discharging, and simultaneous charge or discharging of the system. Therefore, the equations of Chapter 3.1 have to be rewritten in numerical form. To determine the first output, the temperature of the phase-change material, two equations have to be set equal to each other. Taking the derivative of Equation 3.3, the new relation is given in Equation 4.1. Subsequently, it is set equal to the known relation of $\frac{du}{dt}$, which is taken from Equation 3.2. This holds when there are no losses, as established in the assumptions, and the change in internal energy in the material must be equal to the added internal energy to the PCM for a given PCM temperature T. Thus with all known parameters, the model can numerically find the temperature of the PCM per time step, which is shown in Equation 4.2. Note that the overall heat transfer coefficient U^n is also time dependent because it depends on the value of χ^{n-1}, which is initially zero for the charging mode and one for the discharging mode.

$$\frac{\partial u}{\partial t} = \begin{cases} C_s \frac{\partial T}{\partial t} & \text{if } T < T^* \\ \frac{\partial \chi}{\partial t}\lambda & \text{if } T = T^* \\ C_l \frac{\partial T}{\partial t} & \text{if } T > T^* \end{cases} \tag{4.1}$$

$$T^n = \begin{cases} (C_s T^{n-1} + (\frac{U^n P}{\rho_s A_{PCM}})T_{f,i}))/(\frac{U^n P}{\rho_s A_{PCM}} + C_s) & \text{if } T < T^* \\ T_{n-1} & \text{if } T = T^* \\ (C_l T^{n-1} + (\frac{U^n P}{\rho_s A_{PCM}})T_{f,i}))/(\frac{U^n P}{\rho_s A_{PCM}} + C_l) & \text{if } T > T^* \end{cases} \tag{4.2}$$

The temperature of the PCM is now determined for every time step. The liquid fraction is also a function of the PCM temperature and the inlet temperature of the HTF, because both know the liquid fraction can be determined by Equation 4.3. The equation is basically a rewritten form of Equation 3.3, but where the liquid fraction is assumed to be zero below melting temperature, and 1 above the melting temperature. The sensible and latent heat stored per second in the phase change material is defined by Equation 4.4. To derive the total stored energy the values per time step should be added.

$$\chi^n = \begin{cases} 0 & \text{if } T < T^* \\ (\frac{U^n P}{\rho A_{PCM}} \frac{T_{f,i} - T^n}{\lambda}) + \chi^{n-1} & \text{if } T = T^* \\ 1 & \text{if } T > T^* \end{cases} \tag{4.3}$$

$$Q_s^n = \begin{cases} mC_s(T^n - T^{n-1}) & \text{if } T < T^* \\ m(\chi^n - \chi^{n-1})\lambda & \text{if } T = T^* \\ mC_l(T^n - T^{n-1}) & \text{if } T > T^* \end{cases} \tag{4.4}$$

With these numerical solutions, the outlet temperature of the heat transfer fluid is determined using Equation 3.4. After some rewriting and setting the boundary conditions $T_f(x = 0) = T_{f,in}$ and $T_f(x = L) = T_{f,o}$. The results are shown in Equation 4.5. The temperature difference over the heat transfer fluid is determined by $\Delta T_f = T_{f,i} - T_{f,o}$. With the temperature difference over the heat transfer fluid, the power of charging or discharging is determined using Equation 3.5. Average effectiveness is the final output of the model and is calculated using Equation 4.7. Here, average effectiveness is not taken into account when adding or retrieving sensible heat from the phase-change material.

$$T_{f,o}^n = \frac{T^n - (T^n - T_{f,i})}{\exp\left\{(\frac{UP}{(\dot{m}C_p)_f} L_{tube})\right\}} \tag{4.5}$$

$$\dot{Q}^n = \dot{m} C_{p,water}(T_{f,0}^n - T_{f,i}) \tag{4.6}$$

$$\bar{\varepsilon} = \begin{cases} 0 & \text{if } T < T^* \\ \int_{t(\chi=0)}^{t(\chi=1)} \left(1 - \exp\left(-U^n / \left(\dot{m} C_p A_{PCM}\right)\right) dt & \text{if } T = T^* \\ 0 & \text{if } T > T^* \end{cases} \tag{4.7}$$

With these equations in numerical form and the other parameters from this approach, the results are generated for both the commercially available heat battery and the laboratory-size heat battery. The results are discussed in the following section.

4.3. Results

The results are given for all three scenario's of the simulation. The model produces the outputs given in Table 4.3 for every time step in the specific mode. The results are discussed in Section 4.4.

4.3.1. Scenario 1 : Charging the system

The initial conditions for the charging sequence are : $T(t = 0) = T_{ref}$, χ(t=0) = 0.

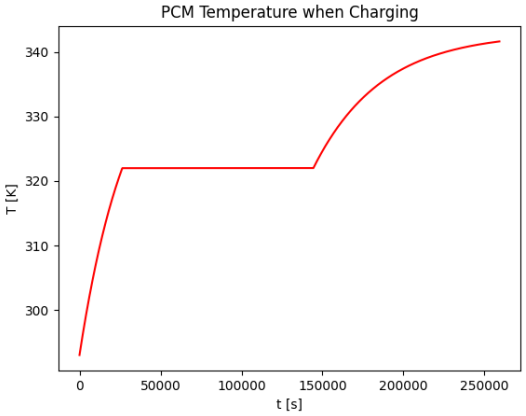

(a) PCM temperature distribution for the commercially available heat battery.

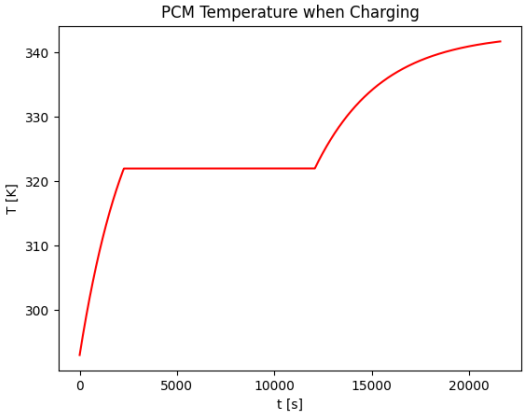

(b) PCM temperature distribution for the laboratory-size scale.

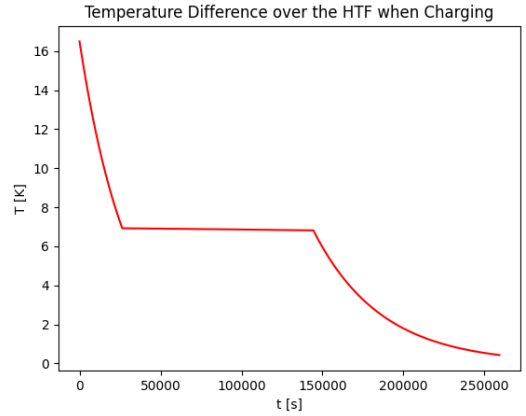

(c) Temperature difference over the HTF the commercially available heat battery.

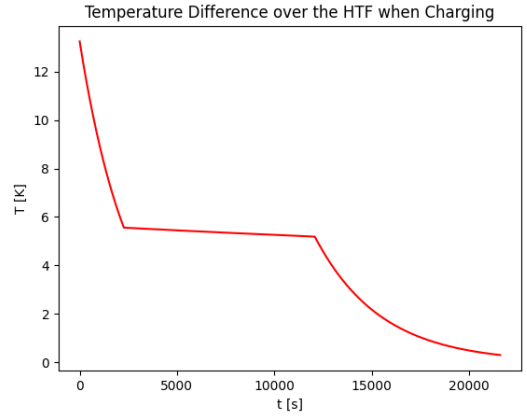

(d) Temperature difference over the HTF for the laboratory-size scale.

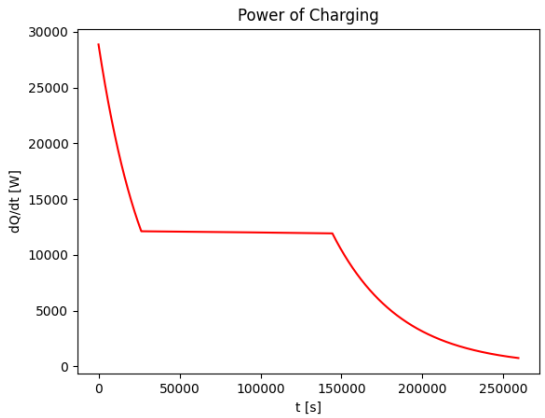

(e) Power of charging for the commercially available heat battery.

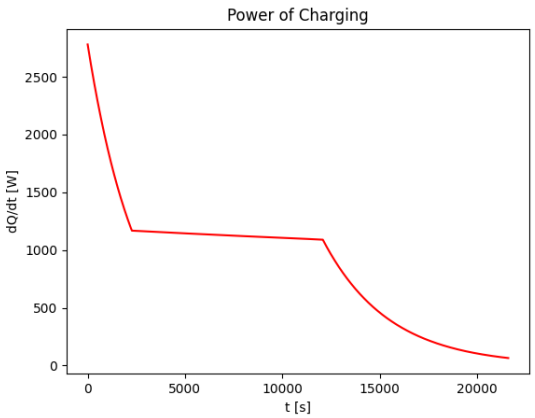

(f) Power of charging for the laboratory-size scale.

Figure 4.1: Results of the analysis for both sizes of the system for Scenario 1.

4.3.2. Scenario 2 : Discharging the system

The initial conditions for the charging sequence are : $T(t = 0) = T_{max}$, χ(t=0) = 1.

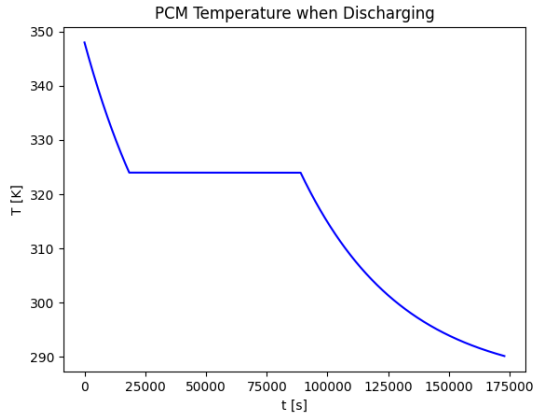

(a) PCM temperature distribution for the commercially available heat battery.

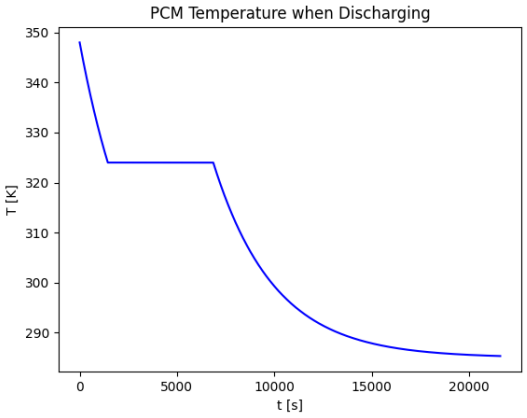

(b) PCM temperature distribution for the laboratory-size scale.

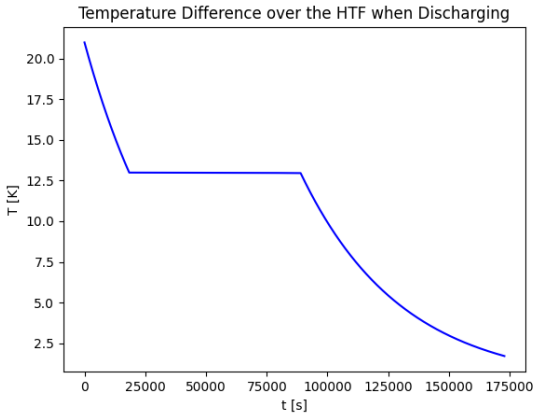

(c) Temperature difference over the HTF for the commercially available heat battery.

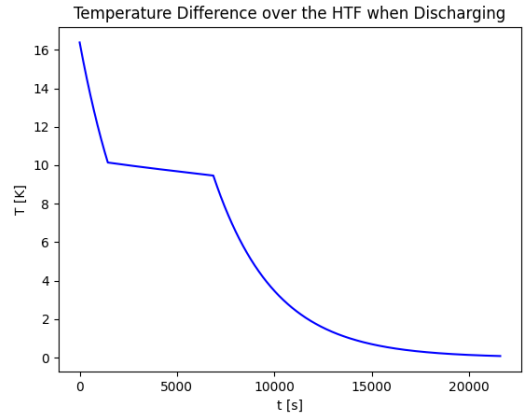

(d) Temperature difference over the HTF for laboratory-size scale.

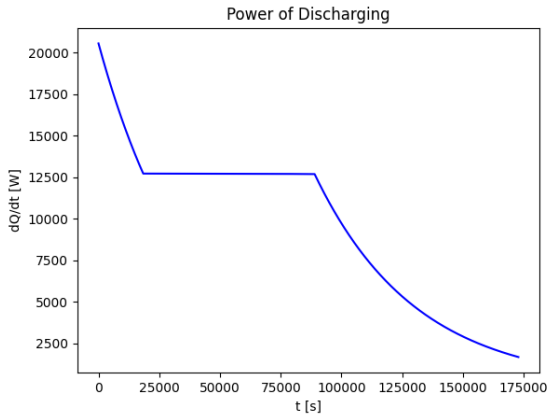

(e) Power of discharging for the commercially available heat battery.

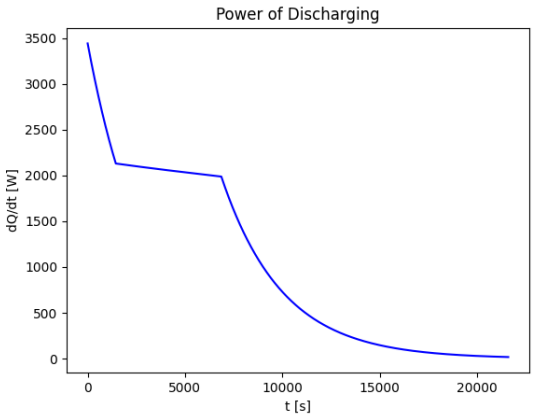

(f) Power of discharging for the laboratory-size scale.

Figure 4.2: Results of the analysis for both sizes of the system for Scenario 2.

4.3.3. Scenario 3 : Simultaneously charging and discharging the system

The initial conditions for the charging sequence are : $T(t = 0) = T_{max}$, χ(t=0) = 1.

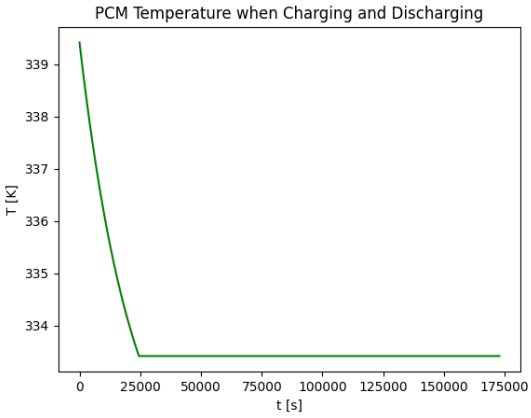

(a) PCM temperature distribution for the commercially available heat battery.

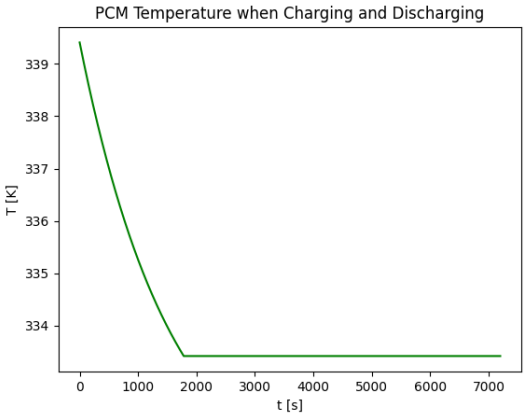

(b) PCM temperature distribution for the laboratory-size scale.

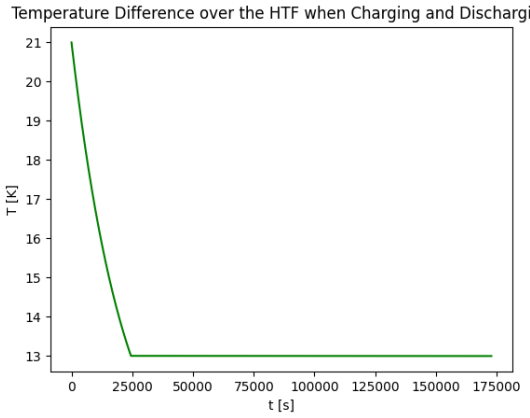

(c) Temperature difference over the HTF for the commercially available heat battery.

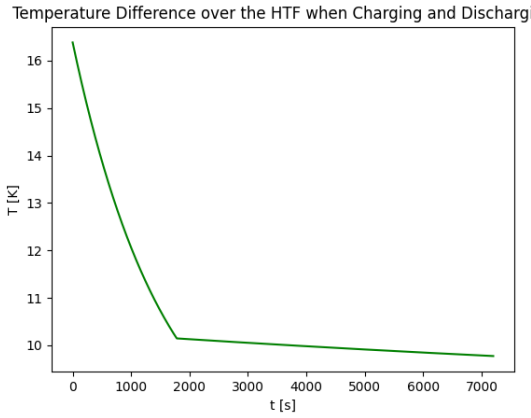

(d) Temperature difference over the HTF for laboratory-size scale.

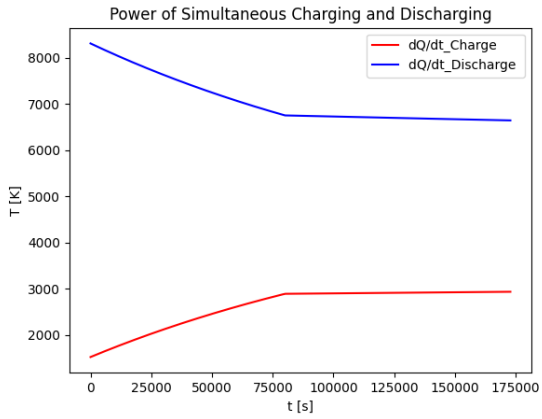

(e) Power of charging and discharging for the commercially available heat battery.

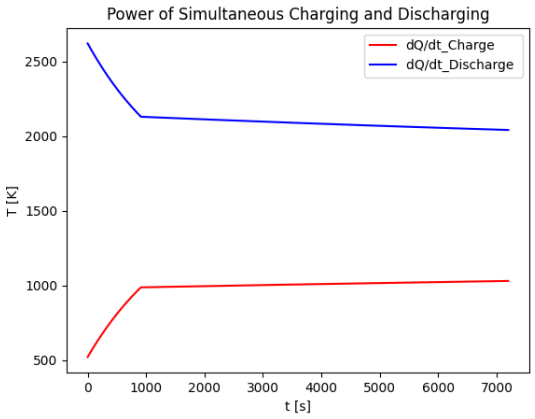

(f) Power of charging and discharging for laboratory-size scale.

Figure 4.3: Results of the analysis for both sizes of the system for Scenario 3.

4.4. Discussion

Scenario 1

The temperature of the PCM follows the same trend for both sizes. First, sensible heat is added when the temperature is rapidly increasing. This is due to the thermal resistance of the PCM being only the thermal conductivity of the solid phase, where $k_s < k_l$. As the temperature increases, a small decline in slope is seen. At the melting temperature, the PCM is absorbing all heat as latent heat; for both cases, it is seen that the temperature stays constant for a longer period. Once melting is complete, the PCM temperature starts to rise eventually, while a decline in the temperature rise is also observed until eventually the maximum temperature is achieved. The biggest difference between the two models is the charging time. The charging time for the commercially available battery is approximately 72 hours, where the melting temperature is reached after 10 hours and the PCM is fully melted after 42 hours. However, the charging time for the laboratory-size heat battery is 6 hours, where the melting temperature is reached after 1 hour, and the PCM is fully melted after 3.5 hours. This shows that the melting time is increasing exponentially for an increasing mass of PCM.

The temperature difference between the heat transfer fluid and the PCM is greatest when the PCM temperature is at the reference temperature. This is due to the large temperature difference between the inlet temperature of the HTF and the PCM temperature. The commercially available heat battery achieves a higher temperature difference on the HTF than on the laboratory size scale. This is due to the longer path for the fluid, which is related to the larger number of passes and length of the tube. The temperature difference shows a very small decrease while the material is melting. The charging power is a function of the temperature difference and the mass flow rate as shown in Equation 4.2.3. Therefore, it has the same slope for both sizes.

Note that the charging power of the commercially available heat battery is around 12 kW for the phase change with a maximum value greater than 25 kW when heating up the solid PCM. The laboratory size requires a maximum power of greater than 2.5 kW and charges the PCM with approximately 1 kW while undergoing phase change. The average effectiveness of charging and the total stored heat are shown in Table 4.4, note that the total stored heat is larger in the first size; however, this amount of mass is capable of storing 41.62 MJ of sensible and latent heat, while the laboratory size is capable of storing a maximum of 2.13 MJ.

Table 4.4: Average effectiveness of charging and total stored energy for both sizes of the system.

Output	Value
$Q_{s,Heatbattery}$ $[MJ]$	40.05
$Q_{s,Laboratory}$ $[MJ]$	2.09
$\bar{\epsilon}_{Heatbattery}$ [%]	7.4
$\bar{\epsilon}_{Laboratory}$ [%]	24.7

Scenario 2

For discharging the system, the time is the same as for the charging system. Here, the commercially available heat battery takes approximately 48 hours of discharging to cool the system to the reference temperature. This shows that the latent heat storage system is capable of providing heat for 2 days. The laboratory-sized heat battery takes around 6 hours to cool the phase change material to the same temperature as the inlet of the cold circuit, where $T_{f,i} = 285\ K$. In both cases, the temperature starts to decrease rapidly when sensible heat is retrieved from the liquid phase-change material. Subsequently, the melting temperature remains constant while the material is solidifying. Finally, the temperature achieves the reference temperature, or in the laboratory case, the inlet HTF temperature, where the slope of decreasing temperature decreases more as the temperature lowers.

The temperature difference when discharging is an important output because it will determine whether the heat battery is capable of providing domestic hot water. In this case, the outlet temperature will be around 305 K, which will not provide the standard of hot water. Therefore, a heat pump configuration or optimisation is necessary. For laboratory size, the maximum temperature difference is around 16 K. The temperature difference starts and declines rapidly while the sensible heat is recovered. The temperature difference shows a very small decrease while the material is solidifying,

and then begins to decrease again when the heat is removed from the solid PCM, before achieving a temperature difference of 2 K for the heat battery and zero for the laboratory-sized system. The discharge power follows exactly the same trend as the temperature difference, as expected. The charging power can also be expressed as the power supply of the system. For the commercially available battery, the power supply is 8 kW. Here, the system shows a maximum output of 20 kW, and 12.5 kW when solidifying. This shows a higher value than the required 8 kW. For the laboratory-sized battery, the maximum discharging power is 3.5 kW and 2 kW during phase change. The average effectiveness of discharging and the total heat retrieved from the battery are shown in Table 4.5. The maximum retrieved heat is higher than the stored heat. This is because the PCM temperature has an initial value higher than the final charge temperature, and the final temperature after discharging drops to the HTF inlet temperature, which is lower than the PCM reference temperature.

Table 4.5: Average effectiveness of discharging and total retrieved energy for both sizes of the system.

Output	Value
$Q_{r,Heatbattery}$ $[MJ]$	44.36
$Q_{r,Laboratory}$ $[MJ]$	2.22
$\bar{\epsilon}_{Heatbattery}$ [%]	13.8
$\bar{\epsilon}_{Laboratory}$ [%]	24.3

Scenario 3

The PCM is initially in the molten state and the initial temperature is 340 k. For both sizes, the flowrates of the hot circuit and cold circuit are equal to each other. The commercially available heat battery is simultaneously charging and discharging for a period of 48 hours, while the laboratory-scale battery is running for 2 hours. The temperature of the PCM is decreasing as a result of the discharging power being higher than the charging power; the temperature of the PCM drops to the melting temperature and stays in the phase-change region for the rest of the period. The temperature of the PCM in the smaller size model is showing similar results.

The temperature difference over the HTF is only shown for the cold circuit, because this is the output on which the system will be assessed. The temperature difference for the commercially available heat battery has a maximum of 21 K and remains constant at 13 K during the phase change. For the laboratory-size heat battery, the maximum temperature difference is 16.5 K, while during phase-change the temperature difference is around 10 K. The power to charge while in simultaneous mode is lower than that to charge. The charging power increases, while the PCM temperature decreases. The discharging power decreases when the PCM temperature is decreasing. The power and discharging power are converging while in phase change and will eventually be equal to each other. The maximum discharging power is 8 kW for the first scale and 2.5 kW for the latter scale. The maximum power output during phase change is approximately 8 kW for the commercially available heat battery, which allows the power output requirement determined for this system. For the laboratory-size battery, the power output during the phase change is approximately 2 kW. The average effectiveness for charging and discharging and the total retrieved energy are shown in Table 4.6. Note that the total stored energy is not mentioned because there is no energy being stored while charging, but immediately being retrieved by the cold circuit.

Table 4.6: Average effectiveness of charging and discharging and total retrieved energy for both sizes of the system.

Output	Value
$Q_{r,Heatbattery}$ $[MJ]$	15.48
$Q_{r,Laboratory}$ $[MJ]$	1.13
$\bar{\epsilon}_{Heatbattery,charge}$ [%]	21.8
$\bar{\epsilon}_{Heatbattery,discharge}$ [%]	24.7
$\bar{\epsilon}_{Laboratory,charge}$ [%]	25.6
$\bar{\epsilon}_{Laboratory,discharge}$ [%]	25.1

4.5. Conclusion

In this chapter, a numerical analysis is conducted to evaluate the proposed methodology. The basis of the analysis is to determine whether the commercially available heat battery can be simulated and whether the system can be scaled down to be the basis of the design for experimental validation. Therefore, the numerical analysis is defined in two parts. Firstly, a numerical model is produced which simulates the commercially available heat battery specifications and outputs, and secondly a smaller laboratory-size scale of the system has to be simulated and is used as the bases for the design for the experimental set-up. The entire analysis is based on numerical simulations. From the results, the research questions from Section 4.1 are answered.

What is the distribution of the PCM temperature, when scaling the system?

The results of the temperature distribution show that the charging time is growing non-linearly with an increase in the mass of PCM. The same is observed in the discharge mode, where the discharge time is significantly shorter than the charging time as predicted in Section 3.3. For the simultaneously charging and discharging mode, the temperature remains constant at the melting temperature. This implies that the material is still solidifying, which is also mentioned in the hypothesis.

What is the temperature difference in the heat transfer fluid, when scaling the system?

The temperature difference is larger for charging and discharging on a larger scale, this is due to the increased number of passes and length per tube. This will result in a longer heat transfer path for the HTF to be heated up. The laboratory scale also produces a large temperature difference for these two modes; this is most likely due to the low mass flow rate of the water that runs through the system. For simultaneously charging and discharging, similar results are shown, where the temperature difference remains constant for a longer period, which is seen as a positive effect.

What is power stored in or retrieved from the heat battery, when scaling the system?

The power added is a function of the temperature difference, thus showing the same trends as the temperature differences of the various heat transfer modes. The discharging power of the Heat battery shows significantly higher maximum values than explained in the data, namely 12.5 kW, where 8 kW is expected.

What is the average effectiveness of the heat battery, when scaling the system?

The average effectiveness is low for the commercially available heat battery; this mostly shows that optimisation is needed for this system. It is noticeable that when the system is scaled down, the average effectiveness will increase significantly. This implies that the average effectiveness of the system is affected by the size of the system.

In conclusion, the numerical analysis produces a model which is able to design a thermal battery based on the commercially available heat battery. Additionally, the model can design a model for different scales and power demands, and produce realistic outputs.

5

Experimental validation

This chapter discusses the applied experimental procedure used to collect accurate experimental data. In Section 5.1 the specifications of the latent heat storage system designed for experiments are described. Thereafter, the experimental set-up and the corresponding components are described in Section 5.2. In Section 5.3, applied data analysis and calculation of system output is described. The results of the measured data are shown and discussed in Section 5.4. Finally, a summary of the experimental validation is described in Section 5.5.

5.1. Specifications

In the previous chapter, a numerical analysis as carried out. In that study, two different scales are worked out on which the system is simulated. The second size is a laboratory-scale size of the commercially available heat battery. To conclude about the accuracy of this simulation, the methodology developed is applied in an experimental setting to validate the outputs of the system. For validation, an experimental test set-up is designed; the process of the design of the experimental set-up is described in Appendix A. Through the measurement devices, the experimental output is determined and then compared with the data from the numerical model. When analysing both the results of the model and the real-life data, the model is experimentally validated and can be used for optimisation.

The properties of the system are scaled by the available phase-change material and the bend radius of the copper tubes. An overview of the specifications of the system is shown in Table 5.1. The mass flow rates are not mentioned because they differ for specific test sequences.

Table 5.1: Specifications of the latent heat battery design.

Dimension	Value	Dimension	Relation
R_{out}	3 mm	R_{in}	R_{out} - d_{wall}
d_{wall}	0.8 mm	x_{cube}	Sy_{cube}
x_{bends}	11 mm	x_{tube}	x_{cube} - $4x_{bends}$ - $2x_{tubes,walls}$
$x_{tubes,walls}$	8 mm	y_{tube}	$(2n_{tubes}$ - $1)y_{between,tubes} + n_{tubes}R_{out}$
$y_{between,tubes}$	25 mm	y_{cube}	$y_{tube} + 2y_{tube,walls}$
$y_{tubes,walls}$	10 mm	z_{tube}	$n_{passes}D_{out} + (n_{passes}$ - $1)z_{between,tubes}$
$z_{between,tubes}$	10 mm	z_{PCM}	$z_{tubes} + 2z_{tubes,walls}$
$z_{tubes,walls}$	15 mm	z_{cube}	$\frac{\rho_s}{\rho_l} z_{PCM}$

5.2. Experimental set-up

An overview of the experimental set-up is provided in Figure 5.3. In this figure, the set-up is shown where the PCM is not loaded, secondly, the PCM is loaded in the system, and the insulation is installed to three sides of the cube. The webcam is also installed, which measures the liquid fraction. The experimental set-up consists of three main components. The first is the designed heat battery. Second, the heat exchanger service unit, which provides the hot and cold circuits and is able to record the data. Third, the temperature probe, which measures the temperature of the phase-change material. For each part, further elaboration is given below, furthermore, the test procedure is described.

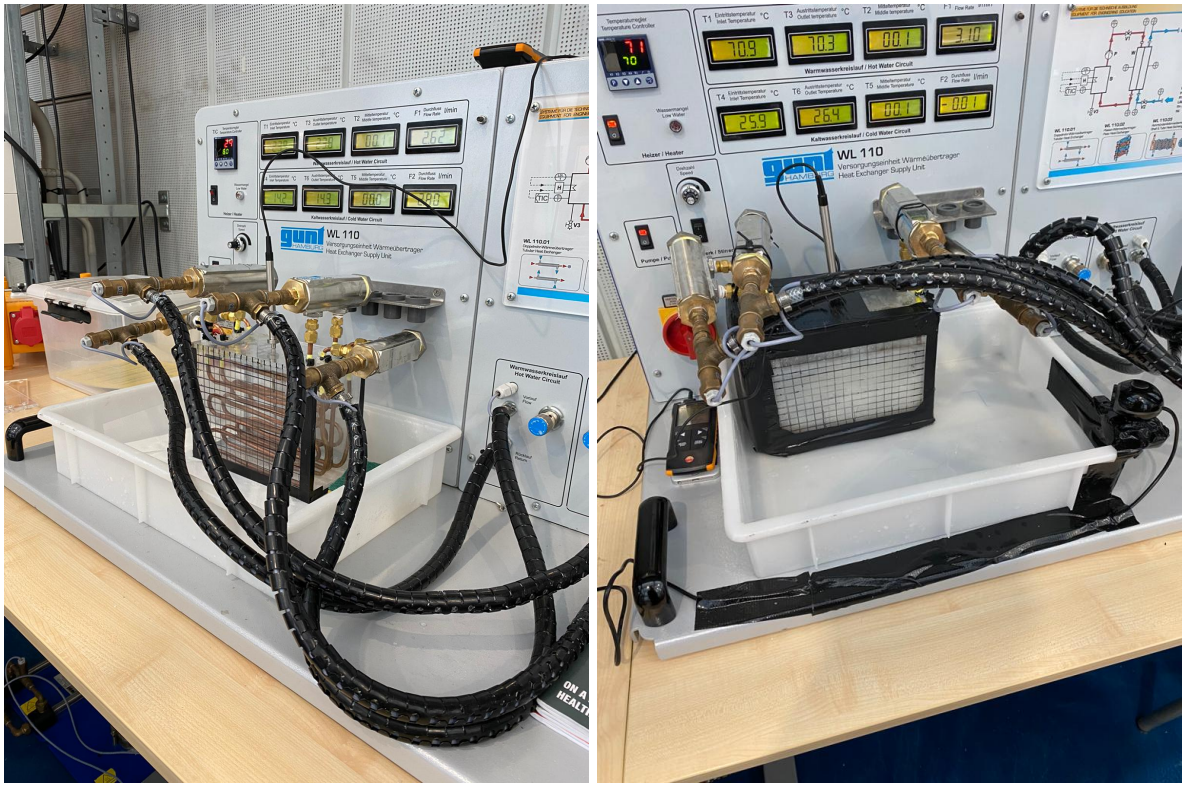

(a) Experimental set-up not containing PCM. **(b)** Experimental set-up loaded with PCM.

Figure 5.1: Overview of the experimental set-up.

5.2.1. Overview of the components

One of the components is the latent heat battery, as shown in Figure 5.2. For the test set-up, 2.8 kg of HS48 PCM is provided by commercially available. Copper brake wiring is used for the tubing. Based on the 2.8 kg provided, a rectangular enclosure is designed in which the tubing is fitted. The rectangular enclosure is made of PMMA, which is a see-through material so that the liquid fraction can be measured. To ensure that there is no supercooling or superheating occurring within the PCM, the design must be airtight. This is because of the vaporised water, within the salt hydrate, which could escape into the air. Salt-hydrate with fewer water particles requires a higher melting temperature.

The dimensions of the tube are constrained by the dimensions of the open dividers. These open dividers split the flows of the hot and cold circuit into two parallel tubes, each. These 4 parallel tubes have 5 passes each. The tubing is installed in a countercurrent design, where each hot circuit is followed by a cold circuit, and these flows run in opposite directions. Finally, the insulation is installed to three sides of the enclosure, to minimise heat losses to the surroundings but still be able to measure the liquid fraction on three planes. The measurement grid is printed on the PMMA to quantify the liquid fraction, which is a percentage of the volume. There are no aluminium plates inserted to improve the thermal conductivity.

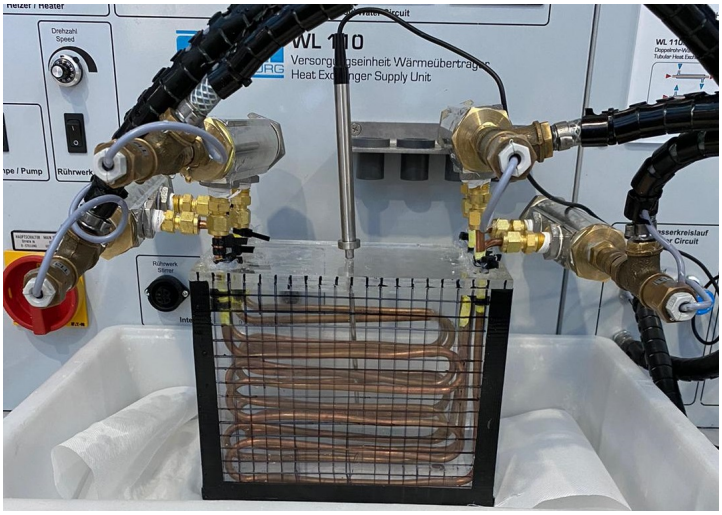

Figure 5.2: Designed heat battery, with the tubing configuration, the open dividers, and the PMMA enclosure.

Another component is the Gunt WL110 HEX service unit, as seen in Figure 5.3a. The service unit has multiple functions. The primary function is to provide the hot and cold circuit to the heat battery, where the flowrate and temperature can be regulated by the system. The technical data corresponding to the system are described in Table 5.2. The system consists of a number of parts. The parts are visualised in Figure 5.3b. where (1) is the temperature controller, (2) is the heated water tank. (3) is the heat exchanger; in this experimental set-up, this is the latent heat battery. (4) is the pump that provides the flowrate, where the red line is the hot water circuit and the blue line is the cold water circuit. the flow sensors are depicted by (F) and the temperature sensors by (T).

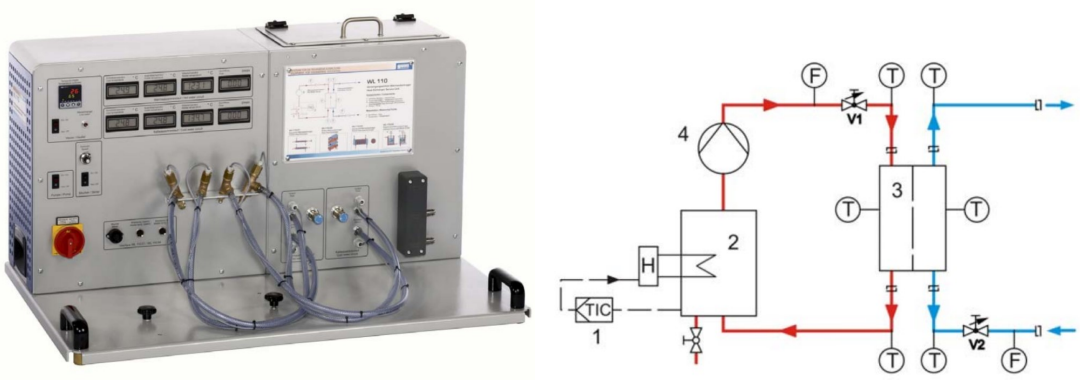

(a) 3D view of Gunt HEX service unit. **(b)** Process schematic of the Gunt HEX service unit.

Figure 5.3: Gunt HEX service unit.

The second function of the HEX service unit is to measure and record the data. Measurements are carried out by the temperature and flow sensors in the building of the system. The software can also record the time. The temperatures of the inlet and outlet flow are sampled in between 1 and 100 s depending on the size of the data set. The discharging test sequence is performed overnight, for logistic reasons, therefore the data-set is large for this test sequence. Data acquisition is carried out by the GUNT software. The software can calculate the charging or discharging power to the system, as well as the heat transfer coefficient and the log-mean temperature difference.

Table 5.2: Technical data of the WL110 HEX service unit [43]

Pump	
Power consumption	120 W
Max. flow rate	600 L/h
Max. head	30 m
Heater	
Power output	3 kW
Water temperature range	0 °C - 70 °C
Volume of water tank	approx. 10 L
Measuring ranges	
Temperature	0 °C - 100 °C
Flow rate	20 L/h - 250 L/h

The final components are the measurement devices. The data which must be measured to determine the power outputs are the PCM temperature and the liquid fraction. For determining the PCM temperature, only one temperature sensor is used. Favourably, multiple sensors are distributed along the PCM to have a more representative value for the temperature along the PCM. Due to the assumption of uniform PCM temperature in Chapter 3 the measured data from the sensor is taken uniformly for the entire phase change material. This is however not realistic; therefore, some alternations are done in the validation of the model in Section 6.1.

The PCM temperature is measured using a temperature probe that is inserted through the top of the enclosure and placed in the middle of the material, as seen in Figure 5.2. For the temperature probe, the TESTO 922 temperature sensor is used. The sampling rate for measuring the PCM temperature during charging and discharging is determined set for every 30 seconds. To measure the liquid fraction, a webcam is used, which films the change in the liquid fraction over time. The liquid fraction is photographed with a sampling rate of 300 s. An overview of the liquid fraction over time is given in Appendix C.

5.2.2. Procedure

To validate the model, the outputs which are defined in the numerical analysis should be determined for the test set-up. There are three sequences which are related to the three scenario's from Section 4.2. The sequences will be carried out with a high mass flow rate and a low mass flow rate, which are 3.0 kg/min and 1.5 kg/min, respectively. The charging and discharging tests are repeated for both mass-flowrates. Simultaneously charging and discharging is conducted with either equal flow rates or unequal flow rates. To ensure the repeatability of the experimental results, a series of test sequences is carried out at least twice under the same operating conditions [44].

In addition, two separate test sequences are conducted to evaluate the heat losses of the system. The air test sequence where no PCM is present and the surface test sequence, where the increase in temperature of the enclosure wall is determined. The air test sequence determines the efficiency of the heat exchanger while in steady state. The hot and cold circuits are both turned on, while the enclosure is filled with air. Due to the air-tight design, the air will be heated due to the hot circuit. After a while, the air temperature, which is measured by the temperature probe, remains constant and steady state is achieved. By subtracting the charging power from the discharging power, the losses per second are determined. When the losses are divided by the charging power, the efficiency of the system is determined when no PCM is available. The surface test sequence follows the same principle; however, now the probe is taped to one of the surfaces of the enclosure and insulated on both sides. The rise of the surface temperature will determine the losses of the system through conductive heat transfer of the non-insulated walls. The surface test sequence is conducted for unequal mass flow rates. An overview of all test sequences is described in Table 5.3. The step-by-step test plan including the loading procedure is described in Appendix B.

Table 5.3: Overview of the test sequences.

Test Sequence	$\dot{m}_{charge}$ $[\frac{kg}{min}]$	$\dot{m}_{discharge}$ $[\frac{kg}{min}]$	Time [h]	Repeats
Air test	3.0	1.5	0.5	3
Surface test	3.0	1.5	0.5	2
Charging test (HFR)	3.0	N.A.	7	2
Charging test (LFR)	1.5	N.A.	7	2
Discharging test (HFR)	N.A.	3.0	13	2
Discharging test (LFR)	N.A.	1.5	13	2
Simultaneous test (Equal)	3.0	3.0	2	2
Simultaneous test (Unequal)	3.0	1.5	2	2

5.3. Uncertainty analysis

Signal processing is done with data from the Gunt software, which measures and converts the data into a CVS file. Average effectiveness, power, and total stored energy are derived from the equations of Section 3.1. Note that some of the experimental data shows large amplitudes of values due to the inlet temperature and mass flow rate fluctuating around the fixed value. The data is smoothed by exponential averaging the data with a damping factor of 0.8 [45]. To test the accuracy of the experimental set-up, an uncertainty analysis has to be conducted.

The uncertainty of the experiment was induced by the heat loss of the thermal energy storage system, the fluctuation of the input temperature and the mass flow rate, and the inaccuracies of the measurement equipment (thermocouples, flow metres, and data acquisition system). Heat loss is determined by the air test sequence and the surface test sequence. The error due to fluctuations is smoothed out by exponential averaging. The measurement error for the mass flow is determined by comparing a calibrated flow metre and a calibrated thermocouple with the flow metre and temperature sensors in the WL110 heat exchanger service unit. The accuracy of the thermocouples is determined by embedding the temperature sensor within a tray of ice, as seen in Figure 5.4. If the thermocouple is fully submerged, but does not touch the melted ice at the bottom of the tray, the temperature sensor should be exactly 0.0 ° C. The offset can be read on the Gunt data logger.

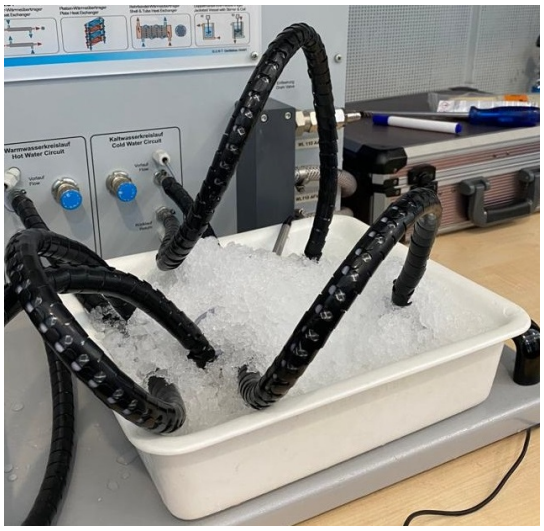

Figure 5.4: Uncertainty analysis of the temperature sensors.

The paddle wheel flow metres inside the Gunt HEX service unit are tested for errors using a precision mass balance scale. Set the flow rate at a certain value and capture the water in the bucket for a specific time period. By dividing the mass of the water inside the bucket by the time period, the mass flow rate can be determined. Make sure the mass flow rate does not fluctuate while performing this procedure.

An overview of all the uncertainties is given in Table 5.4.

Table 5.4: Error of the measurement devices used in experimental set-up.

Measurement device	Error
Thermocouple T4	+ 0.1 °C
Thermocouple T6	+ 0.1 °C
Thermocouple T1	+ 0.1 °C
Thermocouple T3	+ 0.1 °C
Flow metre F1	+/- 2.18 $\frac{g}{s}$
Flow metre F2	+/- 2.12 $\frac{gg}{s}$
Testo Temperature Probe	+ 0.07 °C

The aim is to determine the uncertainty in the calculated result that is equivalent to the uncertainties in the measurements. The result of the experiment is assumed to be calculated from a set of measurements, and the objective is to express the uncertainty in the result at the same odds as those used in estimating the uncertainties in the measurements. The uncertainty in the computed result can be accurately estimated by combining the effects of each of the individual inputs using a root-sum-square method. The effect of uncertainty in a single measurement on the calculated result, if only that one measurement was in error, is determined by Equation 5.2. The partial derivative of the result R with respect to X_i is the sensitivity coefficient of the result R with respect to the measurement X_i. When multiple independent variables are used in the function R, the individual terms are combined using the root-sum-square method, as described in Equation 5.3.

$$R = R\left(X_1, X_2, X_3, \cdots, X_N\right) \qquad (5.1)$$

$$\delta R_{X_i} = \frac{\partial R}{\partial X_i}\delta X_i \qquad (5.2)$$

$$\delta R = \left\{\sum_{i=1}^{N}\left(\frac{\partial R}{\partial X_i}\delta X_i\right)^2\right\}^{1/2} \qquad (5.3)$$

The equation for uncertainty analysis is given below, with each term representing the contribution of uncertainty in one variable, δX_i, to the total uncertainty in the result, δR_i. The uncertainties in the results of this experimental validation are outlined in Table 5.5.

Table 5.5: Overall uncertainties of the measurement device used in experimental set-up.

Output	δR
Q_{charge}	+/- 14.91 W
$Q_{discharge}$	+/- 30.59 W
ϵ_{charge}	+/- 0.64 %
$\epsilon_{discharge}$	+/- 0.36 %

5.4. Measured data

The results of the experimental validation per test sequence are shown in this section. The initial system conditions might change per test sequence. The PCM was cooled to the right temperature by discharging overnight. However, due to PCM evaporation while in molten state, some of the water inside the salt hydrate might escape through the leaks in the design. The design was therefore not fully airtight. Therefore, the enthalpy range from the PCM might change due to the removed water inside the salt hydrate.

5.4.1. Air test sequence

The air sequence shows an efficiency of around 70 % when insulated on three sides and an airtight design. This is as expected, but highlights the flaws of the design. The summary of the test results is shown in Table 5.6. Here, the value for Q is the sum of all the values for $\dot{Q}$ over the test period.

Table 5.6: Results of Air test sequence.

Output	RUN 1	RUN 2	RUN 3
$Q_{charged}$ $[kJ]$	45.19	32.08	10.18
$Q_{discharged}$ $[kJ]$	32.01	21.67	7.37
Q_{Losses} $[kJ]$	13.19	10.41	2.81
η_{HEX} [-]	0.71	0.68	0.72

5.4.2. Surface test sequence

The surface test sequence measures the temperature difference of the surface temperature when the air is heated in steady state. With these measurements, the average heat transfer coefficient of the walls to the surrounding ($\bar{h}_{wall}$) is determined.

$$\dot{Q}_{losses} = h_{wall} A_{surface} \Delta T_{surface} \tag{5.4}$$

Where T_{air} is constant over time $T_{surface}$ is measured for every time step, and Q_{losses} is the total of $\dot{Q}_{losses}$ in the 30 minutes taken for the surface test sequence. . Furthermore, the values for $\mathrm{A}_{surface}$ are in this case the three uninsulated surfaces. The results of the surface test sequence are given in Table 5.7. This will result in three values for h_{wall}, where the average is taken and shown in the results.

Table 5.7: Results of surface test sequence.

Output	RUN 1	RUN 2
Q_{losses} $[kJ]$	13.9	15.9
T_{air} $[K]$	36.8	35.4
$\bar{h}_{wall}$ $[W/m^2K]$	36.9	34.8

5.4.3. Charging test sequence

The charging sequence is conducted twice for a high mass flow rate (HFR) in the hot circuit and twice for a low mass flow rate (LFR) in the hot circuit. The test is carried out throughout the day and runs for approximately 7 hours.

The charging time for the experimental set-up takes around 7 hours. The distribution of temperature is very similar to the numerical analysis, however, there is no constant melting temperature during phase change, but a period of small increase when melting occurs. There is no big distinction seen between low mass flowrate and high mass flowrate, besides that high mass flowrate has big differences between separate runs.

For the temperature difference over the heat transfer fluid, there is indeed a higher temperature difference when the PCM temperature is low, and a rapidly decreasing temperature difference when this PCM temperature is growing. However, no clear ”platform” is seen in the distribution, but rather a continuing declining decreasing slope. The temperature difference on the HTF is converging to a value of 1 K, which implies poor heat transfer characteristics. Furthermore, no big distinction between high and low mass flowrate is observed, beside an outlier in the first run for low mass flowrate. The power of charge shows the same distribution as the temperature difference. The maximum power of charging is around 250 W, while the power converges to 100 W.

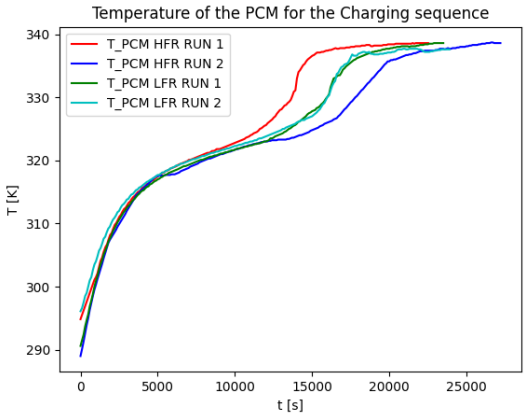

(a) PCM temperature distribution.

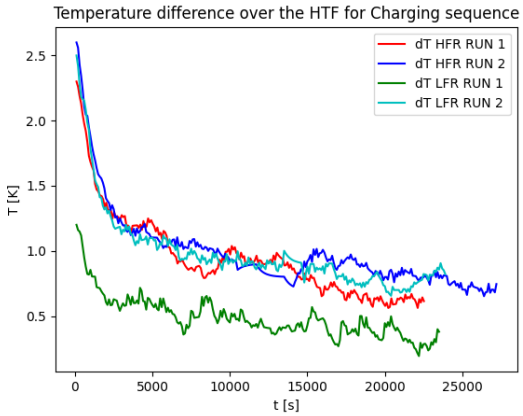

(b) Temperature difference over the HTF.

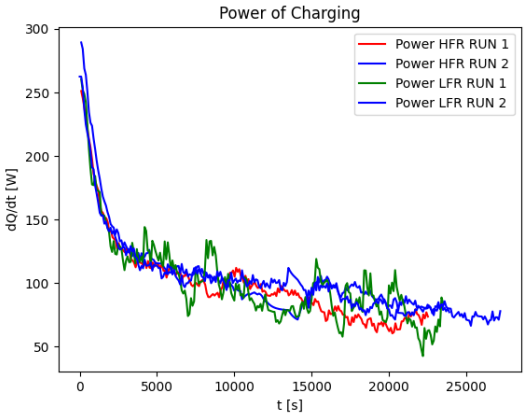

(c) Power of charging

Figure 5.5: Results of the charging sequence for high and low mass flow rates.

The total stored energy and average effectiveness given during the phase change are given in Table 5.8. Here, the total stored energy is around 1 MJ, while the theoretical storage capacity of this mass of PCM is 1.11 MJ of heat. Therefore, the designed set-up implies sufficient heat transfer characteristics. Note that this experimental value is taken for an assumed uniform PCM temperature. The PCM is not completely liquefied as shown in the Appendix C so this value is higher than in real life.

Table 5.8: Output of the charging test sequence.

Output	HFR Run 1	HFR Run 2	LFR Run 1	LFR Run 2
Q_s $[MJ]$	1.03	1.07	1.08	1.01
$\bar{\epsilon}$ [%]	7.3	3.2	7.1	6.9

5.4.4. Discharging test sequence

The discharging sequence is performed twice for a high mass flow rate (HFR) for the cold circuit, and twice for a low mass flow rate (LFR) for the cold circuit. The test is carried out overnight and lasts approximately 13 hours.

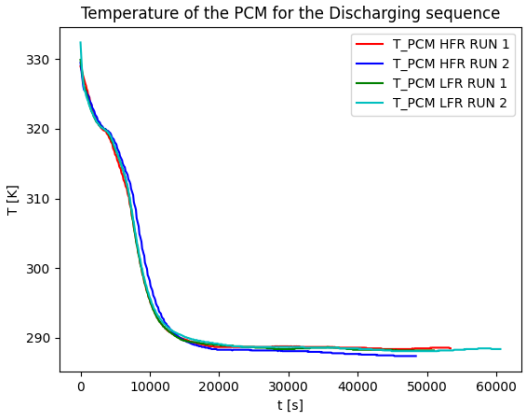

(a) PCM temperature distribution.

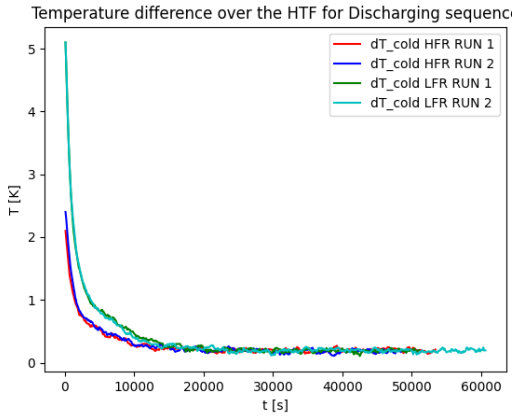

(b) Temperature difference over the HTF.

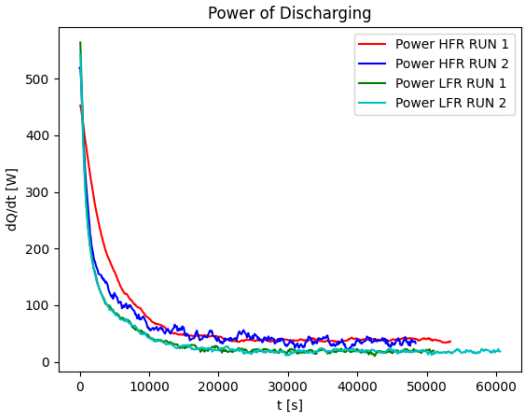

(c) Power of discharging.

Figure 5.6: Results of the discharging sequence for high and low mass flow rates.

The reference temperature is achieved after around 6 hours; thus discharging takes less time than charging, which is expected. The distribution of temperature is very similar to that in numerical analysis. However, no constant temperature is maintained during solidification, but rather a more horizontal line is seen. There is no clear distinction observable between the high and low mass flow rate runs.

For the temperature difference over the heat transfer fluid, there is indeed a higher temperature difference when the PCM temperature is high, and a rapidly decreasing temperature difference when this PCM temperature is cooling down. Similar to the charging sequence, there is no constant temperature line seen in the distribution, but a rapid decline, which diminishes the less heat is discharged from the PCM. For the second run with a low mass flow rate, the temperature difference is around 5 K, but for the other runs, the maximum outlet temperature is 2 K, which is very low. The maximum discharging power is around 450 W, while the power converges to 50 W, until it reaches zero.

Table 5.9: Output of the discharging test sequence.

Output	HFR Run 1	HFR Run 2	LFR Run 1	LFR Run 2
Q_r $[MJ]$	0.99	1.0	0.99	1.02
$\bar{\epsilon}$ $[\%]$	21.3	24.1	21.1	20.2

The total retrieved energy and the average effectiveness given during the phase change are given in Table 5.9. The average effectiveness is similar to the values of the experimental validation. The maximum effectiveness of the system arises when the outlet temperature of the HTF is the same as

the phase change temperature, which is very close to each other for the entire test run. Therefore, the values are significantly higher than the values for the charging sequence.

5.4.5. Simultaneously charging and discharging test sequence

The simultaneous charging and discharging sequence is done twice for equal flow rates with high mass flow rate for both circuits, and twice for unequal flow rates with a high mass flow rate for the hot circuit and a low mass flow rate for the cold circuit. The test is run for two hours at a time , until a stable PCM temperature is reached and the power of charging and discharging are converged to equal values.

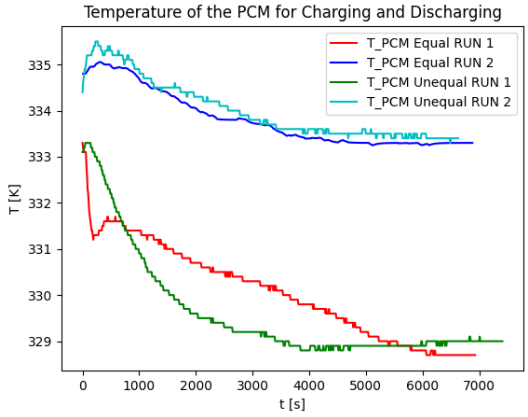

(a) PCM temperature distribution.

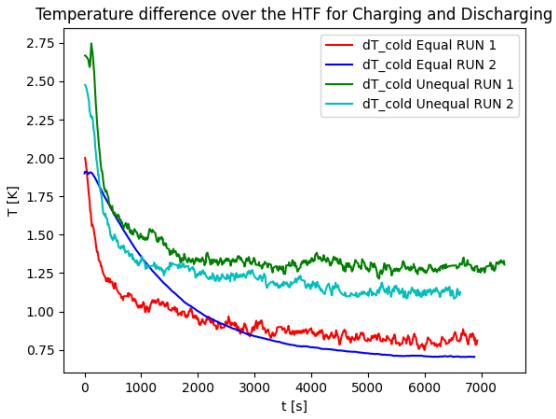

(b) Temperature difference over the HTF.

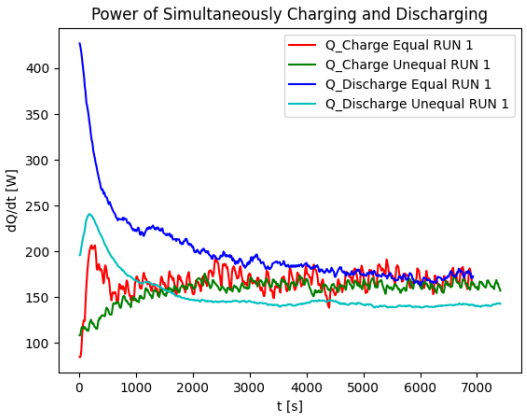

(c) Power of charging and discharging.

Figure 5.7: Results of the simultaneous charging and discharging sequence for equal and unequal mass flow rates.

The discharging test sequence runs for 2 hours. The runs are started in the molten state, where the first run for equal and unequal mass flow rates, the PCM temperature is 333 K. For the second run for either flow configuration, the PCM temperature is 335 K. The distribution of temperature is very similar to the numerical analysis where, because the discharging power is larger than the charging power, the temperature is slightly decreasing.

For the temperature difference over the heat transfer fluid only the cold circuit is taken into account. There is a clear distinction observed between the two flow configurations. In the unequal run, the mass flow rate of the cold circuit is lower, which results in a higher temperature difference over the HTF. The maximum temperature for unequal flow rates reaches around 2.5 K, while for equal flow rates this is 2 K. The configurations are decreasing to respectively 1.5 K and 1 K and rapidly decreasing temperature difference when this PCM temperature is cooling down. For the power only one test run per configuration is shown, and by doing this the phenomena are still visible. The runs are very similar to the second run. The power of charging starts at a value of 100 W and increases to around 175

W. The discharging power initially is around 250 W while it decreases to 150 W, so the power of charging and discharging are converging to equal values after a specific time, where in the unequal run the charging power increases above the discharging power after a certain time. This implies that the system has reached a steady state in the phase-change region. Here, the first run of the unequal mass flowrate configuration generates an initial outlier but still converges to the same value of 175 W.

The total retrieved energy and the average effectiveness given during the phase change are given in Table 5.10. Here, the total energy retrieved has a maximum value of 0.045 MJ, which is low but makes sense, as the PCM temperature does not drop below the melting temperature when charging and discharging, and the energy is stored at a slightly lower rate than it is retrieved. The average effectiveness is low for simultaneously charging and discharging, where the charging effectiveness is still larger than the discharging effectiveness, due to the PCM temperature staying at a high temperature, thus being closer to the outlet temperature of the hot circuit than that of the cold circuit.

Table 5.10: Output of the simultaneously charging and discharging test sequence.

Output	Equal Run 1	Equal Run 2	Unequal Run 1	Unequal Run 2
Q_r $[MJ]$	0.045	0.015	0.039	0.011
$\bar{\epsilon}_{charge}$ [%]	5.9	6.8	5.5	6.8
$\bar{\epsilon}_{discharge}$ [%]	2.2	3.4	5.5	2.7

5.5. Chapter Remarks

This chapter proves the procedure behind the experimental set-up. The measured data are collected and analysed to provide the basis for the experimentally validated model. The design of the experimental set-up is described in Appendix A. The specifications are described in this chapter, and the measured data are provided. Several outcomes of the chapter are now discussed.

- The charging test sequence shows complete melting in the time period of 7 hours. The melting distribution is only measured with one temperature sensor, which could provide inaccurate results. The liquid fraction is not completely melted as described in Appendix C. The stored energy is estimated to be around 1 MJ, and the effectiveness of charging shows poor results compared to the numerical analysis.
- The discharging test sequence provides data that implies complete melting; note that the initial conditions are a sufficient melting temperature but not a complete melted PCM. The temperature of the PCM is rapidly decreasing when discharging occurs, the same applies to the temperature difference over the HTF and the power of discharging. The total energy retrieved from the material is similar to the energy stored from charging, which is expected. The average effectiveness of discharging shows significantly improved results compared to the charging test sequence.
- The simultaneous charging and discharging sequence is initially in a molten state, however, the PCM is not fully melted. The PCM temperature does not decrease by more than 4 K while running the test for 2 hours. The temperature difference over the HTF decreases slightly as expected. Furthermore, the charging and discharging power converge until they reach an equal value of 175 W, which implies a steady state in the solidified PCM. The total retrieved heat is small because the material is charged at the same time. Average effectiveness over the phase change shows poor results, where the value over charging is slightly better than the value over discharging.

6

Results

In this chapter, the results of the proposed methodology are presented. In Section 6.1, measured data is compared with the numerical model. The numerical model from Chapter 4 is altered where the inputs are set equal to that of the experimental set-up. When the validation is complete, the results of the optimisation are provided in Section 6.2.

6.1. Validation of numerical model

The results of Chapter 5 show the output corresponding to the experimental set-up designed. To validate the model that is able to simulate the commercially available battery, the data must correspond to the measured data. The specifications of the designed test-up are used as input for the scaled model. The outputs which are compared are the distribution of the temperature of the phase-change material over time, the delivered or discharged power, and the temperature difference over the heat transfer fluid. The results are compared for the charging, discharging, and simultaneous charging and discharging scenarios. The system output is validated with the test run per scenario that delivers the most reliable results. The inputs of the system are also calibrated with the specific initial conditions corresponding to that test run.

From the numerical analysis in Chapter 4, a model is produced for two different power demands. First, the commercially available heat battery is modelled, and second, a laboratory-size model is simulated. Based on the results of this laboratory-size model, shown in Section 4.3, an experimental set-up is designed. The results of this experimental set-up are provided in Section 5.4. The dimensions and input of the numerical model are modified to resemble the experimental set-up. The results of the experimental set-up and the adjusted numerical model are compared, and if they provide similar output, the model will be validated. With this validated model, the input can be scaled to provide the same power output as the commercially available heat battery. Subsequently, the model will be optimised and assessed.

The temperature of the phase-change material in the experimental set-up is measured using only one temperature sensor. The temperature probe measures the temperature of the PCM in the middle of the enclosure. However, this does not take into account the temperature of the PCM located at the walls or in the corners of the enclosure. This PCM is further away from the hot circuit, and thus will have a lower temperature than measured. From the model implemented in Section 3.1 the numerical model assumes a uniform PCM temperature. In other words, the model considers the PCM temperature to be independent in the x, y, z-direction. However, the temperature difference over the heat transfer fluid is considered to be spatially dependent. To validate this temperature difference, a spatially averaged PCM temperature is added to the numerical model.

Heat transfer is considered one-dimensional in the y-direction. Therefore, the PCM temperature is spatially averaged in this direction. In the experimental set-up the hot circuit consists of two tubes, as well as the cold circuit. Therefore, it is assumed that there are two heat sources and two heat sinks in the y-plane. Heat sinks are the cold circuit with stationary HTF for charging the system, and heat sources are the hot circuits with stationary HTF for discharging the system. Therefore, the weight factors are assumed to be $1/3$ for the sources, sinks, and the non spatially averaged PCM temperature.

The relation used for spatial averaging and the corresponding weighted factors are given in Equation 6.1 & 6.2. To charge and discharge simultaneously, a different approach is needed. In the simultaneous charging and discharging test sequence, the PCM temperature measured is above melting temperature, while the liquid fraction is very low. With these spatially average temperatures of the PCM, a more realistic value is determined for $\Delta T_{f,o}$ and $\dot{Q}$ for all sequences. Note that Equation 6.2 is determined by matching the model results with the experimental data.

$$\bar{T} = \frac{1}{3}T_{f,i} + \frac{1}{3}T + \frac{1}{3}T_{f,i} \quad (6.1) \qquad \bar{T} = \frac{2}{3}T_{f,i,charge} + \frac{3}{12}T + \frac{1}{12}T_{f,i,discharge} \quad (6.2)$$

6.1.1. Validation of charging the system

The results of the validated model to charge the system are shown in Figure 6.1. The run time of the model is 7 hours. The output is compared to the second run with low mass flow rate, because this test run showed the most constant results.

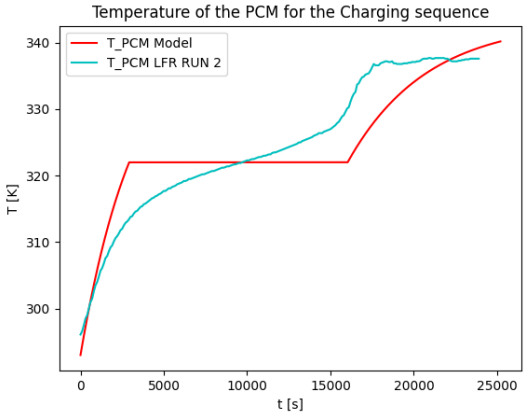

(a) PCM temperature distribution.

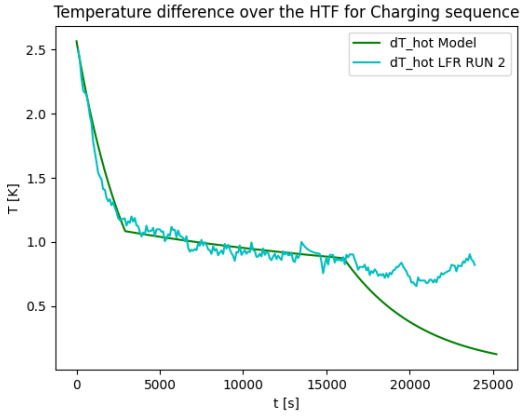

(b) Temperature difference over the HTF.

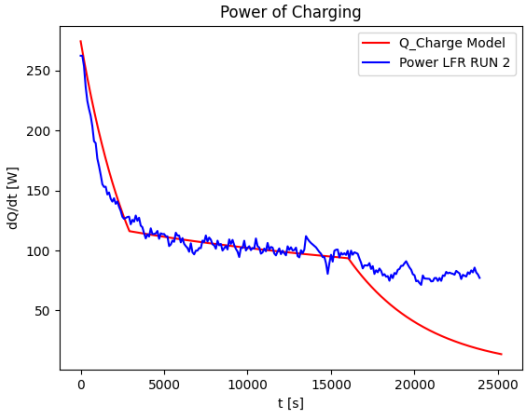

(c) Power of charging.

Figure 6.1: Validation of the numerical model with the experimental data for charging.

The maximum temperature of the phase change material is 340 K, which is a good result compared to the measured data. However, the distribution is not completely flat through the phase change in the measured data. This is due to the assumption that the temperature of the PCM remains constant during melting. The model thus assumed ideal phase change, however, in reality the PCM starts adding sensible heat in both solid and liquid phase. Thus, the melting temperature range lies between 315 K and 325 K, where the temperature slowly increases during this temperature range.

The temperature difference over the heat transfer fluid in the hot circuit decreases rapidly for the first hour, then decreases slightly when melting occurs. For the experimental data, this trend runs

for the entire time, whereas for the model, the temperature differences start dropping after melting is complete. From the results in Appendix C, it is shown that the liquid fraction is not one for the measured data. This is justified by the liquid fraction over time not growing linearly, as assumed in the model. The power of the charging sequence shares very similar results with the measured data, where the power reaches a maximum of approximately 250 W. The average effectiveness of the charging and the total stored energy are described in Table 6.1.

Table 6.1: Output of charging the system for the numerical model vs. the experimental data.

Output	Model	LFR Run 2
Q_s $[MJ]$	0.99	1.01
$\bar{\epsilon}$ $[\%]$	15.9	6.9

6.1.2. Validation of discharging the system

The validation of the measured data when discharged also shows very promising results. As seen in Figure 6.2. The run time for the model is 13 hours. The output is compared with the second run with high mass flow because this test run showed the most constant results.

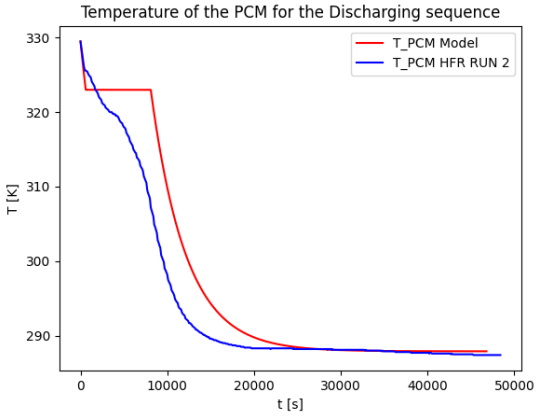

(a) PCM temperature distribution.

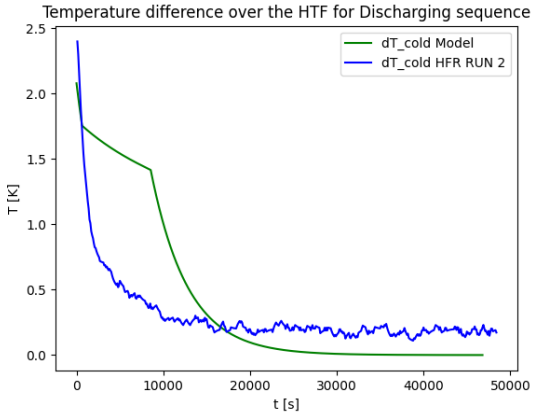

(b) Temperature difference over the HTF.

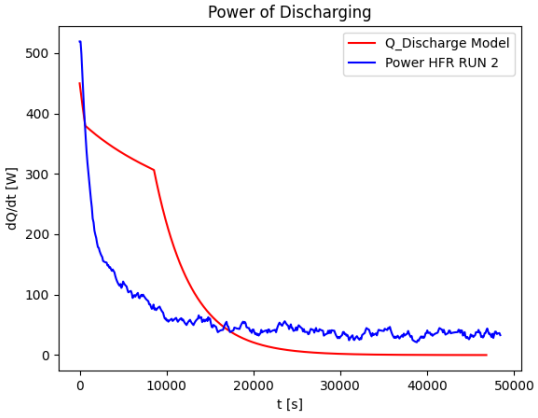

(c) Power of discharging.

Figure 6.2: Validation of the numerical model with the experimental data for discharging.

The temperature distribution of the PCM when discharging is showing the same response as the charging sequence. The model assumes a constant temperature during phase change while the experimental data suggest a decline in the decreasing temperature. Furthermore, the liquid fraction is clearly

not one in the results, while it is taken as one in the model. Therefore, the model suggests that heat is available in the PCM longer than in the real-life data. From the results of the liquid fraction in the Appendix C, it is assumed that the liquid fraction is around 0.3 in the experimental data. The temperature difference over the HTF has a maximum of 2 K in the model, which is slightly lower than the maximum temperature in the experiments, and also here the liquid fraction is much higher in the model. The discharge power shows a maximum value of 450 W in the model, which corresponds to 500 W from the experimental measurements. The average effectiveness of discharging and the total retrieved energy are described in Table 6.2. Here, the retrieved energy is very similar to that of the model.

Table 6.2: Output of discharging the system for the numerical model vs. the experimental data.

Output	Model	HFR Run 2
Q_r $[MJ]$	0.98	1.02
$\bar{\epsilon}$ [%]	5.5	24.1

6.1.3. Validation of simultaneously charging and discharging the system

The results of the validated model to simultaneously charge and discharge the system are shown in Figure 6.3. The run time for the model is 2 hours. The output is compared to the second run with the same mass flow rates, because this test run showed the most constant results.

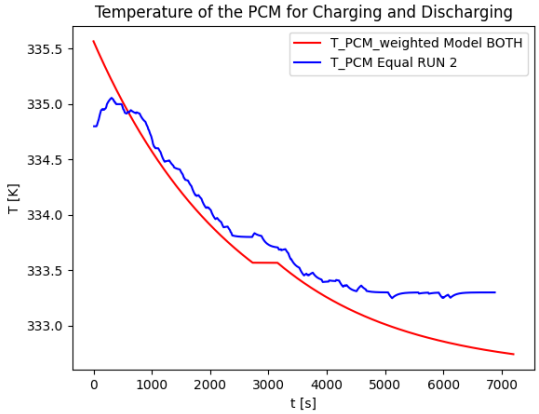

(a) PCM temperature distribution.

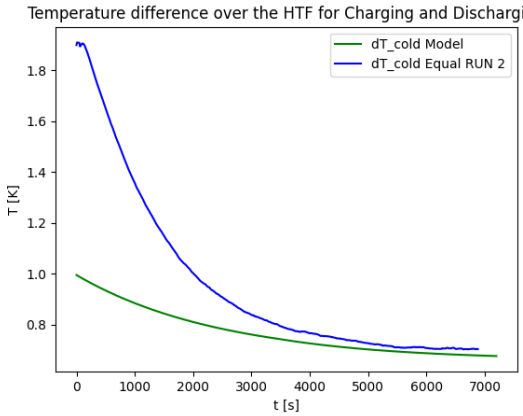

(b) Temperature difference over the HTF.

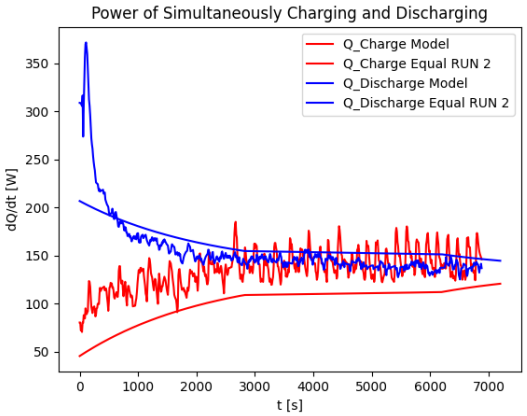

(c) Power of charging and discharging.

Figure 6.3: Validation of the numerical model with the experimental data for the simultaneous charging and discharging test sequence.

The temperature distribution of the model follows the same trend as that of the simultaneous charging and discharging test sequence. However, the maximum temperature in the model is 0.5 K higher than in the experiments. The temperature difference on the HTF is 0.8 K higher for the experimental measurement compared to the model output. The power of charging and discharging follow the same trend, where the discharge is initially higher than the charging rate, but the power values converge to around 150 W for both modes. The average effectiveness of charging and discharging and the total retrieved heat are described in Table 6.3. Here, the total retrieved heat is of the same order of magnitude of the measured data.

Table 6.3: Output of charging and discharging the system for the numerical model vs. the experimental data.

Output	Model	Equal RUN 1
Q_r $[MJ]$	0.028	0.045
$\bar{\epsilon}_{charge}$ [%]	2.4	5.9
$\bar{\epsilon}_{discharge}$ [%]	2.0	2.2

The model is validated for an ideal phase change for three different modes. Average effectiveness values show that the model is not optimised yet. To scale the system to the commercially available heat battery power output, some adjustment must be made to the specifications of the system. The system should be able to provide power without excessively increasing the mass of the PCM due to poor heat transfer properties.

6.2. Optimization of the system

The model is scaled to the power output delivered by the commercially available heat battery. While the heat transfer characteristics still apply, the distance between the tubes has to be minimised. Furthermore, the aluminium plates that are used to enhance the thermal conductivity have to be taken into account in the model. The constant dimensions for all configurations are mentioned in Table 6.4. Note that $n_{aluminium}$ is determined for the number of plates within one rectangular section of PCM.

Table 6.4: Constant-dimensional parameters and relations for all configurations.

Dimension	Value	Dimension	Relation
R_{out}	3 mm	R_{in}	R_{out} - d_{wall}
d_{wall}	0.8 mm	x_{tube}	x_{cube} - $2x_{bends}$ - $2x_{tubes,walls}$
x_{bends}	9 mm	y_{tube}	$(2n_{tubes}$ - $1)y_{between,tubes} + 2n_{tubes}D_{out})$
$x_{tubes,walls}$	10 mm	y_{cube}	$y_{tube} + 2y_{tube,walls}$
$y_{between,tubes}$	6 mm	z_{tube}	$n_{passes}D_{out} + (n_{passes}$ - $1)z_{between,tubes}$
$y_{tubes,walls}$	10 mm	z_{PCM}	$z_{tubes} + 2z_{tubes,walls}$
$z_{between,tubes}$	6 mm	z_{cube}	$\frac{\rho_s}{\rho_l} z_{PCM}$
$z_{tubes,walls}$	10 mm	$n_{aluminium}$	$\text{int}[100x_{tubes})/n_{tubes}]$

The input still relies on the three independent variables N_{tubes}, N_{passes} and L_{tube}. If either of these variables is enhanced,by doubling the length of one the dimensions of the cube, three different configurations are modelled. The three configurations are described in Section 3.2. This enhancement is done by implying specific dimensional relations with the mass of PCM enclosed in the system. Note that to determine the shape here, the number of tubes or the number of passes is delivered as input, under the condition that the power supply is met. The specific dimensional relations for the three configurations are given in Table 6.5. Using constant dimensions and relations, the specifications of the configurations are determined. The specifications of the three configurations are given in Table 5.1.

Table 6.5: Specific dimensional relations for the three configurations.

Dimension	Relation
$x_{cube,1}$	$2y_{cube}$
$n_{passes,1}$	$(y_{cube}\text{-}z_{between,tubes})/(D_{out}+z_{between,tubes})$
$x_{cube,2}$	$2y_{cube}$
$n_{passes,2}$	$\text{int}[(2y_{cube}\text{-}z_{between,tubes})/(\frac{\rho_s}{\rho_l}D_{out}+ z_{between,tubes})]$
$x_{cube,3}$	z_{cube}
$n_{tubes,3}$	$\text{int}[(2z_{cube}\text{-}2y_{tubes,walls}\text{-}y_{between,tubes})/(2y_{between,tubes}+2D_{out})]$

Table 6.6: Specifications of the three configurations.

Configuration 1			Configuration 2			Configuration 3		
Property	Value	Unit	Property	Value	Unit	Property	Value	Unit
m_{PCM}	45.8	kg	m_{PCM}	45.7	kg	m_{PCM}	45.3	kg
x_{cube}	508	mm	x_{cube}	254	mm	x_{cube}	258	mm
y_{cube}	254	mm	y_{cube}	254	mm	y_{cube}	494	mm
z_{cube}	254	mm	z_{cube}	506	mm	z_{cube}	258	mm
L_{tube}	470	mm	L_{tube}	216	mm	L_{tube}	216	mm
N_{tubes}	10		N_{tubes}	10		N_{tubes}	20	
N_{passes}	20		N_{passes}	41		N_{passes}	20	
N_{plates}	46		N_{plates}	21		N_{plates}	11	
A_{PCM}	0.133	m^2	A_{PCM}	0.129	m^2	A_{PCM}	0.065	m^2
A_f	0.133	m^2	A_f	0.129	m^2	A_f	0.063	m^2
$\dot{m}_{charge}$	10	$\frac{kg}{min}$	$\dot{m}_{charge}$	10	$\frac{kg}{min}$	$\dot{m}_{charge}$	10	$\frac{kg}{min}$
$\dot{m}_{discharge}$	10	$\frac{kg}{min}$	$\dot{m}_{discharge}$	10	$\frac{kg}{min}$	$\dot{m}_{discharge}$	10	$\frac{kg}{min}$
$\dot{m}_{sim,equal}$	10	$\frac{kg}{min}$	$\dot{m}_{sim}$	10	$\frac{kg}{min}$	$\dot{m}_{sim,equal}$	10	$\frac{kg}{min}$

The constraints on the system are the specification, which remain equal for all the three configurations. Namely the same mass of PCM and equal mass flow rates for all heat transfer modes. Furthermore, the inlet temperatures of the heat transfer fluid are equal, and the demanded power output is 8 kW. These configurations will be assessed on the five main outputs : PCM temperature distribution, HTF temperature difference, power of the system, heat stored in the material, and average effectiveness of the system. Optimisation will be assessed for all three configurations. The results of the liquid fraction for the three configurations are described in Appendix D.

6.2.1. Optimization of charging the system

The optimisation results for system charging are shown in Figure 6.4. The simulation spans 24 hours, during which one of the configurations (3) reaches the melting temperature ahead of the others. Additionally, this configuration achieves a complete liquid fraction in 48 hours, whereas the remaining configurations remain in a phase change state. Regarding the temperature difference across HTFs, there is no large difference between the various configurations. The third configuration requires a smaller temperature difference over the HTF, due to the higher PCM temperature. The charging power varies among these configurations, with one configuration standing out (3), where the system required less charging power after a while due to the increase in PCM temperature. The required charging power is around 10 kW each.

Furthermore, one of the configurations (3) stores the most heat in the material. The average charging effectiveness is in the same range for all three configurations. An overview of the average effectiveness, total charged energy, and total stored energy can be found in Table 6.7.

Table 6.7: Output of charging the system for three configurations.

Output	Config. 1	Config. 2	Config. 3
Q_s $[MJ]$	4.00	2.72	10.18
$\bar{\epsilon}$ [%]	28.7	26.1	29.3

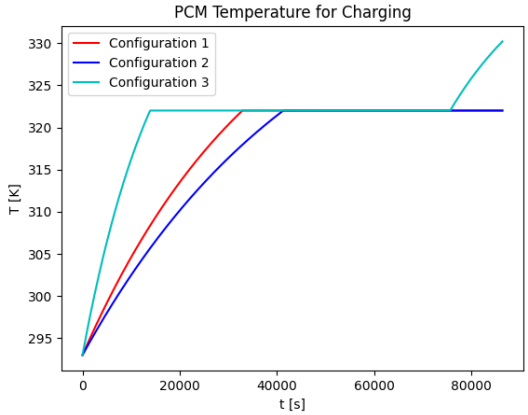

(a) PCM temperature distribution.

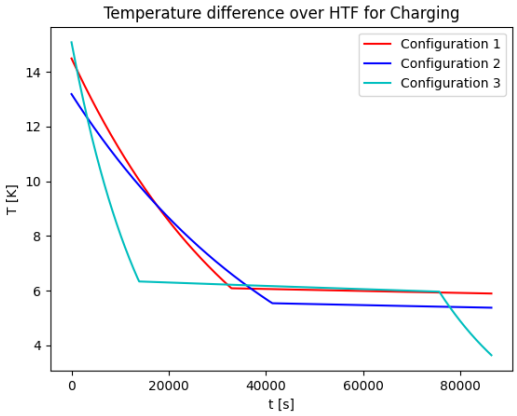

(b) Temperature difference over the HTF.

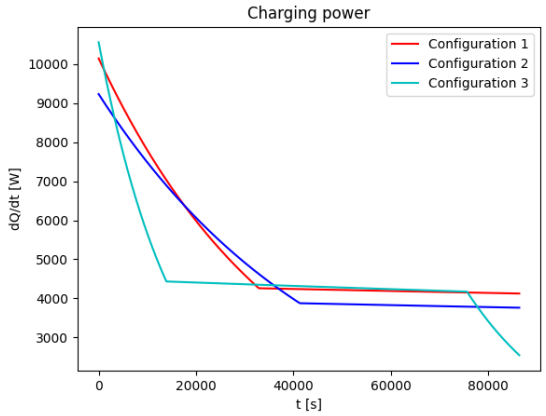

(c) Power of charging.

Figure 6.4: Charging outputs for the three configurations.

6.2.2. Optimization of discharging the system

The optimisation results for system discharging, illustrated in Figure 6.5, provide valuable information on the system performance during a 24-hour simulation. The system starts with the initial conditions of a liquid fraction of one and a temperature set at T^*. Note that configurations 1 and 2 require significantly more time and charging power to reach these initial conditions.

Notably, two configurations maintain the PCM temperature at the melting point throughout this period. Another configuration (3) undergoes a phase change, transitioning to a liquid fraction of zero after about 10 hours and eventually reaching the reference temperature after 24 hours. When considering the temperature difference across the HTF, some configurations exhibit higher temperature differences. These configurations (1,3) peak at 12 K, while one configuration (2) produces a lower temperature difference of 10 K. The third configuration experiences a decrease in temperature difference after the PCM solidifies. In terms of discharging power, the highest power output is achieved by two configurations (1,3) that deliver around 8 kW. In comparison, the configurations maintain a relatively consistent discharging power of around 7 kW. Configuration 3 experiences a significant decrease in power output

after approximately 10 hours.

The average effectiveness shows minimal variations among the different scenarios, with some configurations (1,3) demonstrating higher effectiveness. Furthermore, the total energy retrieved varies, with one configuration (3) retrieving the largest amount of heat from the material, while configuration 2 retrieves the least. The values of these outputs can be found in Table 6.8.

Table 6.8: Output of discharging the system for three configurations.

Output	Config. 1	Config. 2	Config. 3
Q_r $[MJ]$	11.05	9.00	15.28
$\bar{\epsilon}$ [%]	27.6	25.0	28.6

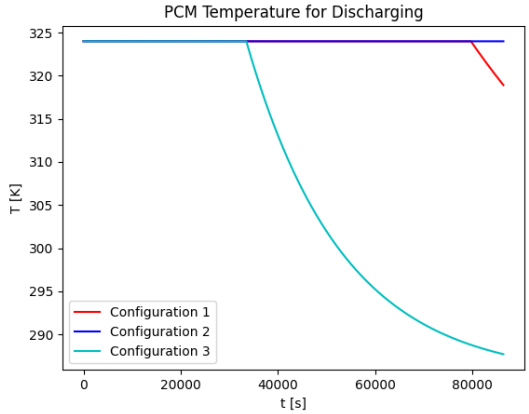

(a) PCM temperature distribution.

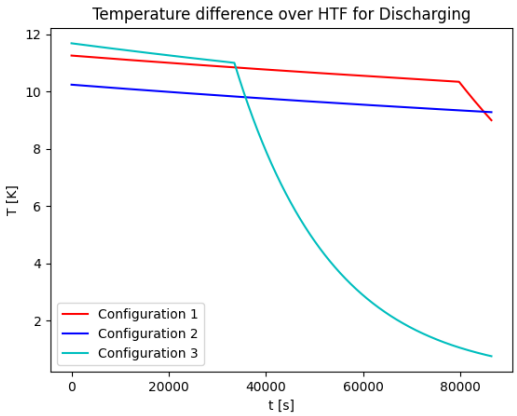

(b) Temperature difference over the HTF.

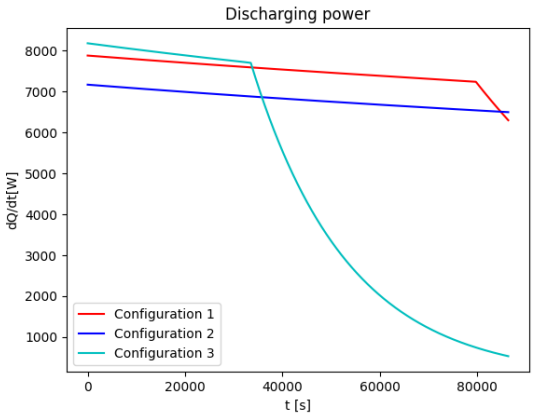

(c) Power of discharging.

Figure 6.5: Discharging outputs for the three configurations.

6.2.3. Optimization of simultaneously charging and discharging the system

The optimisation results for simultaneous system charging and discharging are depicted in Figure 6.6. These simulations span 24 hours and begin with the initial conditions of the system set at a liquid fraction of one and a temperature of T^*. Notably, for a portion of this period, two configurations maintain the PCM temperature at the melting point. The other configuration (3) exhibits different behaviour, with its PCM transitioning to a liquid fraction of zero after approximately 21 hours, eventually dropping the temperature to 318 K. Temperature differences across the HTF exhibit variations between scenarios, with some showing higher temperature differences, reaching a peak at 12 K, while others (2) exhibit

lower temperature differences. In terms of charging and discharging power, one configuration (3) shows a more noticeable convergence over time, while the others exhibit only slight convergence. Importantly, one configuration (3) converges to a power output of 6 kW, while producing a maximal power output of 8 kW surpassing the others.

For a complete overview of the average effectiveness, as well as the total heat recovered, refer to Table 6.9. In particular, one configuration (3) retrieves the largest amount of total heat from the material. This is due to the PCM completely solidifying within 24 hours.

Table 6.9: Output of charging and discharging the system for the numerical model vs. the experimental data.

Output	Config. 1	Config. 2	Config. 3
Q_r $[MJ]$	6.37	5.27	11.06
$\bar{\epsilon}_{charge}$ $[\%]$	27.4	24.3	29.5
$\bar{\epsilon}_{discharge}$ $[\%]$	28.1	25.5	28.9

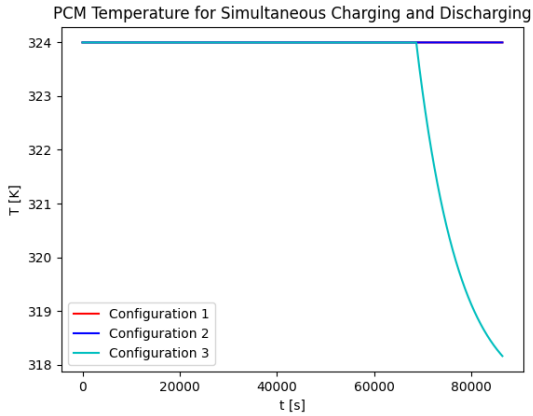

(a) PCM temperature distribution.

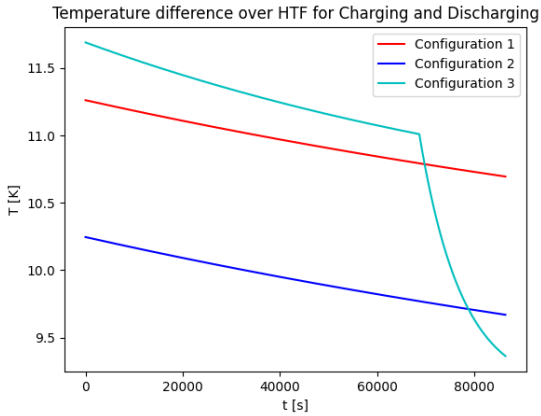

(b) Temperature difference over the HTF.

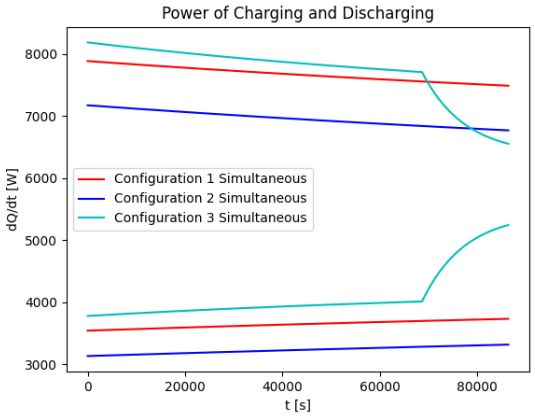

(c) Power of charging and discharging.

Figure 6.6: Output of charging and discharging the system for three configurations.

The results show interesting outputs for the different configurations. Depending on which mode of heat transfer, the latent heat storage system requires specific outputs. The results have to be compared to decide which optimisation configuration delivers the best design. The results are discussed and compared in Chapter 7. The conclusion on optimisation is formulated in Chapter 8.

7

Discussion

In this chapter, the results of the methodology are evaluated and discussed. First, the results of the optimisation are discussed in Section 7.1. In Section 7.2 the methodology is critically evaluated. Finally, recommendations on future research are described in Section 7.3.

7.1. Findings on optimization of the system

The results of the optimisation are given and briefly described in Section 6.2. The results of the liquid fraction are found in Appendix D. The findings are now discussed in this section. The three configurations are discussed in sequence. Subsequently, the optimal design is chosen on the basis of the most relevant mode of heat transfer.

Configuration 1

The first configuration is distinguished by the large length of a single pass. This is the configuration that is most similar to the designed experimental set-up. For the charging mode, the results show that the PCM temperature reaches the melting point after approximately 10 hours. The charging time for this configuration is large, but compared to the other configurations, follows the same trend. Therefore, the heat transfer characteristics of the optimised model are considered poor. The first configuration does not fully melt within the 24 hour time period but reaches a final value of $\chi = 0.38$. This is reflected in the stored heat in the material, where the fist configuration does not exceed a value of $Q_s = 4\ MJ$. Keep in mind that the storage capacity for this amount of PCM is 10.4 MJ, without taking into account the sensible heat stored in the liquefied PCM. The commercially available heat battery from Chapter 4 is able to store 40 MJ in 72 hours, when running the model for 72 hours for this configuration a total stored energy of 10.3 MJ is established, while using 3 times less PCM. The charging time for fully melting the PCM in this configuration is approximately 48 hours, which is 6 h longer than the commercially available heat battery. The average effectiveness of the first configuration is significantly higher than that of the commercially available heat battery.

For the discharge mode, the results show that the PCM temperature remains at the melting point for a time period of 24 hours. This results in a long discharge time for this configuration. Therefore, the heat transfer characteristics of the optimised model are still considered poor. The first configuration fully solidifies within the time period of 24 hours, but only after 23 hours. This is reflected in the heat recovered in the material, where $Q_r = 11.05\ MJ$ is collected from the material. The commercially available heat battery from Chapter 4 is capable of retrieving 44.36 MJ in 72 hours, when running the model for 72 hours for this configuration a total retrieved energy of 15.7 MJ is established, indicating a total discharge of the PCM in this time period. The discharging time for fully melting the PCM in this configuration is thus approximately 72 hours, similar to that of the commercially available heat battery. The average effectiveness of the first configuration is, however, significantly higher than that of the model from the numerical analysis.

For the simultaneously charging and discharging modes, the results show that the PCM temperature remains at the melting point for a time period of 24 hours. This shows that the PCM is still solidifying, while the retrieved heat is larger than the stored heat. The liquid fraction after 24 hours remains at χ

= 0.38. This is reflected in the heat retrieved from the material, where 6.37 MJ is collected from the material. The commercially available heat battery from Chapter 4 is able to retrieve 15.48 MJ in 48 hours, when the model is run for 48 hours, for this configuration a total retrieved heat of 10.7 MJ is established. The average effectiveness of the first configuration is similar to that of the model from the numerical analysis.

The first configuration performs relatively poorly during the charging sequence, while still showing an improvement in effectiveness compared to the model based on the commercially available heat battery. However, the charging time periods are long and thus are not favourable for energy storage applications where energy demand is on short notice. Additionally, the charging power required is large over this extended period resulting in poor heat transfer characteristics and a large amount of nonused heat for charging. The discharging time, on the other hand, is also large; thus, when time is not an issue, the system can deliver heat for an extended period, with a relatively high outlet temperature of the HTF. For simultaneously charging and discharging the system, with the PCM in molten state, a large discharging power can be delivered over a long period, while requiring a relatively low charging power.

Configuration 2

The second configuration is distinguished by the high number of passes per tube. This is the configuration that is most similar to the commercially available heat battery. For the charging mode, the results show that the PCM temperature reaches the melting point after approximately 11.5 hours. The charging time for this configuration is relatively longer compared to that of the other configurations. Therefore, the heat transfer characteristics of this optimised model are very poor. The second configuration does not fully melt within the 24 hour time period but reaches a final liquid fraction value of $\chi = 0.26$. This is reflected in the stored heat in the material, where the first configuration does not exceed a value of 2.72 MJ. Keep in mind that the storage capacity for this amount of PCM is 10.4 MJ, without taking into account the sensible heat stored in the liquefied PCM. When the model is run for 72 hours for this configuration, a total stored energy of 10.3 MJ is established, while using 3 times less PCM than the commercially available heat battery. The charging time for fully melting the PCM in this configuration is approximately 63 hours, which is significantly higher than the melting time of 42 hours in correlation to the locally available heat battery. The average effectiveness of the second configuration produces and charging effectiveness of 25 %, which is better than the model from the numerical analysis.

For the discharge mode, the results show that the PCM temperature remains at the melting point for a time period of 24 hours. Therefore, the heat transfer characteristics of the optimised model are considered poor. The second configuration does not solidify completely during this period, but reaches a liquid fraction value of $\chi = 0.13$. This is reflected in the heat retrieved from the material, where 1 MJ is collected from the material. When running the model for 72 hours for this configuration, a total retrieved energy of 15.4 MJ is established, indicating a total discharge of the PCM in this time period, where the PCM reference temperature is achieved. The discharging time for fully melting the PCM in this configuration is thus approximately 72 hours, similar to the commercially available heat battery. The average effectiveness of the second configuration is, however, significantly higher than that of the model from the numerical analysis.

In the simultaneous charging and discharging mode, the results indicate that the PCM temperature remains constant at the melting point for a duration of 24 hours. This indicates that the PCM remains in a solid state, while the retrieve heat is larger than the stored heat. The liquid portion after 24 hours remains at χ =0.49. This is reflected in the heat extracted from the material, where 5.27 MJ is extracted from the material. When we run the model for this configuration for 48 hours, it yields a total extracted heat of 9.12 MJ. The average effectiveness of the second configuration is similar to that of the model in the numerical analysis.

The second configuration performs very poorly during the charging sequence, with the lowest stored energy of all three configurations. Furthermore, the charging time periods are long and thus are not favourable for energy storage applications where energy demand is on short notice. The charging power required for melting is large, which highlights the poor heat transfer characteristics. The discharging time is equally large, because it depends on the same principles. When the system is initially melted, the system can deliver heat for an extended period, with a relatively high outlet temperature of the HTF. For simultaneously charging and discharging, the system, with the PCM in molten state, can deliver large discharging power over a long period, while requiring a relatively low charging power. However,

the temperature difference over the HTF is relatively low.

Configuration 3

The third configuration is characterised by a large number of parallel tubes. In the charging mode, the results indicate that the PCM temperature attains the melting point in approximately 4 hours, resulting in a relatively short charging time. Consequently, the heat transfer characteristics of this configuration are considered excellent, surpassing those of the other configurations. The third configuration achieves complete melting in 21 hours, which is significantly faster than the commercially available heat battery. After 24 hours, the total stored heat in the material is 10.18 MJ, fully using the storage capacity of the material of 10.4 MJ, without accounting for the sensible heat stored in the liquefied PCM. Notably, the charging power required for full PCM melting is significantly lower than that of the other configurations, and the average effectiveness of the third configuration surpasses that of the commercially available heat battery by a significant margin.

For the discharging mode, the results show that the PCM temperature fully solidifies after 9 hours. The reference temperature of the material is reached within the time period of 24 hours, which amplifies the excellent heat transfer characteristics. This is reflected in the heat recovered in the material, where 15.23 MJ is collected from the material. The temperature difference over the HTF to charge the system is drastically decreasing after the PCM has solidified, which is a disadvantage compared to the other configurations. The same applies to the discharging power that drops to a value below 1 kW after 24 hours. However, the average effectiveness of the third configuration is significantly higher than that of the commercially available heat battery modelled in the numerical analysis.

For the simultaneous charging and discharging modes, the results show that the PCM fully solidifies after 19 hours. In the 24 hour period, the temperature drops even further to a value of 318 K. The total solidification is reflected in the heat recovered from the material, where 11.06 MJ is collected from the material. When the model runs for 48 hours for this configuration, a total heat retrieved of 11.13 MJ is established. Where after 48 hours, the model is completely solidified and the charging power remains constant at 5.5 kW, while the discharging power remains constant at 6.4 kW. The PCM temperature is 317 K during this equilibrium. The average effectiveness of the second configuration is similar to that of the commercially available heat battery model.

The third configuration performs outstandingly during the charging sequence, showing great improvement compared to the other configurations as well as the model based on the commercially available heat battery. The time periods for charging are reasonable and thus favourable for energy storage applications where the energy demand is on short notice.furthermore, the charging power required is relatively low over this extended period resulting in excellent heat transfer characteristics and the amount of non-used heat is minimised. The discharging time is also reasonable, where the system can deliver heat for a period of 10 hours, with a relatively high outlet temperature of the HTF. The discharging power is constant for a shorter time than the other configurations; keep in mind that the other configuration requires almost 3 times more charging power to fully melt the material. For the charging and discharging sequence, it can be concluded that the third configuration is very applicable for residential appliances like the commercial heat battery. For simultaneously charging and discharging, the system, with the PCM in molten state, can deliver large discharging power over a period of 24 hours; however, also requires a large charging power over this period compared to the other configurations. For this sequence, the third configuration will fully solidify in a period of 48 hours and reaches steady state.

Optimal design

As described, the commercially available heat battery is most similar to the second configuration, where the number of passes is high in comparison with the other independent variables. From the results this is considered the least efficient storage system, meaning that optimisation is indeed needed for this system. The second configuration, where the length of a single pass is doubled, has the most resemblance to the designed experimental set-up. As in Section 5.4 implies that this is also not the optimal design which is emphasised in the results. The third configuration is specific for it's high amount of parallel tubes. The results indicate that the optimisation through this configuration has significant positive effects on the output of the latent heat storage system.

Therefore, the optimal design is determined to be the third configuration for charging and discharging the system. The third configuration has significantly better heat transfer characteristics than the other two configurations. This is expressed in the relatively short charging and discharging time and high

energy stored and retrieved from the material. The charging power of the first configuration also meets the requirement of providing a power output of 8 kW, up to 10 hours. The third configuration is best suitable for delivering stored energy on short notice and is efficient in storing heat in the PCM. These are the criteria that define an efficient latent heat storage system.

For simultaneously charging and discharging, the first configuration shows the best results. Note that the outputs are given for a situation where the PCM is initially in the molten state. To reach this molten state, a significantly longer charging time and higher charging power are needed than for the first configuration. When this is taken into account, suddenly the outputs of the simultaneously charging and discharging modes are less efficient than they appear. Meanwhile, the first configuration can produce a power output of 10 kW for an extended period, but requires more charging power if you run the system for longer than 48 hours.

To conclude this discussion : With all the configurations discussed, the optimal design is chosen as configuration 3. Implementing this design in a commercially available heat battery will reduce the mass of PCM, the size of the system, and the charging time. The temperature difference over the HTF for this configuration is not up to standard for supplying domestic hot water. This could be achieved by improving the optimisation of the dimensional parameter , reducing the mass flow rate of the cold circuit, or adding a heat source in series.

7.2. Evaluation of methodology

The second part of the discussion will evaluate the methodology by providing critical feedback. The methodology is revisited with the results in mind. The main purpose of the evaluation is to recognise shortcomings and ultimately provide recommendations for further research.

The first part evaluated in the methodology is the numerical analysis. One of the assumptions made in Chapter 4 is that the PCM has a uniform temperature throughout the enclosure. For more realistic results, the PCM temperature should be spatially dependent throughout the material. This would result in having the temperature of the PCM have a gradient in all directions ($\frac{dT}{dx}, \frac{dT}{dy}, \frac{dT}{dz}$).

The liquid fraction is also assumed to be spatially independent, resulting in a linear distribution of the liquid fraction in the material. In this methodology, the liquid fraction is only time-dependent. When the thermal resistance is calculated, as described in Section 3.2.1, the liquefied fraction of the width of the PCM (dy) is determined per time step. Through this, a fraction of a length of PCM is determined, which is a spatial value. However, it does not take into account where this melted material is located in the enclosure. It will be harder for the material at the far corners of the material to reach heat through conductive heat transfer. Furthermore, the inlet of the hot circuit is located at the bottom of the material, meaning that the PCM will melt from the ground up. This means that the liquid fraction will have a nonlinear distribution where the increase in the liquid fraction will decrease when the fraction approaches a value of 100 %, as shown in Figure 7.1. The assumption of one-dimensional heat transfer, where no convection occurs, causes the liquid fraction to be nonlinear. Natural convection is the superior mode of heat transfer when melting [46]. In our case, we take the conductivity of the liquid vs. the solid part so that there is no natural convection, which leads to a linear melting fraction. This can be improved by modelling the heat transfer as three-dimensional and adding convective heat transfer.

Another part of the methodology which could use an improved approach is the experimental validation. The testing conditions of the experimental set-up are suboptimal. The foremost problem with the experimental validation is the maximum achievable liquid fraction. The PCM cannot fully melt during the time period of the test sequences. An overview of the maximum liquid fraction per test sequence is given in Appendix C. This could be improved by extending the charging time of the experimental set-up, or by inserting aluminium plates into the material to enhance the thermal conductivity of the material.

Due to the use of one temperature sensor, the data show only the PCM temperature in the middle of the material. Therefore, the melting distribution is only represented in the middle of the PCM, meaning that the melting is not represented at the far sides of the enclosure. The measured PCM temperature gives misleading results for the temperature at the inlet and outlet of the HTF. This is taken into consideration by spatially averaging the PCM temperature using Equations 6.1 and 6.2. This could be improved by adding more temperature sensors to the experimental set-up. By measuring the PCM temperature at multiple locations, the value will be more accurate. An accurate PCM temperature will

result in a more accurate temperature difference over the HTF and a more accurate power of the system. When the PCM temperature is assumed to be not uniform, the validated model will also predict more accurate outputs.

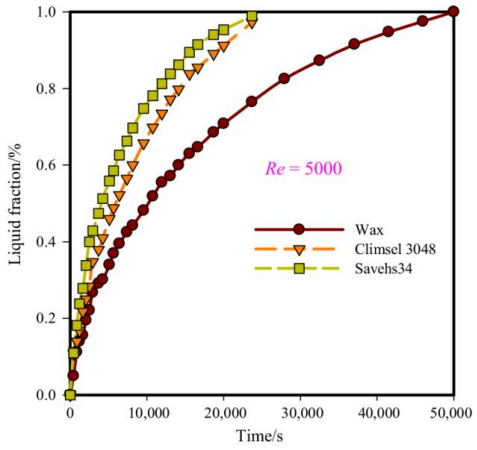

Figure 7.1: Nonlinear liquid fraction as described by Miansari et al. [47].

Optimisation of the design is based on the three configurations described in Section 3.2.3. The configurations are simulated with the validated model. The model is then scaled by the dimensional relations and is constrained by the power output of 8 kW. These dimensional relations are based on the independent variables N_{tubes}, N_{passes} and L_{tube}. Power output is the main constraint of scaling. However, the optimisation gives three configurations which are only based on enhancing one of these three independent variables. A more accurate optimisation would be to express all the equations in the model in constants and independent variables. Now, the model would be able to simulate a number of configurations with a constraint of power output or mass of PCM. The configurations expressed in the independent variables are assessed on the basis of their effectiveness, power, and stored heat. By plotting these independent variables against these outputs, the best scoring combinations could be used as the basis of design for the configurations. Through this method, the configurations represent a more accurate optimisation than the configurations used in this methodology.

Another constraint to designing these configurations would be a minimum temperature difference over the HTF. For optimal results, this temperature difference is not up to the standard for the supply of domestic hot water. To improve the optimisation, an additional constraint is added to ensure that water will provide hot water at a minimum of 60 °C in the cold circuit for a prolonged period of time.

7.3. Recommendations

The improvement in the evaluation are examples of recommendations for further research. These methods are able to improve the methodology in this thesis. An example of an improvement on this methodology could be conducted with another experimental validation where the optimal design outputs are compared with real-life data. Instead of improvement, there are also some options to extend the research and make it more applicable to other types of latent heat storage systems. Further research could be done to scale the latent heat storage system to even larger power outputs. Conventional boiler sizes are available in different sizes that reach 45 kW of the power supply. To provide this size, a subsequent methodology can be defined. Where the numerical model is sized to these requirements and then optimised.

Another follow-up research goal would be optimisation of the described system by implementing the latent heat storage system in a designed thermal heat network. By inserting a heat pump into the said thermal network, the outlet temperature at the cold circuit can be increased to be able to provide domestic hot water to residents [48]. When the emphasis is on providing renewable energy, a solar collector could be added to the thermal network. Thermal collectors are often combined with PCM in the form of solar water heaters [2]. When solar energy is used to charge the PCM in the latent heat storage system, the system is fully supplied by renewable energy.

8

Conclusions

In this research, a new methodology is proposed to determine the optimal design of a thermal energy storage system for a specific power demand. The main research question answered in the conclusion of this thesis is :

What will be the results of the optimisation of a latent heat storage system containing a salt hydrate as a phase-change material?

Several studies have been conducted on latent heat storage systems. In these studies, salt hydrates are used as the phase-change material, but the designs are divergent from those of the commercially available heat battery considered in this methodology. Additionally, the scaleable properties of the numerical model are limited. Therefore, to make this research of added value, the methodology developed must meet certain accuracy and practical standards. These design requirements are translated into three subquestions that are addressed in this thesis. The answer to each of the subquestions is formulated below.

(1) How will the specifications and output of the latent heat storage system be affected when altering the scale of the system?

A numerical model is developed to simulate the specifications and outputs of the commercially available heat battery and a smaller laboratory-scale version of the system which serves as the basis for the experimental set-up. The entire analysis is based on numerical simulations.

The results of the numerical analysis reveal various trends, such as a nonlinear growth in the charging time with an increase in the mass of the PCM, a shorter discharge time compared to the charging time, and a constant temperature at the melting point during simultaneous charging and discharging. The temperature difference in the HTF increases with larger-scale systems as a result of an increased number of passes and tube length, while the laboratory scale also exhibits significant temperature differences as a result of low mass flow rates. The power to charge and discharge the system is uniform with these temperature differences. The average effectiveness of the commercially available heat battery is found to be low, suggesting a need for optimisation. Interestingly, scaling down the system leads to a significant increase in average effectiveness, indicating that the system size affects this parameter. The numerical analysis successfully produces a model capable of designing thermal batteries based on commercially available heat batteries. Furthermore, the model can be adapted to different scales and power demands, providing realistic outputs for design and evaluation. The accuracy of the scaleable model is addressed in the second subquestion.

(2) How accurate are the outputs of the latent heat storage system compared to the experimental data?

To ensure accuracy, the dimensions of the model and the inputs are adjusted to match the experimental conditions. Calibration is carried out to align the model's inputs with specific initial conditions for each test run scenario. An important aspect of validation is to address the spatial variation of the temperature of phase-change material. Although the experimental set-up uses a single temperature sensor in the middle of the enclosure, the model assumes a uniform PCM temperature. To account for variations, a spatially averaged PCM temperature is introduced.

The validation covers three scenarios: charging, discharging, and simultaneous charging and discharging. The results of charging the system are presented with a run time of 7 hours. The model is closely aligned with the experimental data, especially in terms of maximum PCM temperature and power output. The validation process extends to discharging the system with a runtime of 13 hours. Similarly to charging, the model's outputs closely match the experimental data, including temperature distribution, power output, and temperature difference. The performance of the model in simulating simultaneous charging and discharging is assessed, revealing results that closely resemble experimental data, with minor differences in temperature values.

In general, the validation demonstrates promising results and identifies areas for improvement, particularly related to the idealised assumption of phase change behaviour. The validation process laid the groundwork for developing a more accurate and reliable numerical tool for the analysis of heat battery systems, with the goal of optimising their performance.

(3) What is the optimal design configuration of the latent heat storage system for a specific power demand?

The results of the optimisation study focus on three different configurations of a latent heat storage system. The primary objective is to identify the most suitable configuration for the various modes of heat transfer. The first configuration exhibits a prolonged charging time, with the phase-change material failing to fully melt in a 24 hour period. For discharging, this configuration achieves complete solidification in 24 hours. During simultaneous charging and discharging, the PCM remains partially solid while heat is retrieved. The second configuration shares similarities with the first in terms of long charging time and incomplete melting within 24 hours. When discharged, the PCM remains at the melting point for 24 hours, but yields a relatively small amount of retrieved heat. When the PCM is simultaneously charged and discharging, it also remains solid during heat recovery. The third configuration stands out with a relatively short charging time of around 4 hours, achieving full PCM melting in 21 hours. In the discharging mode, it rapidly solidifies within 9 hours, indicating excellent heat transfer characteristics, and recovers a significant amount of heat. During simultaneous charging and discharging, the PCM is kept in a partially solid state while efficiently releasing heat. The average effectiveness of the third configuration provides constant results of approximately 28 %, for the three heat transfer modes.

As a result of these analyses, it can be concluded that configuration 3 is the optimal design for the latent heat storage system. It offers shorter charging and discharging times, efficient heat transfer, and higher stored and retrieved energy. This configuration is deemed suitable for delivering stored energy promptly and efficiently and storing heat in the PCM. However, caution is given regarding the temperature difference over the heat transfer fluid, which may fall short of the requirements for providing domestic hot water without additional measures. Suggestions are made to further optimise the dimensional parameters, reduce the cold circuit mass flow, or add a heat source in series to address this issue. In summary, Configuration 3 is selected as the optimal design for the latent heat storage system, offering improved performance compared to other configurations and the potential for further improvements to meet specific application needs, such as domestic hot water supply.

References

[1] "A review of thermal absorbers and their integration methods for the combined solar photovoltaic/thermal (PV/T) modules". **in***Renewable and Sustainable Energy Reviews*: 75 (2017), **pages** 839–854. ISSN: 18790690. DOI: 10.1016/j.rser.2016.11.063.

[2] A. Sharma **and** C. R. Chen. "Solar Water Heating System with Phase Change Materials". **in***Int. Review of Chemical Engineering*: 1 (4 2009).

[3] F. Zhou, J. Ji, W. Yuan, M. Modjinou, X. Zhao **and** shengjuan Huang. "Experimental study and performance prediction of the PCM-antifreeze solar thermal system under cold weather conditions". **in***Applied Thermal Engineering*: 146 (**january** 2019), **pages** 526–539. ISSN: 13594311. DOI: 10.1016/j.applthermaleng.2018.10.038.

[4] T. Kousksou, P. Bruel, A. Jamil, T. E. Rhafiki **and** Y. Zeraouli. "Energy storage: Applications and challenges". **in***Solar Energy Materials and Solar Cells*: 120 (PART A 2014), **pages** 59–80. ISSN: 09270248. DOI: 10.1016/j.solmat.2013.08.015.

[5] Y. Dai, L. Chen, Y. Min, Q. Chen, Y. Zhang, F. Xu, K. Hu **and** J. Hao. "Active and Passive Thermal Energy Storage in Combined Heat and Power Plants to Promote Wind Power Accommodation". **in***Journal of Energy Engineering*: 143 (5 **october** 2017). ISSN: 0733-9402. DOI: 10.1061/(asce)ey.1943-7897.0000466.

[6] *A review of available methods for seasonal storage of solar thermal energy in residential applications*. **september** 2011. DOI: 10.1016/j.rser.2011.04.013.

[7] B. Xu, P. Li **and** C. Chan. *Application of phase change materials for thermal energy storage in concentrated solar thermal power plants: A review to recent developments*. **december** 2015. DOI: 10.1016/j.apenergy.2015.09.016.

[8] M. Carmona **and** M. Palacio. "Thermal modelling of a flat plate solar collector with latent heat storage validated with experimental data in outdoor conditions". **in***Solar Energy*: 177 (**january** 2019), **pages** 620–633. ISSN: 0038092X. DOI: 10.1016/j.solener.2018.11.056.

[9] Y. Tian **and** C. Y. Zhao. "A review of solar collectors and thermal energy storage in solar thermal applications". **in***Applied Energy*: 104 (2013), **pages** 538–553. ISSN: 03062619. DOI: 10.1016/j.apenergy.2012.11.051.

[10] K. Pielichowska **and** K. Pielichowski. *Phase change materials for thermal energy storage*. 2014. DOI: 10.1016/j.pmatsci.2014.03.005.

[11] H. Jouhara, A. Żabnieńska-Góra, N. Khordehgah, D. Ahmad **and** T. Lipinski. "Latent thermal energy storage technologies and applications: A review". **in***International Journal of Thermofluids*: 5-6 (**august** 2020). ISSN: 26662027. DOI: 10.1016/j.ijft.2020.100039.

[12] E. Bellini. *PCM-based thermal battery to store solar power via heat pump*. **october** 2022. URL: https://www.pv-magazine.com/2022/10/17/pcm-based-thermal-battery-to-store-solar-power-via-heat-pump/.

[13] A. Pasupathy, R. Velraj **and** R. V. Seeniraj. *Phase change material-based building architecture for thermal management in residential and commercial establishments*. **january** 2008. DOI: 10.1016/j.rser.2006.05.010.

[14] J. A. Ramsay. *A NEW METHOD OF FREEZING-POINT DETERMINATION FOR SMALL QUANTITIES*.

[15] M. M. Farid, A. M. Khudhair, S. A. K. Razack **and** S. Al-Hallaj. *A review on phase change energy storage: Materials and applications*. **june** 2004. DOI: 10.1016/j.enconman.2003.09.015.

[16] J. B. Ott **and** J. Boerio-Goates. *Chemical thermodynamics : principles and applications*. Academic Press, 2000, **page** 664. ISBN: 0125309902.

[17] D. Jansone, M. Dzikevics **and** I. Veidenbergs. "Determination of thermophysical properties of phase change materials using T-History method". **in**volume 147: Elsevier Ltd, 2018, **pages** 488–494. DOI: 10.1016/j.egypro.2018.07.057.

[18] T. Yang, W. P. King **and** N. Miljkovic. *Phase change material-based thermal energy storage*. **august** 2021. DOI: 10.1016/j.xcrp.2021.100540.

[19] L. F. Cabeza, G. Zsembinszki **and** M. Martín. "Evaluation of volume change in phase change materials during their phase transition". **in***Journal of Energy Storage*: 28 (**april** 2020). ISSN: 2352152X. DOI: 10.1016/j.est.2020.101206.

[20] N. Bianco, A. Fragnito, M. Iasiello, G. M. Mauro **and** L. Mongibello. "Subcooling Effect on PCM Solidification: A Thermostat-like Approach to Thermal Energy Storage". **in***Energies*: 16 (12 **june** 2023). ISSN: 19961073. DOI: 10.3390/en16124834.

[21] H. Huang, J. Fan, J. Lin, Q. Zhao, Y. Zhang **and** Y. Xiao. "Numerical phase change model considering crystal growth under supercooling". **in***Applied Thermal Engineering*: 200 (**january** 2022). ISSN: 13594311. DOI: 10.1016/j.applthermaleng.2021.117685.

[22] J. A. Duffie **and** W. A. Beckman. *Solar engineering of thermal processes*. Wiley, 2013, **page** 910. ISBN: 9780470873663.

[23] Q. Wang, D. Zhou, Y. Chen, P. Eames **and** Z. Wu. "Characterization and effects of thermal cycling on the properties of paraffin/expanded graphite composites". **in***Renewable Energy*: 147 (**march** 2020), **pages** 1131–1138. ISSN: 18790682. DOI: 10.1016/j.renene.2019.09.091.

[24] R. Kothari, A. Ahmad, S. K. Chaurasia **and** O. Prakash. "Experimental analysis of the heat transfer rate of phase change material inside a horizontal cylindrical latent heat energy storage system". **in***Materials Science for Energy Technologies*: 5 (**january** 2022), **pages** 208–216. ISSN: 25892991. DOI: 10.1016/j.mset.2022.02.004.

[25] A. Mills. *Basic Heat and Mass Transfer*. Prentice Hall, 1999. ISBN: 9780130962478. URL: https://books.google.nl/books?id=C5AvAQAAIAAJ.

[26] M. M. Hassan **and** Y. Beliveau. "Modeling of an integrated solar system". **in***Building and Environment*: 43 (5 **may** 2008), **pages** 804–810. ISSN: 03601323. DOI: 10.1016/j.buildenv.2007.01.019.

[27] G. Liu, T. Xiao, J. Guo, P. Wei, X. Yang **and** K. Hooman. "Melting and solidification of phase change materials in metal foam filled thermal energy storage tank: Evaluation on gradient in pore structure". **in***Applied Thermal Engineering*: 212 (**july** 2022). ISSN: 13594311. DOI: 10.1016/j.applthermaleng.2022.118564.

[28] D. J. Morrison **and** S. I. Abdel-Khalikt. "EFFECTS OF PHASE-CHANGE ENERGY STORAGE ON THE PERFORMANCE OF AIR-BASED AND LIQUID-BASED SOLAR HEATING SYSTEMS". **in***Solar Energy*: 20 (1978), **pages** 57–67.

[29] N. K. Bansal **and** D. Buddhit. "AN ANALYTICAL STUDY OF A LATENT HEAT STORAGE SYSTEM IN A CYLINDER". **in***Energy Convers. Mgmt*: 33 (4 1992), **pages** 235–242.

[30] A. A. Ghoneim. "COMPARISON OF THEORETICAL MODELS OF PHASE-CHANGE AND SENSIBLE HEAT STORAGE FOR AIR AND WATER-BASED SOLAR HEATING SYSTEMS". **in**42: (3 1989), **pages** 209–220.

[31] S. Canbazoğlu, A. Şahinaslan, A. Ekmekyapar, Y. G. Aksoy **and** F. Akarsu. "Enhancement of solar thermal energy storage performance using sodium thiosulfate pentahydrate of a conventional solar water-heating system". **in***Energy and Buildings*: 37 (3 **march** 2005), **pages** 235–242. ISSN: 03787788. DOI: 10.1016/j.enbuild.2004.06.016.

[32] M. Mazman, L. F. Cabeza, H. Mehling, M. Nogues, H. Evliya **and** H. Ö. Paksoy. "Utilization of phase change materials in solar domestic hot water systems". **in***Renewable Energy*: 34 (6 **june** 2009), **pages** 1639–1643. ISSN: 09601481. DOI: 10.1016/j.renene.2008.10.016.

[33] I. Al-Hinti, A. Al-Ghandoor, A. Maaly, I. A. Naqeera, Z. Al-Khateeb **and** O. Al-Sheikh. "Experimental investigation on the use of water-phase change material storage in conventional solar water heating systems". **in***Energy Conversion and Management*: 51 (8 **august** 2010), **pages** 1735–1740. ISSN: 01968904. DOI: 10.1016/j.enconman.2009.08.038.

[34] N. Nallusamy, S. Sampath **and** R. Velraj. "Experimental investigation on a combined sensible and latent heat storage system integrated with constant/varying (solar) heat sources". **in***Renewable*

Energy: 32 (7 **june** 2007), **pages** 1206–1227. ISSN: 09601481. DOI: 10.1016/j.renene.2006.04.015.

[35] C. S. Malvi, A. Gupta, M. K. Gaur, R. Crook **and** D. W. Dixon-Hardy. "Experimental investigation of heat removal factor in solar flat plate collector for various flow configurations". **in***International Journal of Green Energy*: 14 (4 **march** 2017), **pages** 442–448. ISSN: 15435083. DOI: 10.1080/15435075.2016.1268619.

[36] M. M. A. Khan, N. I. Ibrahim, I. M. Mahbubul, H. M. Ali, R. Saidur **and** F. A. Al-Sulaiman. "Evaluation of solar collector designs with integrated latent heat thermal energy storage: A review". **in***Solar Energy*: 166 (**may** 2018), **pages** 334–350. ISSN: 0038092X. DOI: 10.1016/j.solener.2018.03.014.

[37] A. E. Food, G. J. G. Despault, J. B. Tylog **and** C. E. Caves. *SOLAR STORAGE LATENT HEAT SYSTEMS USING SALT HYDRATE AND DIRECT CONTACT HEAT EXCHANGE-I PRELIMINARY DESIGN CONSIDERATIONS*. 1980.

[38] N. H. Tay, M. Belusko **and** F. Bruno. "An effectiveness-NTU technique for characterising tube-in-tank phase change thermal energy storage systems". **in***Applied Energy*: 91 (1 2012), **pages** 309–319. ISSN: 03062619. DOI: 10.1016/j.apenergy.2011.09.039.

[39] G. Wang, Z. Liao, C. Xu, G. Englmair, W. Kong, J. Fan, G. Wei **and** S. Furbo. "Design optimization of a latent heat storage using sodium acetate trihydrate". **in***Journal of Energy Storage*: 52 (**august** 2022). ISSN: 2352152X. DOI: 10.1016/j.est.2022.104798.

[40] N. A. Amin, M. Belusko, F. Bruno **and** M. Liu. "Optimising PCM thermal storage systems for maximum energy storage effectiveness". **in***Solar Energy*: 86 (9 **september** 2012), **pages** 2263–2272. ISSN: 0038092X. DOI: 10.1016/j.solener.2012.04.020.

[41] P. K. Namburu, D. K. Das, K. M. Tanguturi **and** R. S. Vajjha. "Numerical study of turbulent flow and heat transfer characteristics of nanofluids considering variable properties". **in***International Journal of Thermal Sciences*: 48 (2 **february** 2009), **pages** 290–302. ISSN: 12900729. DOI: 10.1016/j.ijthermalsci.2008.01.001.

[42] W. Banzhaf. "Self-Organizing Systems". **in***Encyclopedia of Physical Science and Technology (Third Edition)*: **byeditor**R. A. Meyers. Third Edition. New York: Academic Press, 2003, **pages** 589–598. ISBN: 978-0-12-227410-7. DOI: https://doi.org/10.1016/B0-12-227410-5/00681-5. URL: https://www.sciencedirect.com/science/article/pii/B0122274105006815.

[43] G.U.N.T. *Products*. **september** 2015. URL: https://www.gunt.de/en/products/heat-exchanger-supply-unit/060.11000/wl110/glct-1:pa-148:pr-1457.

[44] Y. Ma, Y. Tao, W. L. Wu, L. Shi, Z. Zhou, Y. Wang, J. Y. Tu **and** H. R. Li. "Experimental investigations on the performance of a rectangular thermal energy storage unit for poor solar thermal heating". **in***Energy and Buildings*: 257 (**february** 2022). ISSN: 03787788. DOI: 10.1016/j.enbuild.2021.111780.

[45] F. Klinker. "Exponential moving average versus moving exponential average". **in***Mathematische Semesterberichte*: 58 (1 **april** 2011), **pages** 97–107. ISSN: 0720728X. DOI: 10.1007/s00591-010-0080-8.

[46] U. Stritih. "An experimental study of enhanced heat transfer in rectangular PCM thermal storage". **in***International Journal of Heat and Mass Transfer*: 47 (12-13 **june** 2004), **pages** 2841–2847. ISSN: 00179310. DOI: 10.1016/j.ijheatmasstransfer.2004.02.001.

[47] M. Miansari, M. Nazari, D. Toghraie **and** O. A. Akbari. "Investigating the thermal energy storage inside a double-wall tank utilizing phase-change materials (PCMs)". **in***Journal of Thermal Analysis and Calorimetry*: 139 (3 **february** 2020), **pages** 2283–2294. ISSN: 15882926. DOI: 10.1007/s10973-019-08573-2.

[48] A. V. Olympios, P. Sapin, J. Freeman, C. Olkis **and** C. N. Markides. "Operational optimisation of an air-source heat pump system with thermal energy storage for domestic applications". **in***Energy Conversion and Management*: 273 (**december** 2022), **page** 116426. ISSN: 01968904. DOI: 10.1016/j.enconman.2022.116426.

Using letters for chapter

A

Design of the test set-up

The laboratory-size model output of Chapter 4 is the basis for the design of the experimental setup. The outputs of the system will be assessed on the constraints of the experimental setup. The constraints of the system are based on the parts of the system, which are described in Table A.1. The foremost constraint of the experimental set-up are :

- The number of tubes is restricted by the open divider (2 per open divider).
- The available mass of PCM, delivered by PLUSS, is 3 kg.
- $y_{between,tubes}$ is constrained by the dimensions of the open divider.
- Charging time of maximum 8 hours due to lab opening hours.

Other design considerations are as follows:

- The PCM and heat exchanger must be placed in a rectangular tank with transparent walls to be able to observe the melting behaviour.
- The tank must be fully airtight to prevent vapour from escaping the enclosure when the PCM is melted.
- Design has to have an excess volume compared to the PCM volume, this is due too expansion of the PCM by density change.
- The heat exchanger must be compatible with the WL110 heat exchanger service unit from Gunt. This equipment will be able to measure and control the temperatures and flow rates entering and leaving the HEX.
- A temperature probe must be inserted into the enclosure to measure the temperature of the PCM.
- The liquid fraction has to be measured and quantified. This is done by drawing a measuring grid on the transparent walls of the enclosure, as seen in Figure A.1.

Table A1: List of parts used for the experimental set-up.

Equipment	**Fitting**	**Amount**
WL100 HEX service Unit	1/4” (F)	1
Immersion heater 1 kW		2
Installation Materials		
O-ring	1 mm	25
Open Divider	1 ” (F), 1/2” (F) groups	4
Copper pipes (Brake-wire)	6 mm	5 m
Crimp-fitted couplings 6 mm	1/8” (M)	8
Nipple	1/4” (M)	4
Adapterring	1/4” (F) to 1” (M)	4
Plug	1 ”	10
Adapterring	1/4” (F) to 1/2” (M)	8
Crimp-fitted couplings 6 mm	1/4” (M)	8
Enclosure		
Acrifix Plexiglas glue		1
Loctite		1
Silicone Gel		1
Insulation		3
PMMA Plates (6mm thickness)		6
savE© HS48 by PLUSS		3 kg
Measuring device		
Trust Webcam		1
Testo 922 temperature probe		1

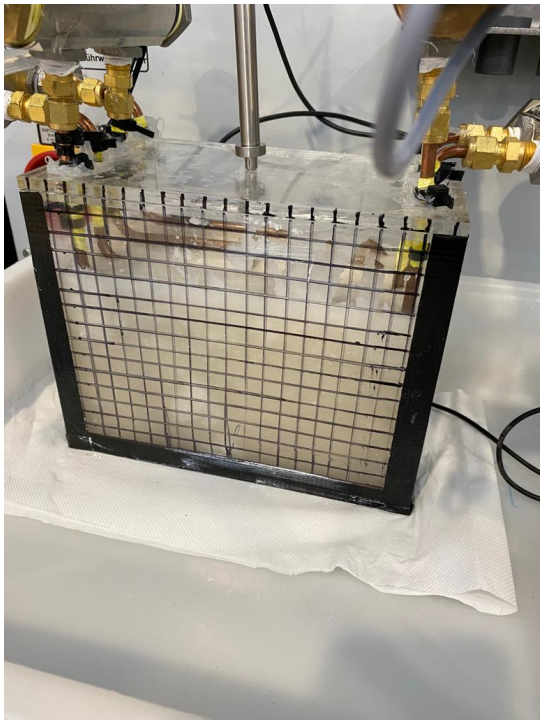

Figure A.1: Measurement grid to measure the liquid fraction.

With the constraints and considerations, the specifications are described in Table 5.1. With the specification in mind the design is known modelled in solid works as seen in Figure A.2. Note that in the final design the aluminium plates which are inserted in the model are not included.

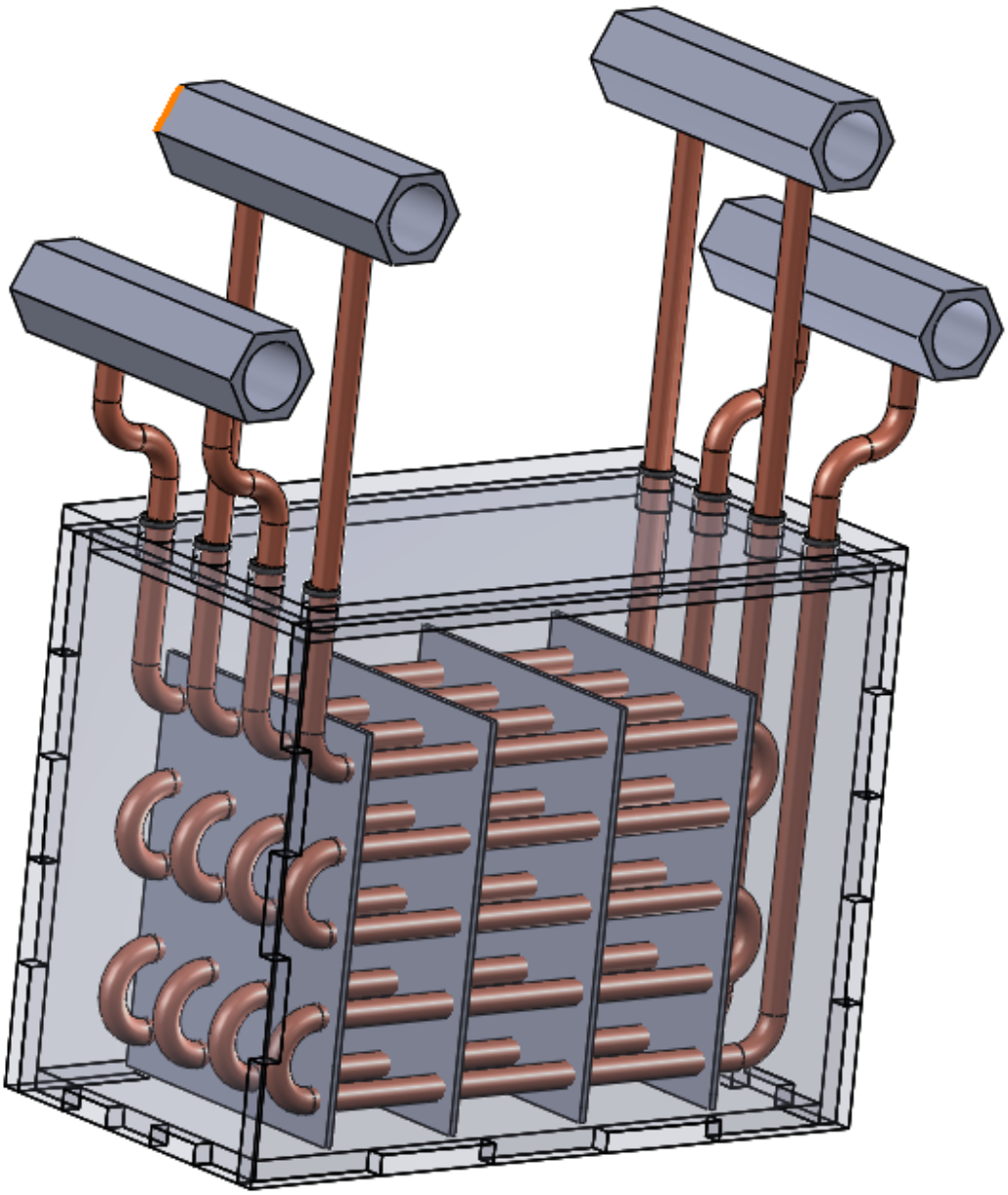

Figure A.2: Solid works assembly of final design.

B

Test procedure

The experimental validation test procedure is described in a step-by-step test plan. Tests are conducted consecutively in the order of the test plan. The loading procedure is executed before the test sequences including PCM begin. The PCM has to be melted in a separate procedure, to ensure a fully melted PCM when loading the enclosure.

1. Air Test Sequence (**30 minutes**)
   (a) Make sure enclosure is Air tight.
   (b) Prepare the Gunt WL110 heat exchanger service unit, heat the water tank up to 70 °C.
   (c) Set the flow rate of the hot side and the cold side to the right value.
   (d) The charging and discharging flow is run until the air temperature has reached a steady state.
   (e) Restore data in steady state and measure temperatures.
   (f) Determine the enclosure losses with the logged data.
   (g) Repeat this 3 times.
2. Surface temperature test sequence (**30 minutes**)
   (a) Make sure enclosure is Air tight.
   (b) Prepare the Gunt WL110 heat exchanger service unit, heat the water tank up to 70 °C.
   (c) Set the flow rate of the hot side and the cold side to the right value.
   (d) Run flow-rates until the air temperature has reached a steady state.
   (e) Restore data in steady state and measure all the temperatures.
   (f) Determine the surface temperature and the heat transfer coefficient of the walls.
   (g) Repeat 2 times.
3. Loading procedure (**6 hours**)
   (a) Heat up the packed PCM in a 75 °C water bath (see Figure B.1, until it's fully melted, this will take approximately 6 hours.
   (b) Prepare the Gunt WL110 heat exchanger service unit, heat the water tank up to 70 °C.
   (c) Notate the mass of the enclosure before pouring the molten PCM into the enclosure.
   (d) Remove the PCM from the package and pour melted PCM into the enclosure.
   (e) Note the mass of the enclosure after pouring.
   (f) Place tubes and lid onto the enclosure, and add duct tape to ensure an air tight environment.
   (g) Attach the heat exchanger to the Gunt WL110 heat exchanger service unit.
   (h) Let the PCM solidify while in the enclosure and prepare for the charging sequence.
4. Charging Sequence (**7 hours**)
   (a) Heat up the WL100 heat exchanger service unit to 70 °C.
   (b) Set the flowrate at the hot circuit to the right value, start charging the PCM.
   (c) Record the temperatures and flowrates of the heat exchanger, the PCM temperature, and the liquid fraction over time.

(d) When the PCM temperature starts to rise above 60 °C , the melting enthalpy will not be added to the system and only sensible heat will be stored.
(e) Repeat 2 times for high mass flow and 2 times for low mass flow.

5. Discharging sequence (**13 hours**)

(a) Set the flowrate at the cold circuit to the right value, start discharging the PCM.
(b) Measure all the data and record the PCM solidification.
(c) Run the system overnight and log all the data with a high sampling rate.
(d) Fully discharge the system until the PCM temperature is equal to the inlet temperature of the cold circuit.
(e) Repeat 2 times for high mass flow and 2 times for low mass flow.

6. Simultaneously charging and discharging sequence (**9 hours**)

(a) Heat up the PCM to 60 °C, when no enthalpy is added to the storing of energy, this will take approximately 4 hours
(b) Set the flow rates at the hot side and the cold side to the right values and run the test, record data for 2 hours.
(c) Heat the PCM to 60 °C again, this will take around 1 hour.
(d) Set the flow rates on the hot side and on the cold side to unequal values and run the test, recording data for 2 hours.
(e) Repeat twice for equal flow rate and twice for unequal flow rate.

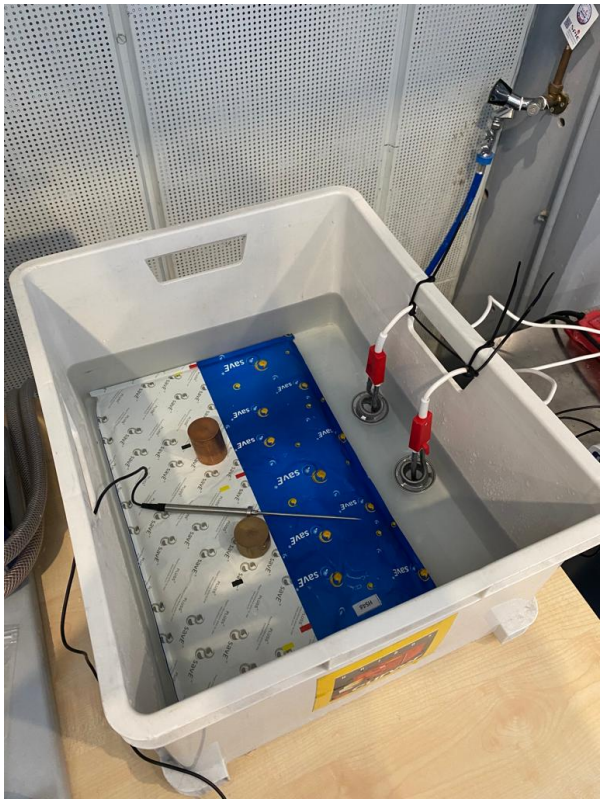

Figure B.1: Melting of PCM as described in the loading procedure

.

C

Validation of the liquid fraction

The liquid fraction is measured using the webcam and the measuring grid. By the measuring grid, only an estimation can be made on the liquid fraction. The PCM will be solid on the walls because of the cooling effect of the surrounding air. An overview of the liquid fraction over the time period of testing is given in this appendix. In addition, the predicted liquid fraction by the numerical model.

Measured liquid fraction

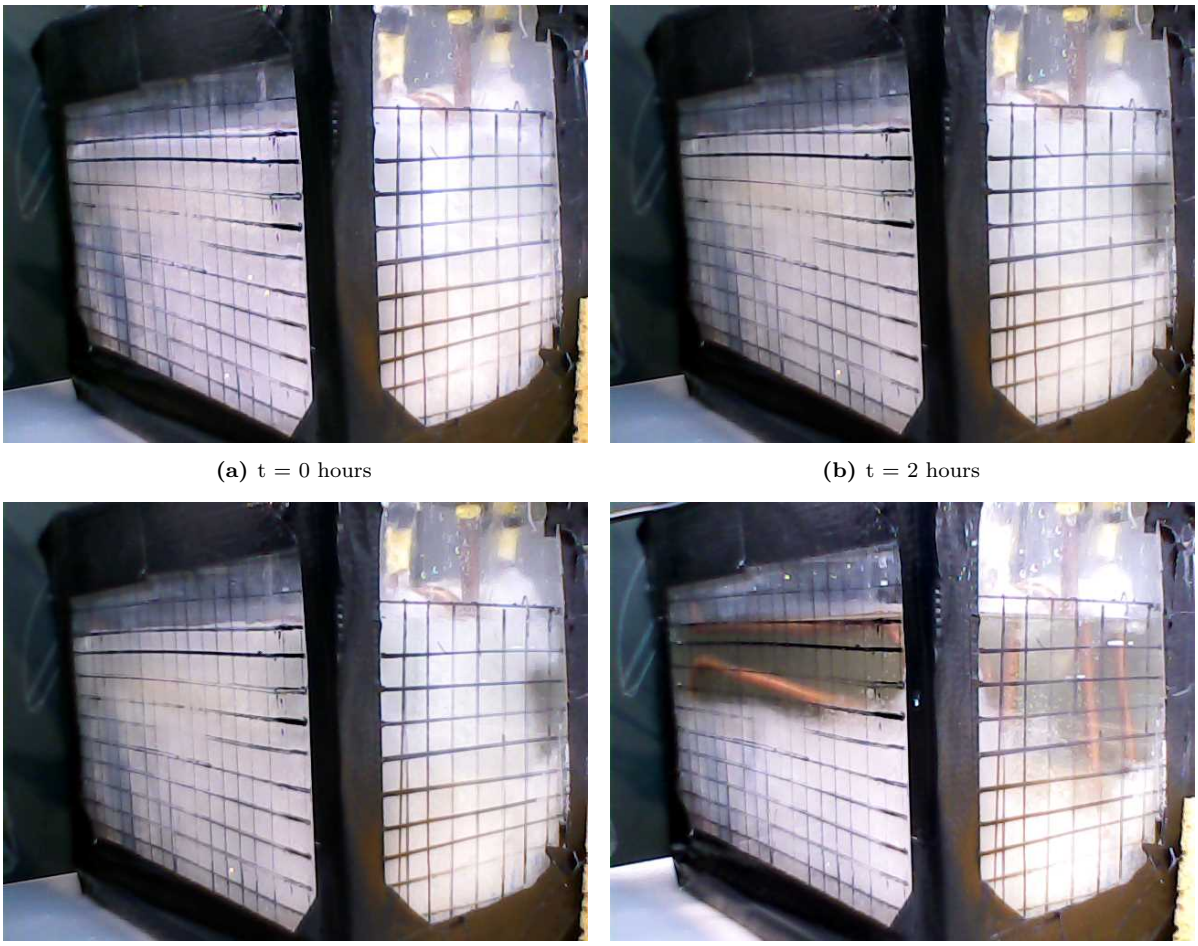

(a) t = 0 hours

(b) t = 2 hours

(c) t = 5 hours

(d) t = 7 hours

Figure C.1: Measured liquid fraction of the charging sequence

The charging does not reach a fully melted state. The maximum estimated value of the liquid fraction of the measuring grid is approximately: $\chi = 0.6$. For discharging, the solidification is visible to be complete after three hours. Initially, the PCM was not fully melted. As seen in Figure C.3a, solidification begins on the surface of the cold circuit, which is the coldest location in the material. The results are shown in Figures C.1 and Figure C.2.

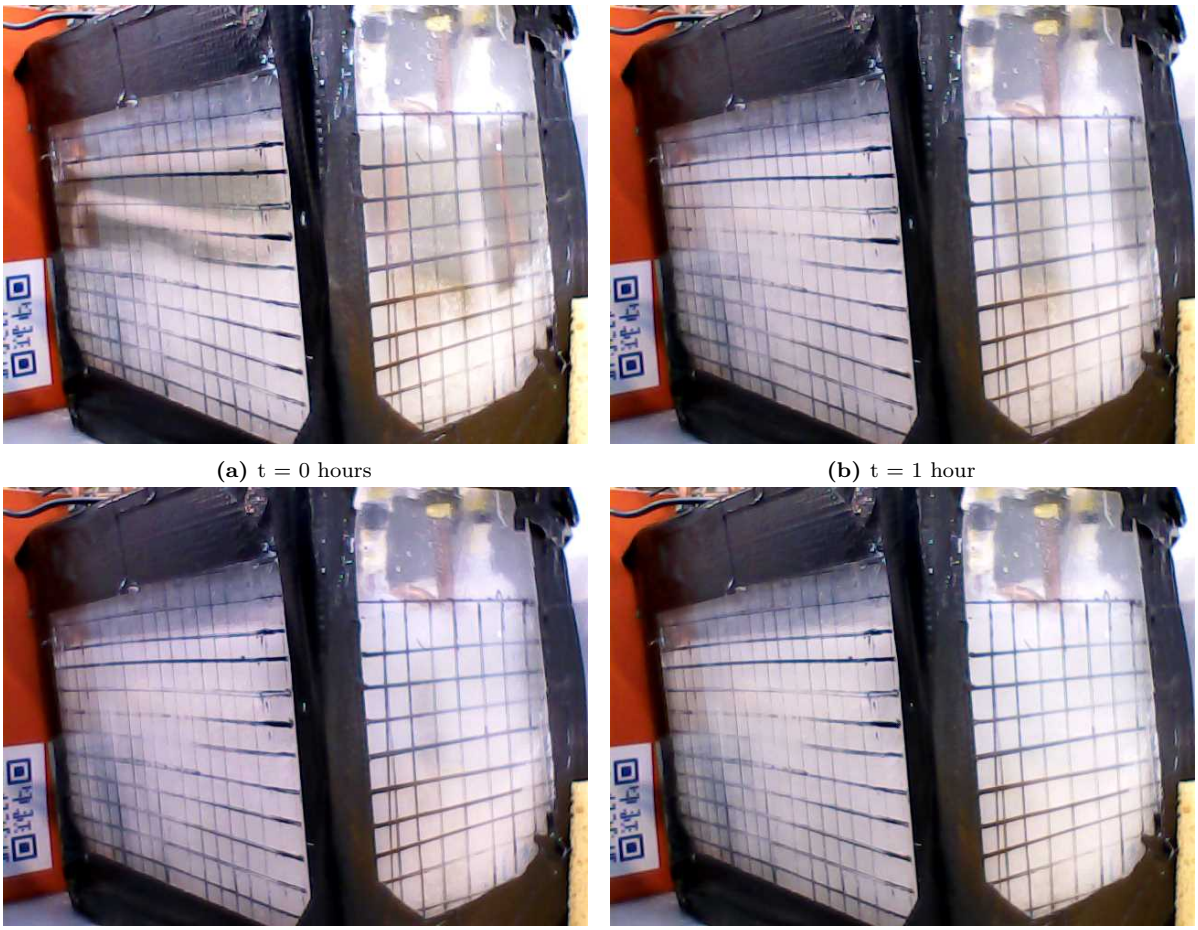

(a) t = 0 hours

(b) t = 1 hour

(c) t = 2 hours

(d) t = 3 hours

Figure C.2: Measured liquid fraction of the discharging sequence

For the simultaneous charging and discharging sequence, the results show that the liquid fraction slowly decreases. However, after 2 hours of running the test, a significant part is still melted. This is also as expected, as the liquid fraction does not decrease in this time period while charging and discharging at the same time. The results are shown in Figure C.3.

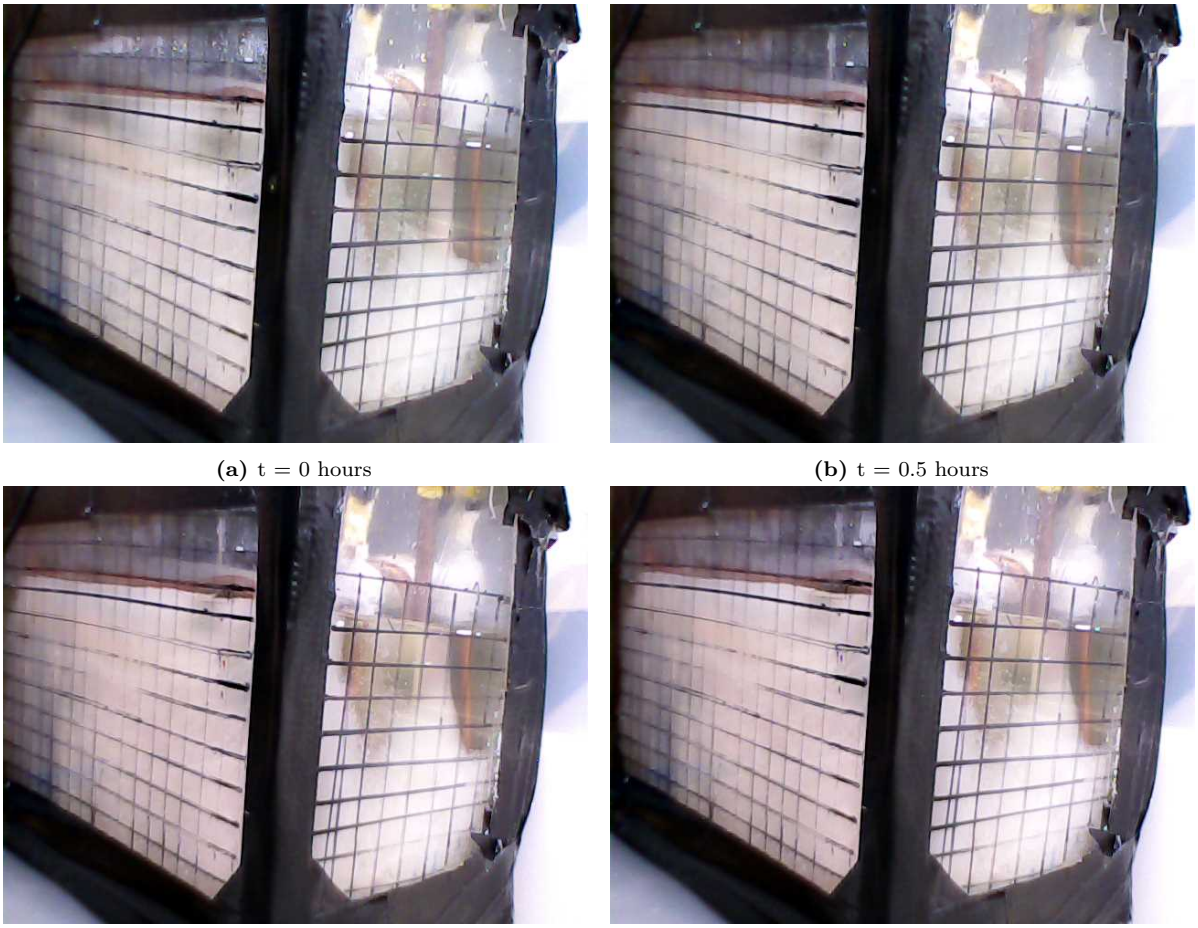

(a) t = 0 hours

(b) t = 0.5 hours

(c) t = 1 hour

(d) t = 2 hours

Figure C.3: Measured liquid fraction of the simultaneous charging and discharging sequence

Modelled liquid fraction

The modelled liquid fractions are not fully representative due to the melting distribution not being equal to 1. The temperature distribution of the PCM is only measured with one temperature probe in the middle of the material. As seen in the measurements of the liquid fraction from the previous section. When the corners and sides are not taken into account and the PCM is approached from the middle, the liquid fraction values are larger in line width than the outputs of the model. The liquid fraction modelled for all heat transfer modes is shown in Figure C.4.

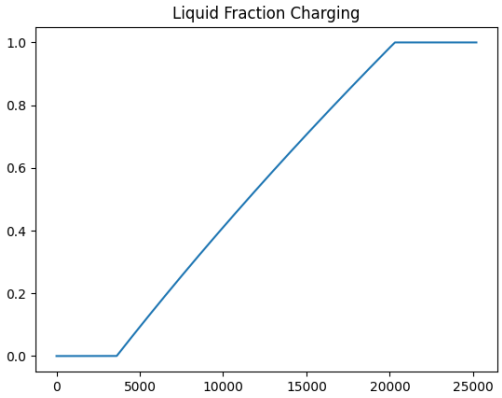

(e) Liquid fraction for charging.

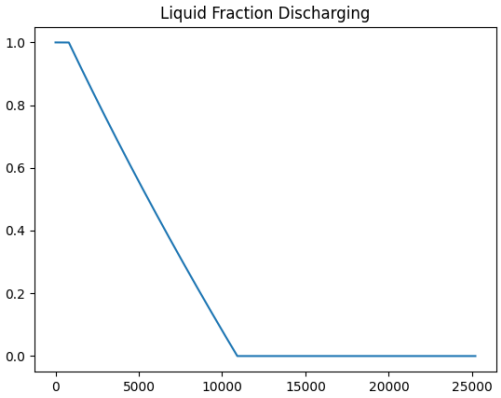

(f) Liquid fraction for discharging.

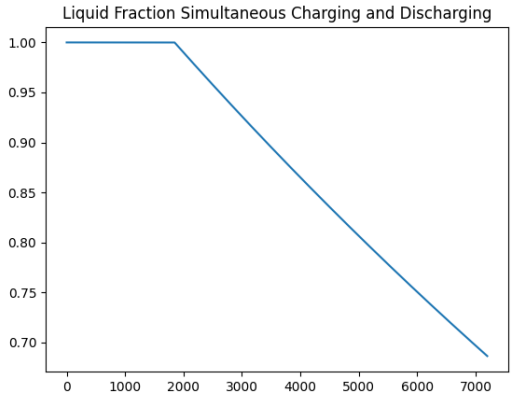

(g) Liquid fraction for charging and discharging.

Figure C.4: Liquid fraction of validated model for all test sequences.

D

Results of the liquid fraction

In this appendix, the liquid fractions of the three configurations of the optimisation are given, as well as the liquid fraction of both sizes of the numerical analysis, The results will be given for all three modes of heat transfer.

Optimization

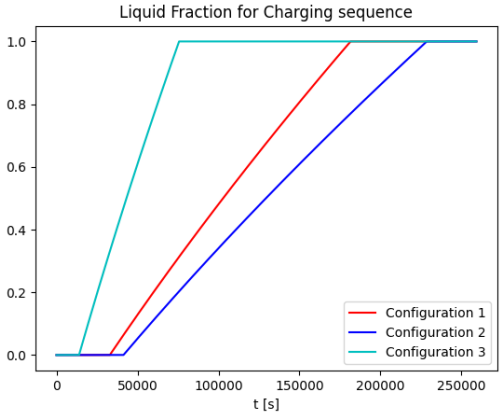

(a) Liquid fraction for charging.

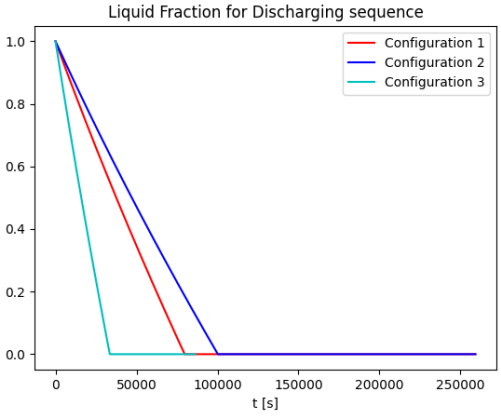

(b) Liquid fraction for discharging.

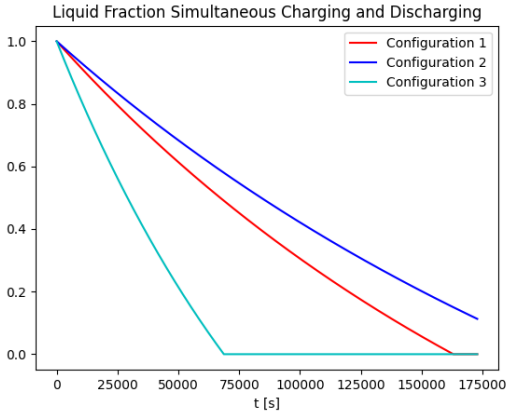

(c) Liquid fraction for charging and discharging.

Figure D.1: Liquid fraction of all three configurations of optimization, for all modes of heat transfer.

Numerical Analysis

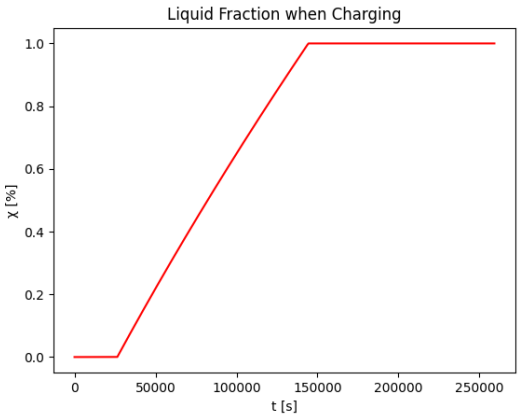

(a) Liquid fraction of the commercially available heat battery while charging.

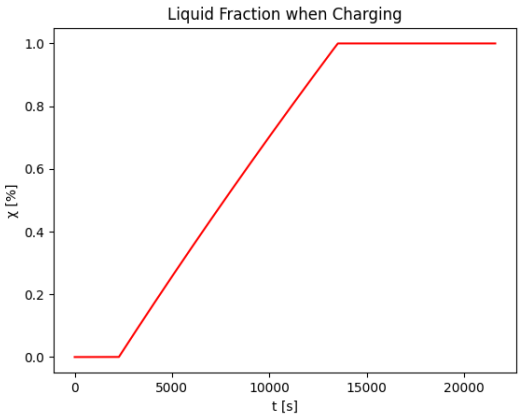

(b) Liquid fraction of the laboratory-size scale while charging.

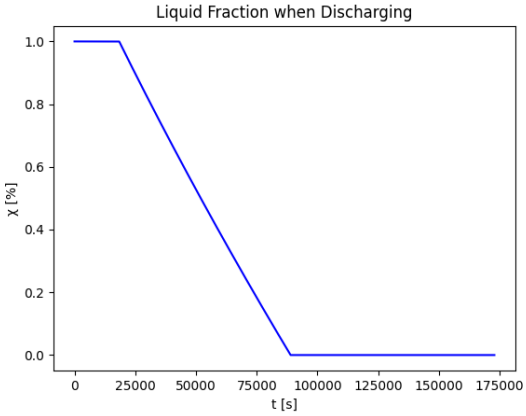

(c) Liquid fraction of the commercially available heat battery while discharging.

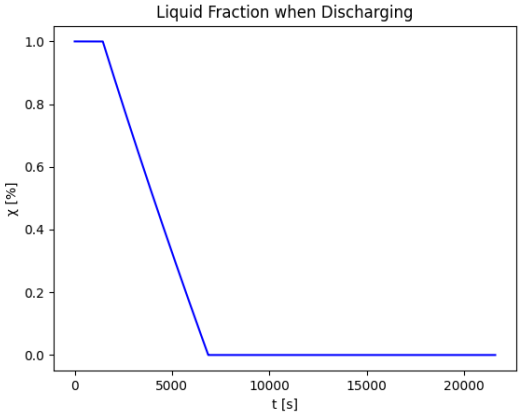

(d) Liquid fraction of the commercially available heat battery while discharging.

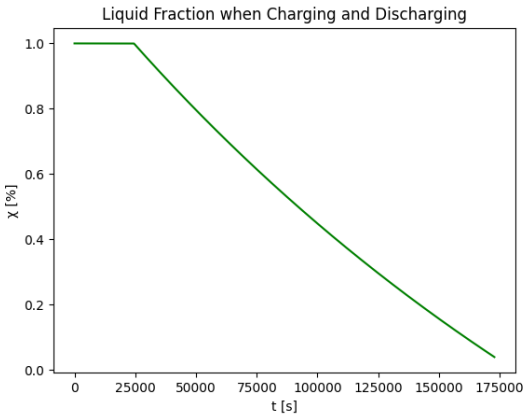

(e) Liquid fraction of the commercially available heat battery while charging and discharging.

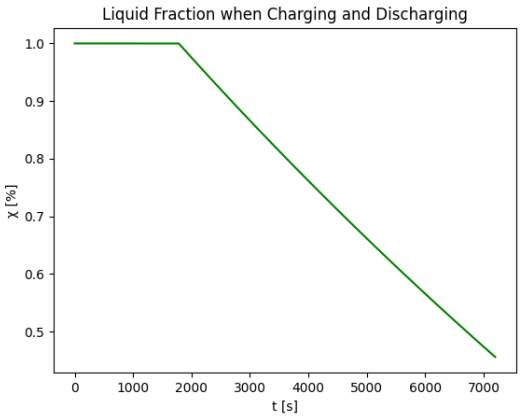

(f) Liquid fraction of the commercially available heat battery while charging and discharging.

Figure D.2: Liquid fraction over time for for both size of the numerical model, for all modes of heat transfer